

# Structure and dynamics of the solar chromosphere

*Front cover:* Front page was designed by Thijs Krijger, with credit to:  
T.A. Rector, I.P. Dell'Antonio, NOAO, AURA, NSF &  
SOHO - EIT Consortium, ESA, NASA.

Copyright 2002 J.M. Krijger

Alle rechten voorbehouden. Niets van deze uitgave mag worden verveelvoudigd, opgeslagen in een geautomatiseerd gegevensbestand, of openbaar gemaakt, in enige vorm, zonder schriftelijke toestemming van de auteur.

ISBN 90-393-3156-1





# Structure and dynamics of the solar chromosphere

Structuur and dynamica van de zonnchromosfeer

(met een samenvatting in het Nederlands)

PROEFSCHRIFT

TER VERKRIJGING VAN DE GRAAD VAN DOCTOR AAN  
DE UNIVERSITEIT UTRECHT OP GEZAG VAN  
DE RECTOR MAGNIFICUS, PROF. DR. W.H. GISPEN,  
INGEVOLGE HET BESLUIT VAN HET COLLEGE VOOR  
PROMOTIES IN HET OPENBAAR TE VERDEDIGEN OP  
WOENSDAG 9 OKTOBER 2002 DES MIDDAGS TE 12.45 UUR

DOOR

**Johannes Mattheus Krijger**

geboren op 29 april 1976, te Dordrecht

**Promotor:**

Katholieke Universiteit Nijmegen

**Prof. dr. J. Kuijpers**

Afdeling Sterrenkunde,

**Co-promotor:**

Universiteit Utrecht

**dr. R. J. Rutten**

Sterrenkundig Instituut,

Dit proefschrift werd mede mogelijk gemaakt door financiële steun van de Nederlandse Organisatie voor Wetenschappelijk Onderzoek (NWO).

Aan mijn beide ouders,  
zonder wiens steun  
ik nooit zo ver gekomen was:

Nelleke Wilhelmina Krijger-Blom  
&  
Marinus Mattheus Krijger



# Contents

<b>1</b>	<b>Introduction</b>	<b>7</b>
	authors: J.M. Krijger ;	
1.1	The Solar Chromosphere . . . . .	8
1.2	Solar granulation . . . . .	8
1.3	Helioseismology . . . . .	11
1.4	The magnetic sun . . . . .	12
1.4.1	Space Weather . . . . .	13
1.5	Chromospheric structure . . . . .	15
1.5.1	Chromospheric oscillations . . . . .	16
1.5.2	Chromospheric Heating . . . . .	17
1.5.3	The complete picture . . . . .	18
1.5.4	Why study the solar chromosphere? . . . . .	19
1.6	This thesis . . . . .	20
<b>2</b>	<b>Photospheric flows measured with TRACE</b>	<b>23</b>
	authors: J.M. Krijger, T. Roudier, M. Rieutord ; published in A&A, 2002, 389, 672-677	
2.1	Introduction . . . . .	24
2.2	Observations and reduction . . . . .	25
2.2.1	TRACE sequence . . . . .	25
2.2.2	Local Correlation Tracking . . . . .	26
2.2.3	Isotropic divergence . . . . .	29
2.3	Results . . . . .	30
2.3.1	Divergence . . . . .	30
2.3.2	Chromospheric network . . . . .	30
2.3.3	Spatial comparison . . . . .	30
2.4	Conclusions . . . . .	32

---

<b>3</b>	<b>Photospheric flows measured with TRACE</b>	
	<b>II. Network formation</b>	<b>35</b>
	authors: J.M. Krijger, T. Roudier ; Submitted to A&A	
3.1	Introduction . . . . .	36
3.2	Observations . . . . .	37
3.3	Local Correlation Tracking . . . . .	38
3.4	Cork Insertion . . . . .	39
3.5	Results . . . . .	42
3.5.1	Increased emergence rate . . . . .	47
3.6	Discussion . . . . .	47
3.7	Conclusion . . . . .	48
<b>4</b>	<b>Dynamics of the solar chromosphere</b>	
	<b>III. Ultraviolet brightness oscillations from TRACE</b>	<b>51</b>
	authors: J.M. Krijger, R.J. Rutten, B.W. Lites, Th. Straus, R.A. Shine, T.D. Tarbell ; published in A&A, 2001, 379, 1052-1082	
4.1	Introduction . . . . .	52
4.2	Observations and reduction . . . . .	55
4.3	Fourier analysis . . . . .	60
4.4	Results . . . . .	64
4.4.1	Spatio-temporal behaviour . . . . .	64
4.4.2	Spatial modulation variations . . . . .	73
4.4.3	One-dimensional modulation spectra . . . . .	81
4.4.4	Two-dimensional modulation spectra . . . . .	90
4.5	Error analysis . . . . .	95
4.6	Discussion . . . . .	99
4.7	Conclusions . . . . .	103
<b>5</b>	<b>Dynamics of the solar chromosphere</b>	
	<b>IV. Evidence for atmospheric gravity waves from TRACE</b>	<b>105</b>
	authors: R.J. Rutten, J.M. Krijger; Submitted to A&A	
5.1	Introduction . . . . .	106
5.2	Observations and reduction . . . . .	107
5.3	Analysis and results . . . . .	109
5.3.1	Space-time representations . . . . .	109
5.3.2	Time-delay scatter representations . . . . .	112
5.3.3	Fourier representations . . . . .	118
5.4	Discussion . . . . .	122
5.4.1	Terminology . . . . .	122
5.4.2	Gravity wave excitation . . . . .	123
5.4.3	Inverse canopy mapping . . . . .	123

---

---

5.4.4	Magnetic alternative . . . . .	125
<b>6</b>	<b>Dynamic behaviour of the upper solar atmosphere:</b>	
	<b>II. SUMER/SOHO, TRACE and VTT observations</b>	<b>127</b>
	authors: J.M. Krijger, P. Heinzel, W. Curdt, W. Schmidt ; Submitted to A&A	
6.1	Introduction . . . . .	128
6.2	Observations and reduction . . . . .	129
6.2.1	SUMER/SOHO observations . . . . .	129
6.2.2	TRACE observations . . . . .	131
6.2.3	VTT observation . . . . .	131
6.2.4	Coalignment . . . . .	132
6.3	TRACE 1600 Å versus Ca II K . . . . .	134
6.4	TRACE Ly $\alpha$ versus SUMER Ly $\alpha$ . . . . .	135
6.5	Oscillations in higher Lyman lines and in the Lyman continuum . . . . .	137
6.6	Discussion and Conclusions . . . . .	141
<b>7</b>	<b>Structuur en dynamica van de zonnechromosfeer</b>	<b>143</b>
	<b>Bibliography</b>	<b>148</b>
	<b>Dankwoord</b>	<b>163</b>
	<b>Levensloop</b>	<b>165</b>

---

You are my sun,  
my moon,  
my starlit sky.  
Without you,  
I dwell in darkness.

Madmartigan, *Willow*

Join me,  
and together  
we shall rule the galaxy.

Darth Vader, *The Empire strikes back*

---

# Chapter 1

## Introduction

**Abstract.** The chromosphere is the interface between the solar body which is dominated by gas pressure and fluid motions and the solar corona which is dominated by magnetic fields. Study of this layer including the so-called quiet-sun chromosphere is crucial for our understanding of the entire sun. In this introduction the main properties of the solar surface layers are briefly described with a focus on the unsolved problems. At the end is summarized how the various chapters in this thesis contribute to the solution of these problems.

## 1.1 The Solar Chromosphere

The structure of the chromosphere is dominated by magnetic fields, while the chromospheric dynamics are dictated by oscillations and flows. It is the interaction between flows and fields in a complicated geometry that makes the chromosphere into one of the most challenging layers of the solar atmosphere.

The standard temperature stratification of the solar atmosphere is shown in Fig. 1.1 with the formation heights of different spectral lines. Vernazza et al. (1981) have derived this model semi-empirically by inverting observed extreme ultraviolet (EUV), Ly $\alpha$  and other line intensities. The solar chromosphere lies in between the “cool” ( $T \approx 5000$  K,  $h \approx 0 - 500$  km) photosphere (the temperature drop on the right hand side of Fig. 1.1) and the warmer ( $T \approx 25 \times 10^3$  K,  $h \approx 2100$  km) transition region (TR) which merges into the hot ( $T \approx 2 \times 10^6$  K,  $h \geq 2300$  km) corona (sharp temperature rise on left-hand side of Fig. 1.1).

The Ca II spectral line is frequently used to study the lower chromosphere. However the intrinsic problem with Ca II observations is that Ca II photons scatter significantly before escaping from the solar atmosphere, creating a fuzzy picture of the actual chromospheric structure. Another possible spectral line in which the chromosphere can be observed is H $\alpha$ , but solar images taken in H $\alpha$  show such a complex structure that they are very hard to understand, as the H $\alpha$  spectral line is very sensitive to various kinds of ionisation (Rutten 1998). The earth’s atmosphere blocks the alternative possibility of using ultraviolet (UV) observations (e.g. Ly $\alpha$  or Mg II) so if one wants to study the chromosphere in the UV one needs to observe from space.

## 1.2 Solar granulation

The outer 30% (in radius) of the sun is convective. Energy is transported upwards by convective hot upwellings until the optical depth becomes low enough for photons to escape into outer space. We see these upwellings as a pancake pattern. The pancakes are called granules. At the top, sudden radiative losses cool the convective upwellings, which are halted and sink down again in the lanes between granules, the intergranular lanes. The solar granulation has a characteristic horizontal scale of 1000 km, and a life-time of about 10 min (e.g., Bray et al. 1984). Figure 1.2 presents an example of photospheric granulation as taken by the Dutch Open Telescope at La Palma. Granulation is remarkably well reproduced in numerical simulations by e.g., Stein & Nordlund (1998) on the basis of radiative cooling in the surface thermal boundary layer. They have shown that granules evolve by pushing out against and being pushed in by their neighbouring granules, and by being split by overlying plasma that cools and is pulled down by gravity.

Besides the normal granulation, there is a controversial larger mesogranulation

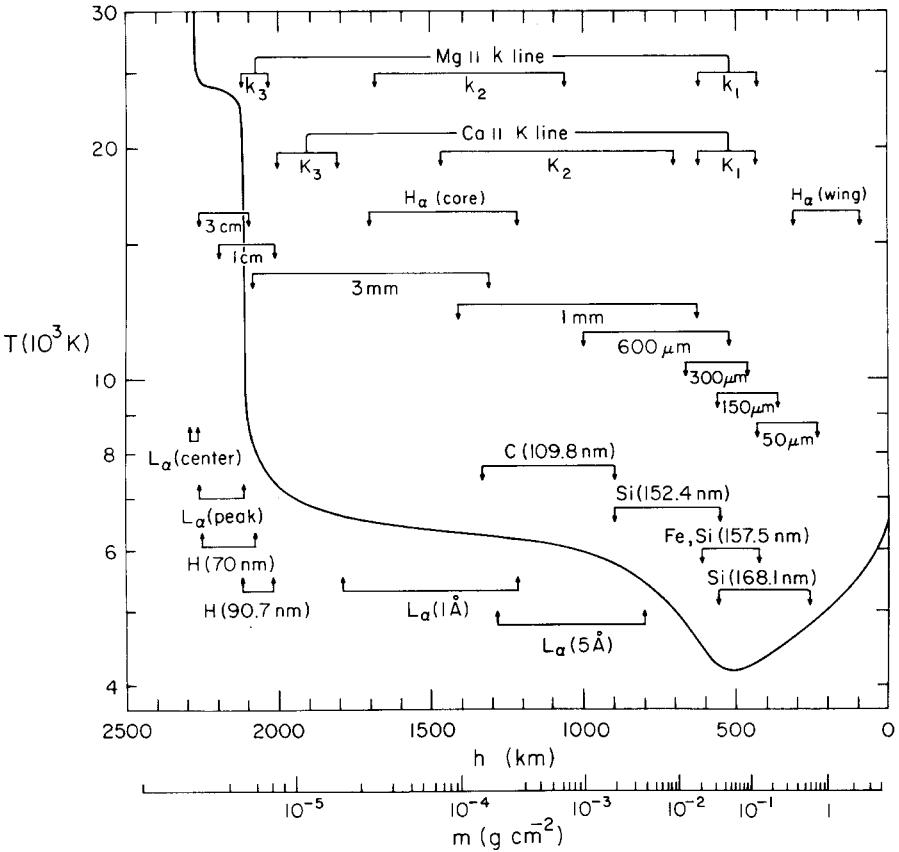


Figure 1.1: The standard quiet sun atmosphere temperature stratification, derived from inversion of the EUV continuum, Ly $\alpha$  line and other observations. Shown is temperature against height and density (assuming radiative equilibrium). Indicated are the approximate formation heights for various lines and continua used for the temperature determination (numbers are wavelengths). From Vernazza et al. (1981).

with sizes in the order of 7 Mm and a maximum lifetime of 4 to 6 hrs (Shine et al. 2000a). Ever since its first discovery by November et al. (1981), its existence has been doubted. The different reported scales, lifetimes, velocities, *etc.* depend very much on the different filters applied to the data. This dependency has convinced some authors that mesogranulation is purely an artefact of the data reduction (Roudier et al. 1999). Mesogranules are most often identified in “divergence” maps of the velocity field at the surface. Figure 1.3 shows such a divergence map of the solar surface averaged over a period of 6 hrs. Divergence maps are derived from (horizontal) velocity fields showing locations where matter is welling up (bright)

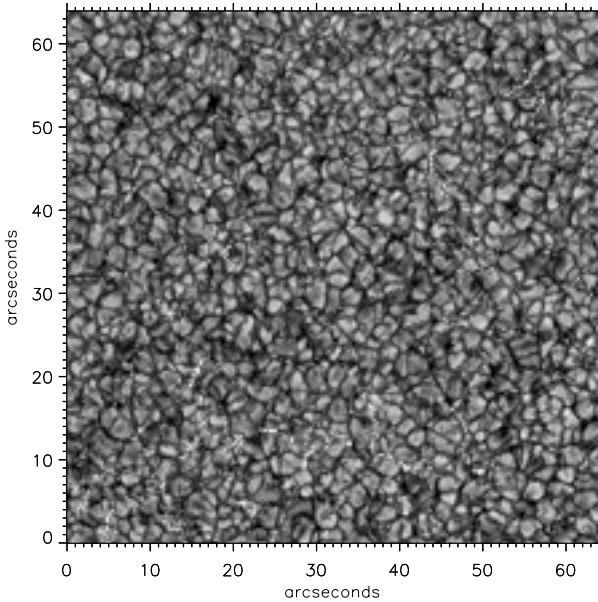


Figure 1.2: A fine granulation image taken by the Dutch Open Telescope on October 19, 2001 09:34 UT in the so-called G-band centred on the CH absorption band between 4300 and 4310 Å. The bright upflows or granules combine with the dark downflows or intergranular lanes into a pancake pattern. Inside the intergranular lanes are the very bright G-band bright points or filigree grains, which are interpreted as magnetic fluxtubes poking through the solar photosphere. These fluxtubes are swept away quickly by the granulation into the intergranular lanes and subsequently to the boundaries of supergranules. (1 arcsec on our sky equals about 730 km on the solar surface). Image provided by P. Sütterlin.

and sinking down (dark), and clearly show convective patterns. Some examples of mesogranular structures are indicated by the black arrows in Fig. 1.3. For a discussion of previous studies of mesogranulation, see Rieutord et al. (2000).

The existence of an even larger scale of granulation, called supergranulation, has been discovered by Leighton et al. (1962) with a length scale between 13 Mm and 35 Mm (e.g., Hagenaar et al. 1997) and a lifetime between 15 hours and 52 hours, depending on the scale (e.g., Wang & Zirin 1989; Simon et al. 1995). In Fig. 1.3 the supergranular pattern is indicated by white dotted contours. Supergranules are found in white light by tracking and averaging the horizontal motion of individual granules. Line-of-sight dopplergrams show supergranules only away from disk centre. Local helioseismology using time-distance inversion (Duvall et al. 1993; Hathaway et al. 2002) is a new promising technique that also allows study of supergranules.

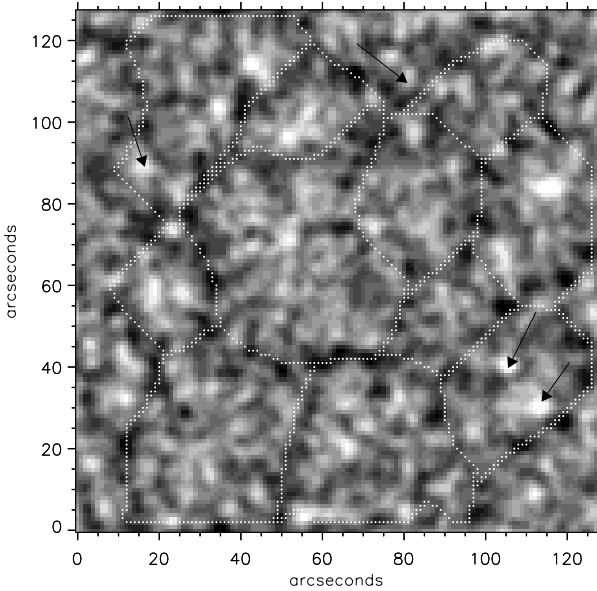


Figure 1.3: Horizontal divergence map showing areas where matter rises up (bright) and sinks down (dark). The supergranular pattern is indicated by dotted contours. A few mesogranular features have been marked with black arrows.

## 1.3 Helioseismology

The sun is oscillating on a multitude of spatial scales and frequencies. The (standing and running) waves have radial velocity components and are observed as Doppler shifts of spectral lines and continuum brightenings.

The most common kind of solar waves are standing pressure (or acoustic), gravity and surface gravity waves, generating the so-called p-modes, g-modes and f-modes respectively.

At the surface acoustic waves are the most prominent and are generated on a local scale but can become global by getting trapped in the solar atmosphere that acts as a resonant cavity. The large density drop near the solar surface acts as an upper boundary, similarly the internal increase in sound speed as a result from the increasing temperature) acts as lower boundary by refracting downward propagating waves back. The discovery of these propagating sound waves by (Leighton et al. 1962) and their explanation by Ulrich (1970) and Leibacher & Stein (1971) opened a new field in solar physics: helioseismology. As the sun is spherical these modes can be described using spherical harmonics and are characterized by their degree and azimuthal-order quantum numbers,  $l$  and  $m$ . The signature of the standing waves is

best seen in helioseismological displays as Fig. 1.4 showing oscillation power as a function of temporal and spatial frequency. Destructive interference filters out all but the resonant frequencies which show up at a specific combination of temporal and spatial frequency.

While the upper boundary of all cavities is near the solar surface, the depth of the lower boundary is dependent on the oscillation frequency and the spherical harmonic degree  $l$ . As a result some cavities do not extend very deeply while other reach rather close to the centre of the sun. Each mode then samples different but overlapping regions of the solar interior. The large number of different resonant modes, each with a different cavity depth, allow astronomers to study different structural properties, like motions, temperature, and chemical composition, from just beneath the solar surface to almost the solar core (e.g., Leibacher et al. 1985; Christensen-Dalsgaard 1988).

Helioseismology has been using the p-modes since their frequencies can be measured to such high accuracy. An even better probe of the solar core would be the g-modes, that are truly confined within the solar interior. However, no firm detection for g-modes have yet been claimed as their amplitude are very small compared to the solar noise (e.g., Appourchaux et al. 2000).

## 1.4 The magnetic sun

Observationally, one distinguishes two different kinds of regions on the solar surface; “quiet sun” and “active sun”, referring to regions with little or no large scale magnetic structure and, respectively, regions where the magnetic field dominates the structure. Typical examples of active regions are sunspots, large bundles of magnetic fluxtubes that are strong enough to prevent normal granulation. This causes the plasma within a sunspot to be cooler than its surroundings, which is why a sunspot appears a relative dark spot. The inflow of warmer plasma from around the sunspot keeps the sunspot stable as the magnetic elements want to disperse (e.g., Zhao et al. 2001).

The magnetic field configuration above active regions reaches up into the solar corona and can be very complicated. When the coronal configuration becomes too tangled reconnection between different magnetic field lines takes place and the free magnetic energy is released into an enormous and bright explosion called a solar flare with a timescale up to 15 min and energy release up to  $10^{32}$  ergs (Carrington 1859; Somov 1992, e.g.). These flares can deposit large amounts of energy into their surroundings. Other examples of reconnection are Coronal Mass Ejections (CME), large magnetized plasmoids which are expelled from the sun at large speed (e.g., Hildner et al. 1975; Forbes 2000) or microflares (e.g., Porter et al. 1987) which have been suggested to be a possible method to heat the corona (e.g., Moore et al. 1999). Magnetograms (such as in Fig. 1.5) are being used to predict the eruption of CMEs.

---

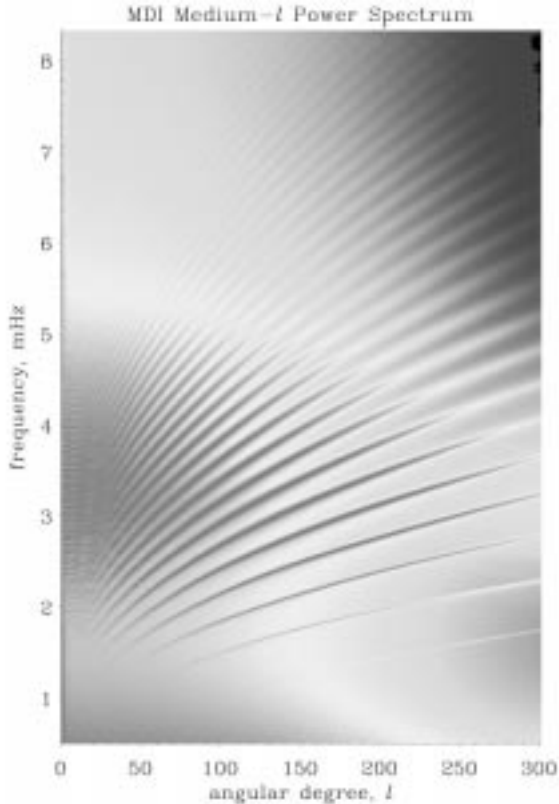


Figure 1.4: Medium- $l$   $\nu$  diagram showing power as a function of spatial and temporal frequency. From Rhodes et al. (1998).

The quiet-sun is the collection of small-scale magnetic fluxtubes and intermittent non-magnetically fluid cells. On average it is much calmer, is not strongly magnetically dominated, and it conforms to the more regular structure as described in Fig. 1.6 and Fig. 1.9. The huge differences in emission between active and quiet sun forced observers and theoreticians to differentiate between the two. In this thesis the focus is on the quiet sun.

### 1.4.1 Space Weather

The influence of all magnetic disturbances caused by the sun on the earth is called space weather. Most magnetic disturbances are either caused by CMEs or strong increases in UV radiation that change the ionosphere altitude. As these magnetic

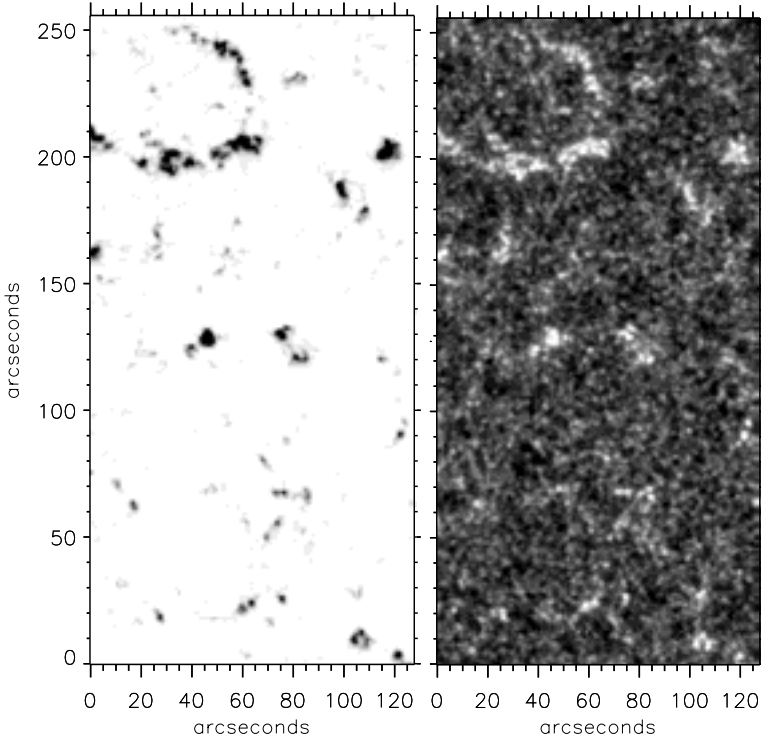


Figure 1.5: Left: MDI magnetogram showing absolute magnetic field strength. Right: Logarithmic greyscale TRACE 1700 Å image, showing chromospheric emission. Both panels show the same sub-field and were obtained around 12 May 1998, 15:30 UT.

disturbances hit the earth they can induce electric currents in conductors on earth and produce energetic particles (e.g., Daglis 2001). These effects can severely harm satellites, astronauts and large powergrids among others. Understanding and modelling the interaction between CMEs and the earth's magnetosphere is thus of utmost importance to our modern society (Keppens & Goedbloed 2000; Poedts 2001).

The solar cycle of  $2 \times 11$  years influences also the earth's climate. The global mean temperature correlates with the number of sunspots over the last century (Soon et al. 1996), the solar irradiance variations in the EUV (Solanki & Fligge 2000), and anticorrelates with the cosmic ray modulation at earth by the solar wind magnetic field (e.g., Lockwood 2002). At this moment it is unclear what is causing the earth climate variations: the UV radiation (e.g., Soon et al. 1996) or the change in earth low cloud cover due to cosmic rays (e.g., Marsh & Svensmark 2000).

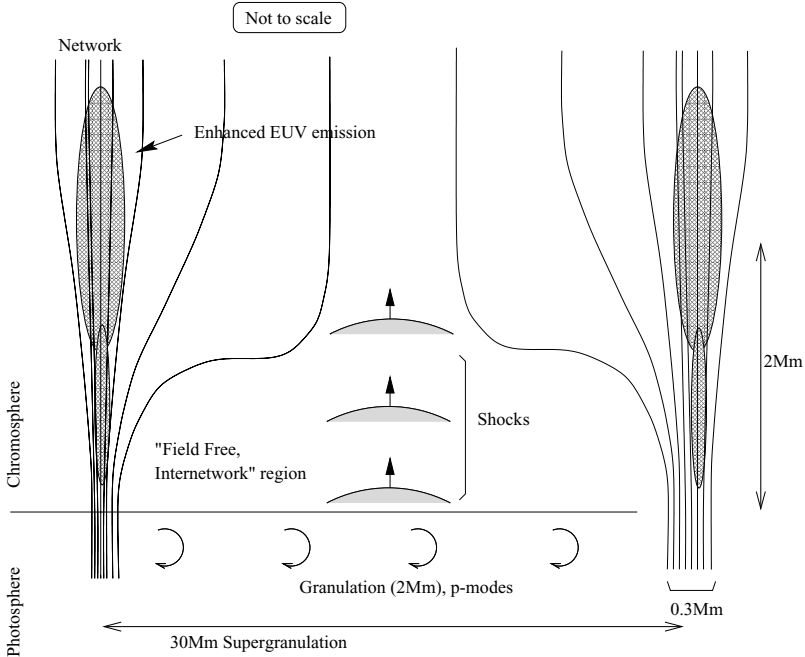


Figure 1.6: Cartoon with current ideas about the structure of the lower solar atmosphere, showing a vertical slice of a single supergranule and the overlying chromosphere with clusters of magnetic field tubes at its boundaries. From Judge & Peter (1998)

## 1.5 Chromospheric structure

The current idea about the structure of the chromosphere is displayed in Fig. 1.6, showing a schematic vertical slice of the lower solar atmosphere across a single supergranulation cell. At the bottom is the photosphere with granules and p-modes. The supergranular motion buffets against the magnetic elements (fluxtubes) that poke through the solar atmosphere. Any magnetic elements rising up from deeper layers through the photosphere inside the supergranules are quickly swept to the cell boundaries and form clusters that remain at the supergranular boundaries until they are destroyed by reconnection (e.g., Hagenaar et al. 1997). This so-called “magnetic network” is observed in photospheric magnetograms (like Fig. 1.5) and has a magnetic field strength around a kilogauss. In the chromosphere the gas pressure drops more quickly with increasing height than the magnetic pressure of these magnetic elements. As the magnetic forces win over the gas force the magnetic elements expand and fill the entire higher chromosphere, forming a “magnetic canopy” as has



Figure 1.7: Magnetic fluxtubes sticking through the solar photosphere expand in the chromosphere due to the relative increase of magnetic over gas pressure forces until it fills the entire upper chromosphere and forms the “magnetic canopy”. From Schrijver & Zwaan (2000)

been suggested by Kopp & Kuperus (1968) and later by Jones & Giovanelli (1982) (see Fig. 1.7).

Magnetic heating of the chromosphere is concentrated in the magnetic clusters (dark shading in Fig. 1.6) and causes bright patches in chromospheric emission, which are arranged in a cellular pattern. These patches form the “chromospheric network” which coincides with the magnetic network. When averaging observations over long periods, the chromospheric network maps the supergranular cell boundaries, be it incompletely (see Fig. 1.8). Because of this mapping of the supergranules the term “cell boundaries” is sometimes also used for these patterns, but since these patches do not map the boundaries completely, even when averaged over very long periods, the term is somewhat inappropriate. Inside these supergranular patterns is the “internetwork”: dark in chromospheric emission and largely free of (kilogauss) magnetic field, sometimes also called intranetwork or cell interior. These terms are again misplaced because the chromospheric network does not fully map the supergranular cell boundaries. At irregular intervals, magnetic flux concentrations emerge in the internetwork in the form of ephemeral regions, small bipoles ( $< 20$  arcsec) consisting of two regions of opposite polarity that are buffeted around by granulation (e.g., Harvey-Angle 1993; Schrijver et al. 1997).

### 1.5.1 Chromospheric oscillations

The solar chromosphere shows a variety of oscillations that are strongly affected by the presence of magnetic field, which causes a difference in the dynamics of the network and internetwork (e.g., Lites et al. 1999). In the internetwork, the wide-band acoustic wave spectrum is dominating around the three-minute oscillation. The network shows modulations at a period of only 5 min or longer. These may be the effect of erratically buffeting of the magnetic field by the granulation at the location where it pokes through the photosphere (erratic footpoints motions) (Kneer & von Uexküll 1983, 1985, 1986, 1993; Lites et al. 1993).

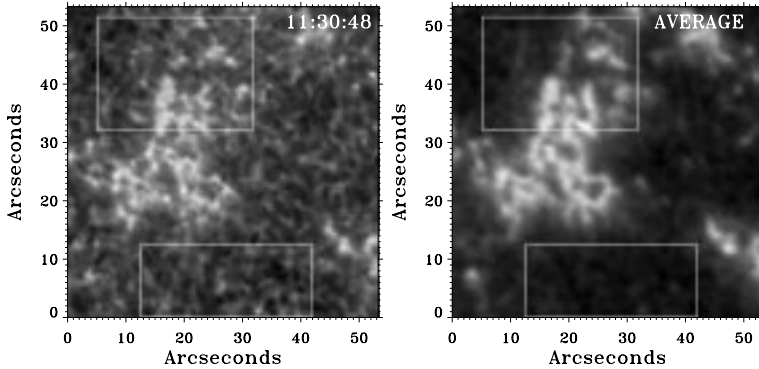


Figure 1.8: Left: an example Ca II K image taken with the Swedish Vacuum Solar Telescope at La Palma (Löfdahl et al. 1998) Right: Temporal average over 70 min of the same area. The internetwork brightness pattern (lower box) loses contrast much faster than the network due to the internetwork rapid variability. The averaged network incompletely maps the supergranular cell boundaries. From Lites et al. (1999).

Well observed chromospheric oscillation phenomenon are the chromospheric internetwork grains, bright features that intermittently appear in the internetwork. Originally these were called Ca II  $K_{2v}$  grains as they show their largest brightness just blueward of the Ca II H & K spectral lines. But since they can also be clearly seen on wider-band Ca II or TRACE UV observations the name chromospheric internetwork grains is more correct. These grains have been reproduced in detailed hydrodynamic computations (Carlsson & Stein 1994) and are identified as weak acoustic upward propagating shocks driven by photospheric piston-like motions.

## 1.5.2 Chromospheric Heating

Figure 1.1 shows a chromospheric temperature rise above  $h = 500$  km. This temperature rise is needed in the empirical model of Vernazza et al. (1981) to explain the bright chromospheric emission and has been accepted for many years without doubt. The physical process that causes the implied heating is however still unknown. Biermann (1946, 1948) and Schwarzschild (1948) proposed that acoustic waves are generated in the photosphere and dissipate as shocks in the chromosphere. Magneto hydrodynamic calculations predict short-period (around 30 sec) acoustic waves to be the culprit (Ulmschneider 1970, 1974) but until this day no observational evidence of these waves has been found, which has led to a search for alternative heating mechanisms (Kalkofen 1991; Narain & Ulmschneider 1996).

A (controversial) by-product of the calculations of Carlsson & Stein (1994) on chromospheric grains was that the apparent chromospheric temperature rise is a possible artifact of the inversion technique used by Vernazza et al. (1981). Carlsson &

Stein (1995) propose that acoustic shocks travel upward in the non-magnetic part of the chromosphere where they heat the chromosphere for only short intervals, without really increasing the average temperature of the chromosphere itself. However, these short hot intervals dominate the observed temporal average of the temperature as the Planck function has an exponential temperature dependence at the UV wavelengths, requiring a temperature rise when using the inversion procedure of Vernazza et al. (1981). Other authors (e.g. Theurer et al. 1997b; Kalkofen et al. 1999; Ulmschneider 1999) argue that the piston used by Carlsson & Stein lacks sufficient high frequency power to simulate the physical sun.

While the shocks of Carlsson & Stein can explain the absence of chromospheric heating in the non-magnetic internetwork, observations clearly demonstrate the presence of heating in the magnetic chromospheric network for which several mechanisms have been suggested (e.g., von Uexküll et al. 1989; Goodman 1996; De Pontieu et al. 2001) but the final understanding should come from refined observations. Theurer et al. (1997a,b) suggest that the granules, buffeting the vertical magnetic field, create slow compressive waves that travel upward along the magnetic field and dissipate in the chromosphere thereby heating the chromospheric network (as shown in Fig. 1.6) much like the old shock wave theory predicted by Bessey & Kuperus (1970).

### 1.5.3 The complete picture

Of course the real chromosphere differs from the symmetric and stationary picture as presented in Fig. 1.6. A more complete summary of the physical processes is shown in Fig. 1.9. When the upflow stops below a small granule, a deep downflow follows called a “finger”. These fingers can drive large granule fragmentation (Rast 1995) and cause ‘acoustic events’, collapsing blasts that kill off small granules and may produce the upwards travelling shocks into the chromosphere (Hoekzema & Rutten 1998; Hoekzema et al. 1998; Skartlien 1998) where they turn into internetwork grains. Hoekzema et al. (2002) show this to happen only very rarely.

Also fluxtubes are unlikely to be standing perfectly upright causing all kinds of variation in the angle at which they are viewed. The often ignored spicules are visible as fast changing fibrils best seen at the solar limb (Beckers 1968). The spicules can be explained either by upward traveling shocks in fluxtubes when they are embedded in strong granular downflows (e.g., Hollweg 1982; van Ballegoijen et al. 1998; De Pontieu et al. 2001) or by magnetic channelling of downward conductive heat flow from the corona that cannot be disposed of by radiative losses only generating thermal motions (Kuperus & Athay 1967; Kopp & Kuperus 1968; Bessey & Kuperus 1970). The strongest of the upward travelling shocks that cause the bright internetwork grains may also excite canopy waves that travel back along the network tubes.

---

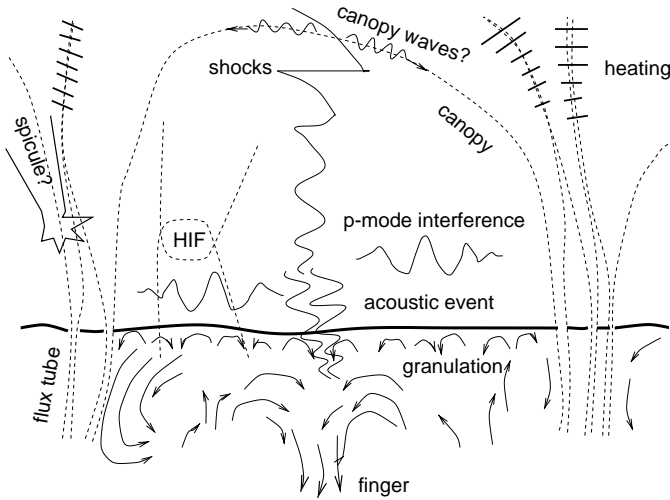


Figure 1.9: Cartoon, showing a more accurate picture of the physical processes occurring in the vertical slice of Fig. 1.6. Convective flows are shown as arrows, magnetic field lines are dashed, the wavy lines are oscillations and waves while the hatching shows the chromospheric heating, HIF is horizontal inter-network field. The analysis in chapter 5 shows that yet another ingredient, atmospheric gravity waves, must be added. From Rutten (1998).

Also, the internetwork is not completely free of magnetic field. While newly emerging flux in the form of ephemeral regions tends to be collected in the network, a weaker 'salt-and-pepper' background is present with single patches extending between 2 and 10 arcsec (Livingston & Harvey 1971). The properties of this internetwork magnetic field are still badly known. The magnetic field strength is likely to be below a kilogauss (Keller et al. 1994; Lin 1995; Wang et al. 1995; Lin & Rimmele 1999, e.g.,) while Lites et al. (1996) also found horizontal internetwork field (HIF), small transient patches containing weak horizontal field that may mark flux emergence (but are yet too weak to be called ephemeral region).

### 1.5.4 Why study the solar chromosphere?

The solar chromosphere is so interesting because it lies between the well studied "cool" photosphere and the "hot" magnetized corona. The chromosphere is the critical boundary layer which determines the corona to a large extent. It is the layer where the plasma-dominated photosphere goes over into the magnetically dominated corona. Also, the evasive magnetic canopy, where magnetic pressure equals gas pressure, is situated inside the chromosphere. Studying the chromosphere and its interaction with the surrounding layers is crucial for our understanding of the solar

atmosphere. In particular the study of local oscillations and waves will provide the answer to the question of chromospheric heating.

Groundbased observations always are restricted to short ( $< 12$  hrs) durations, are often troubled by seeing (earth atmosphere ripples due to heating of both ground and air), and of course, cannot be extended into the UV. Therefore satellites such as TRACE are required to understand the physics of the chromosphere which is like a stone of Rosetta for magnetic activity in stellar atmospheres and accretion disks.

## 1.6 This thesis

This thesis contains, beside this introduction, 5 chapters detailing my work during the years 1998-2002 on the solar chromosphere structure and dynamics. As explained above the chromosphere plays a critical role in the magnetic activity of the sun and largely determines the properties of the corona. That is why this study includes photospheric flows, which influence the magnetic and chromospheric network as well as waves that travel through the chromosphere into the transition region. In this thesis the chapters are not ordered chronologically in time of writing but according to the height they address in the solar atmosphere.

In Chapter 2 a correlation tracking technique is presented that can allow the TRACE satellite to be used for studying the photospheric (super)granular flows and the connection between these flows and the chromospheric network (See Fig. 1.5). The validity of this technique is shown by a test on a 4.5 hr white light observation. In chapter 3 this technique is applied on a week-long TRACE observation. Comparing the results with current models and ideas about meso- and supergranules we find that the flux in the chromospheric network can be maintained by emerging ephemeral regions that are swept as passive particles towards the supergranular boundaries by the horizontal flows. We also find a conformation of the smaller supergranular size as suggested by Hagenaar et al. (1997).

In chapter 4 TRACE UV image sequences are used to study the oscillations in the solar chromosphere, and here most of the techniques referred to in the other chapters are developed. A comparison with previous Ca II studies has been added to place the article into context. It confirms much of the information provided in the present introduction, e.g. the dichotomy between network and internetwork in oscillatory behaviour, the presence of a low-lying canopy, and the result that internetwork consists mostly of upward propagating acoustic waves that show signs of steepening into shocks. Also, we have found strong evidence for internal gravity waves at which we take a closer look in chapter 5.

The next chapter (chapter 6) follows the chromospheric oscillations into the TR. Using multi-telescope (TRACE/SOHO/VTT) and multi-wavelength (Ca II, Ly  $\alpha$ , Ly  $\beta$ , higher Lyman lines and the 1216, 1600, 1700 Å continua) observations we show that

---

---

while layers close in formation height show high correlation, there is little correlation between the oscillations seen in the TR and the lower chromosphere. This can be explained by having a magnetic canopy in the higher chromosphere that changes the dynamics of the oscillations providing a solid observational basis for the picture in Fig. 1.9

*Acknowledgements.* J.M. Krijger is much indebted to J. Kuijpers, M. Kuperus, J. Petrovic, P. Sütterlin and “too many students to mention” for comments. This research is funded by The Netherlands Organization for Scientific Research (NWO).



# Chapter 2

## Photospheric flows measured with TRACE

**Abstract.** We analyse white-light image sequences taken with the *Transition Region and Coronal Explorer* (TRACE) using an optimised local correlation tracking (LCT) method to measure the horizontal flows in the quiet solar photosphere with high spatial (1 arcsec) and temporal (5 min) resolution. Simultaneously taken near-ultraviolet images from TRACE confirm that our LCT-determined flows recover the actual supergranulation pattern, thus proving that the topology of the horizontal flow distribution and network assembly may be studied from long-duration TRACE white-light sequences with our method.

## 2.1 Introduction

Convective flows dominate the structure of and the energy transport in the outer parts of the Sun up to the deep photosphere. Understanding the convective flow and its interaction with the magnetic fields is important since convective motions are believed to drive many important processes on the sun, e.g., (i) – the solar dynamo through interaction with solar rotation, (ii) – the  $p$ -mode oscillations that are used to probe the solar interior, (iii) – magneto-hydrodynamic waves which supply energy to the chromosphere, and (iv) – foot-point motions that lead to magnetic reconnection which may heat the corona.

The most visible product of convection is the solar granulation with a characteristic scale of 1000 km, life-time of about 10 min (e.g., Bray et al. 1984), and easily recorded in broad-band images. The solar granulation is reproduced remarkably well in numerical simulations (e.g., Stein & Nordlund 1998). The larger granulation scales, meso- and supergranulation, are less understood. The existence of convection at the mesogranular scale is still in debate (e.g., Rieutord et al. 2000; Ploner et al. 2000), while study of the supergranular pattern is difficult because it does not show directly in white light whereas the magnetic network and the chromospheric brightness network map supergranular cell boundaries only incompletely. The new technique of time-distance helioseismology (Duvall et al. 1993) has become very popular for studying the supergranulation, but results in controversial findings (e.g., Hathaway et al. 2002) which require further investigation. The supergranule scales are still debated (see Beck & Duvall 2001), with the current estimates for the length scale between 13 Mm and 35 Mm (e.g., Hagenaar et al. 1997) and a lifetime between 15 hours and 52 hours depending on scale (e.g., Wang & Zirin 1989; Simon et al. 1995).

As shown by Rieutord et al. (2001) the flow speeds determined from brightness changes describing granular motions are an indication of the horizontal motion of the associated matter. Tracking this granular structure enables determination of the longer-lived and wider horizontal flows (November & Simon 1988) and one may so study the assembly and topological evolution of the magnetic network at these scales.

Different attempts (e.g., Leighton et al. 1962; Brandt et al. 1994; Roudier et al. 1999; Rieutord et al. 2000) have been made to determine quiet-sun surface flows from ground-based observations. These observations were limited by small field of view (FOV), short duration, and the presence of seeing which hampers precise flow evaluation. Seeing is best avoided by putting telescopes in orbit. The SOUP instrument on-board Spacelab 2 collected a sequence of too short a duration (28 min) to study supergranular ( $>15$  hrs) pattern changes (Simon et al. 1988). The MDI instrument on-board the SOHO satellite can observe for much longer duration but is limited by the fixed pointing of its high resolution field. The line-of-sight velocity images obtained by MDI are much used with time-distance helioseismology (e.g., De Rosa et al. 2000; Hathaway et al. 2002).

Image sequences from the TRACE satellite (Handy et al. 1999a) do not suffer from seeing and have a somewhat better resolution (1 arcsec) than MDI (1.3 arcsec). TRACE offers a large FOV ( $512 \times 512$  arcsec<sup>2</sup>) and long duration observations (up to a week) by following a given area on the solar surface by correcting for solar rotation. Also, TRACE permits quasi-simultaneous observations in both white light (low photosphere) and near-ultraviolet (upper photosphere) wavelengths. The bright chromospheric network visible in the near-ultraviolet wavelengths can be used to show the location of the magnetic network, which is governed by

the flows, in the absence of magnetograms allowing a direct check. However, so far it was not clear whether the TRACE resolution of 1 arcsec is good enough to obtain reliable flow estimates since it resolves the granulation which is to be used as flow tracer only partially.

In this paper we test whether it is possible to use the TRACE white light observations despite their low resolution for measuring horizontal velocity fields, by optimising the LCT method of November & Simon (1988) and using “isotropic divergence” (Roudier et al. 1999; Rieutord et al. 2000). The (dis)advantages of the LCT and other tracking techniques used by different authors are presented and discussed in Roudier et al. (1999). For a discussion of previous studies using feature tracking, see Rieutord et al. (2000). Our test proves that our modified LCT method with optimised parameters and data reduction can be used to derive horizontal flows from longer TRACE white-light image sequences.

The organisation of the paper is as follows. The observations and reductions are presented in the next section. In Sect. 2.3 we display the results of the analysis with the conclusions following in Sect. 2.4.

## 2.2 Observations and reduction

### 2.2.1 TRACE sequence

We use a TRACE image sequence taken on October 14, 1998 between 8:12–12:00 UT. TRACE observed a very quiet rectangular area of the solar surface at disk center (see Fig. 2.1) in three ultraviolet passbands (centered at  $\lambda = 1700 \text{ \AA}$ ,  $1600 \text{ \AA}$ , and  $1550 \text{ \AA}$ ) and a broadband white-light passband. A nominal cadence of 21 sec for each individual passband (but longer occasionally) was used. Only  $512 \times 512 \text{ pixel}^2$  of the  $1024 \times 1024 \text{ pixel}^2$  TRACE CCD camera with 0.5 arcsec pixels (366 km on the sun) were read out due to telemetry limitations. The satellite pointed at a fixed location on the apparent solar disk without following solar rotation during the observation. The observations are specified in Table 2.1. Figure 2.2 shows as example pair of white-light and  $1700 \text{ \AA}$  images.

In this analysis only the lower half of the observed field ( $256 \times 128 \text{ arcsec}^2$ ) was used, due to computer resource restrictions. The images were reduced following standard procedures<sup>1</sup> (dark current subtraction, flat field correction). The sequences were subsequently aligned to remove solar rotation and satellite jitter using cross-correlation aligning the ultraviolet images to other images of the same passband and to the other passbands within a few tenths of a pixel. Differential rotation across the field during the entire sequence had only a small effect (0.4 pixel) and was neglected. Due to solar rotation and satellite jitter only part of the FOV was fully sampled ( $452 \times 246 \text{ pixel}^2$ ,  $226 \times 123 \text{ arcsec}^2$  or  $165 \times 90 \text{ Mm}^2$ ). More details on these data and its reduction are given in Krijger et al. (2001a). More information on reducing TRACE data is available in the TRACE Analysis Guide<sup>2</sup>.

---

<sup>1</sup><http://www.lmsal.com/solarsoft/>

<sup>2</sup><http://diapason.lmsal.com/~bentley/guides/tag/>

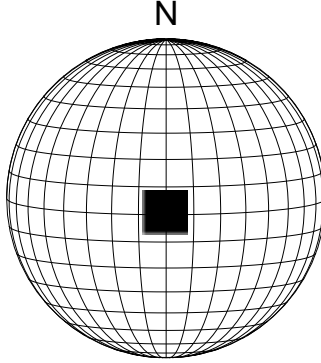


Figure 2.1: Solar location of the field observed with TRACE on October 14, 1998, slightly off disk center. Only the lower half of this field was used for the analysis presented in this paper. The grid shows heliocentric longitude and latitude.

Table 2.1: TRACE observations used in this paper

date	October 14, 1998
program sequence	TDT.any_frames
image size [pixel]	$512 \times 512$
image size [arcsec]	$256 \times 256$
used image size [pixel]	$452 \times 246$
used image size [arcsec]	$226 \times 123$
size pixel [arcsec]	0.5
size pixel [km]	366
number of images	611 per passband
$X_{\text{cen}}, Y_{\text{cen}}$ [arcsec]	$-13, -82$
$L_{\text{cen}}, B_{\text{cen}}$ [deg]	$-0.77, 1.04$
duration [UT]	08:12–12:00
cadence [s]	21.8625
exposure 1700 Å [s]	2.0480
exposure 1600 Å [s]	1.0239
exposure 1550 Å [s]	9.7400
exposure white light [s]	0.0064

## 2.2.2 Local Correlation Tracking

In order to take out the five-minute oscillation, all horizontal movements faster than  $4 \text{ km s}^{-1}$  were removed from the white-light sequence by 3D Fourier filtering (Title et al. 1989).

Subsequently, each individual white-light image was enlarged by a factor of 4 (using interpolation) in order to increase the number of points used in subsequent correlation com-

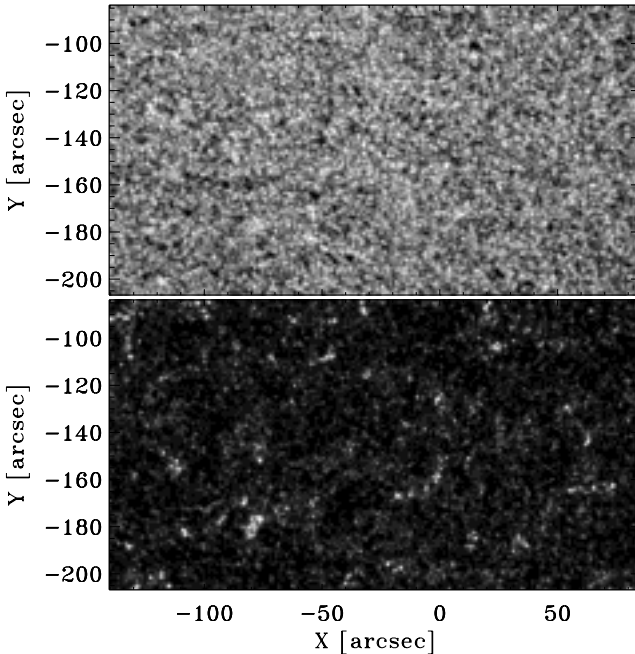


Figure 2.2: Top: sample white-light image taken by TRACE at 10:03 UT, Oct 14 1998. With a resolution of only 1 arcsec TRACE only resolves the larger granules. Smaller granules can jointly appear erroneously as large granules when close enough. No large-scale or magnetic structures are discernable. Bottom: corresponding 1700 Å image taken by TRACE 2 seconds earlier. The brightest features belong to the chromospheric network. The latter stands out more clearly in the time-average display at bottom-left in Fig. 2.6. Axes:  $X$  and  $Y$  in arcsec from disk center.

putations since the noise in the velocity measurements is proportional to  $1/\sqrt{N}$  where  $N$  is the number of points used for the correlation. A test on blurred high resolution ground-based observations showed that this enlargement allows better recovery of the actual velocity fields.

The method used below is described in more detail in Roudier et al. (1999). After enlargement the images were filtered using a 1 arcsec<sup>2</sup> Gaussian window. Tests showed that a larger window samples multiple granules and measures only their group-averaged motion, while a smaller window measures details below the resolution of TRACE (1 arcsec) and generates meaningless results. Subsequently, the images were transformed into a binary map of granules, using local curvature of the intensity pattern to identify granules following Strous (1995).

Horizontal velocity fields were calculated using these binarised maps with the LCT method of November & Simon (1988) with 5 min resolution. Using LCT on binarised data was named the LCT<sub>bin</sub> method by Roudier et al. (1999). For each 5 min temporal window 15 sequential images were used. A test showed that using an artificial cadence of  $\sim 1$  min (3 images per

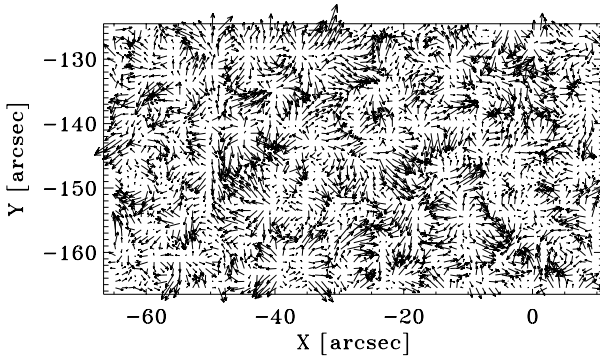


Figure 2.3: Horizontal flows in a partial cutout from the measured horizontal velocity field at 1 arcsec resolution between 10:10–10:15 October 14 1998. Each arrow shows the direction and magnitude of the velocity at a particular point with 1 arcsec length corresponding to  $0.25 \text{ km s}^{-1}$ . Axes:  $X$  and  $Y$  in arcsec from disk center.

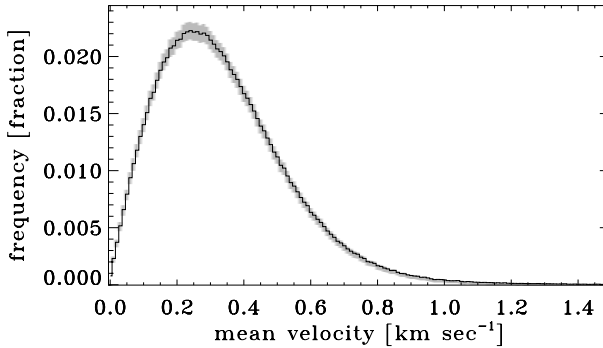


Figure 2.4: Histogram of all measured mean horizontal velocities (both in  $x$  and  $y$  direction), with  $3\sigma$  estimates (shaded contours). Most velocities are below  $1 \text{ km s}^{-1}$ , with a maximum around  $0.25 \text{ km s}^{-1}$ .

temporal window) instead of 21 sec yields similar results. The period of 5 min was used as a compromise between the (mean) lifetime of the granules and noise in the resulting flow maps.

Figure 2.3 shows a sample result. Large-scale ( $\sim 7 \text{ Mm}$ ) diverging and converging areas are visible as a mesoscale pattern. The statistical distribution of the measured flow speeds is shown in Fig. 2.4. The lower cut-off is due to the angular resolution set by the TRACE CCD pixel size. Most mean velocities are below  $1 \text{ km s}^{-1}$ . This distribution is shifted towards the lower velocities compared to the granular mean velocity found in Roudier et al. (1999), due to the tendency of the  $\text{LCT}_{\text{bin}}$  method of smoothing out the smaller and faster patches in the velocity fields.

After the computation of successive mean-flow maps covering the whole sequence duration, one can insert artificial tracers or “corks” that follow horizontal motions over a longer

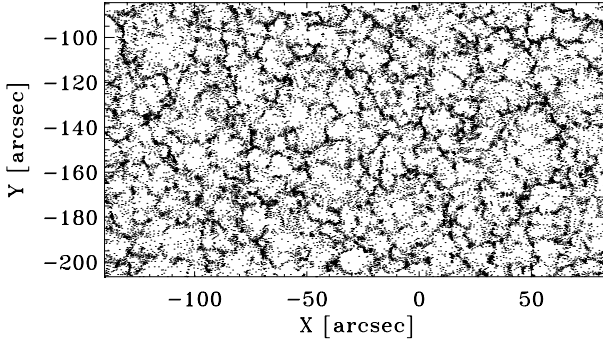


Figure 2.5: This plot shows the final positions of about 30 000 “corks” or tracers after 4 hours, that were initially distributed regularly and allow to freely flow on the velocity fields. Some tracers have not yet reached their final destination, but large scale structures are visible. Axes:  $X$  and  $Y$  in arcsec from disk center.

lifetime than that of individual granules, and so mapping longer-lived flows (Simon et al. 1988). Figure 2.5 shows the final position of such corks, inserted at the start of the flow-map sequence. Large ( $\sim 22$  Mm) cell-like closed structures are visible, filled with smaller ( $\sim 7$  Mm) cells that are less well outlined. The large cells correspond to the supergranular network as we demonstrate in Figs. 2.6 and 2.7. The smaller structures result at least partially from the short sequence duration by showing corks that have not yet reached their final supergranular-cell boundary destination.

### 2.2.3 Isotropic divergence

A quantity that can be derived from flow patterns is the horizontal divergence  $\nabla \cdot v_{xy}$  which furnishes another presentation of the surface flows. Our interest is into sources of divergence/convergence, those locations where matter presumably appears at the surface by flowing upward (divergence) and where matter presumably disappears from the surface by flowing downwards (convergence), respectively. However, using the classical divergence calculation, one also finds a high divergence or convergence value at a particular location when the surrounding area as a whole is horizontally accelerating or decelerating. We therefore employ the “isotropic divergence” instead (Rieutord et al. 2000). We briefly describe both methods here.

Calculating the divergence at a certain point in a regular grid is a straightforward procedure by summing the difference in velocity (in orthogonal directions) of the 4 adjacent points. The mathematical definition for the classic divergence at location  $(x, y)$  in a regular discrete grid is:

$$\frac{v_x(x+1, y) - v_x(x-1, y) + v_y(x, y+1) - v_y(x, y-1)}{2W}, \quad (2.1)$$

with  $W$  the distance between two gridpoints and  $v_x, v_y$  the respective velocity components. The averaged horizontal divergence over the entire duration of the observation is shown in the top-left panel of Fig. 2.6.

The isotropic divergence is defined in each point as the sum of the difference (normalised by the distance) of the projected vector components of the velocity on the axis of the symmetrical points relative to the central one, in all the directions and computed for the two gridpoint-rings around this central point (8 points for the first ring and 16 points for the second ring). The mathematical definition for the isotropic divergence in location  $(x, y)$  is:

$$\sum_{s_x=-2}^2 \sum_{s_y=-2}^2 \frac{s_x v_x(x+s_x, y+s_y) + s_y v_y(x+s_x, y+s_y)}{2W(s_x^2 + s_y^2)}, \quad (2.2)$$

with  $s_x, s_y$  the gridpoint distance from  $x, y$  in their respective directions, which are not allowed to be zero at the same time (*i.e.*, the velocity in the central point is not used for the divergence calculations). The resulting amplitudes peak at isotropic divergence/convergence sites such as exploding granules and sink holes. The averaged horizontal isotropic divergence is shown in the middle-left panel of Fig. 2.6.

## 2.3 Results

### 2.3.1 Divergence

Both the classic and isotropic divergences were evaluated and subsequently averaged over the total duration of the observation (8:12–12:00 UT). The results are shown in the two upper panels in the lefthand column of Fig. 2.6. Using isotropic divergence yields a coarser pattern with a clearer indication of cellular structure at supergranular scale which is outlined by darker-than-average boundary segments.

### 2.3.2 Chromospheric network

The capacity of TRACE to simultaneously observe in the ultraviolet and the white-light allows us to compare the cork collection sites in Fig. 2.5 and the coarse grid-pattern of convergence sites in Fig. 2.6 to the actual structure of the chromospheric network. The pertinent ultraviolet observations from TRACE are described in more detail in Krijger et al. (2001a). The TRACE 1600 Å and 1700 Å passbands show very similar features as Ca II K<sub>2V</sub> movies from ground-based telescopes (Rutten et al. 1999). The bottom-left panel, Fig. 2.6 shows the temporal average of the entire 1700 Å sequence. The chromospheric network stands out much clearer in this time-average display than in the snapshot image in the lower panel of Fig. 2.2 because the intermittent internetwork features (mostly due to the chromospheric three-minute oscillation) average away while the more persistent network features are enhanced.

### 2.3.3 Spatial comparison

Comparison of Fig. 2.6 with Fig. 2.5 shows that the regions with highest cork density (Fig. 2.5) correspond closely to the bright ultraviolet network (bottom-left panel of Fig. 2.6). Similarly, comparing the temporally averaged divergences with the 1700 Å temporal average image (left-hand panels of Fig. 2.6) indicates spatial correspondence between the (dark) converging areas

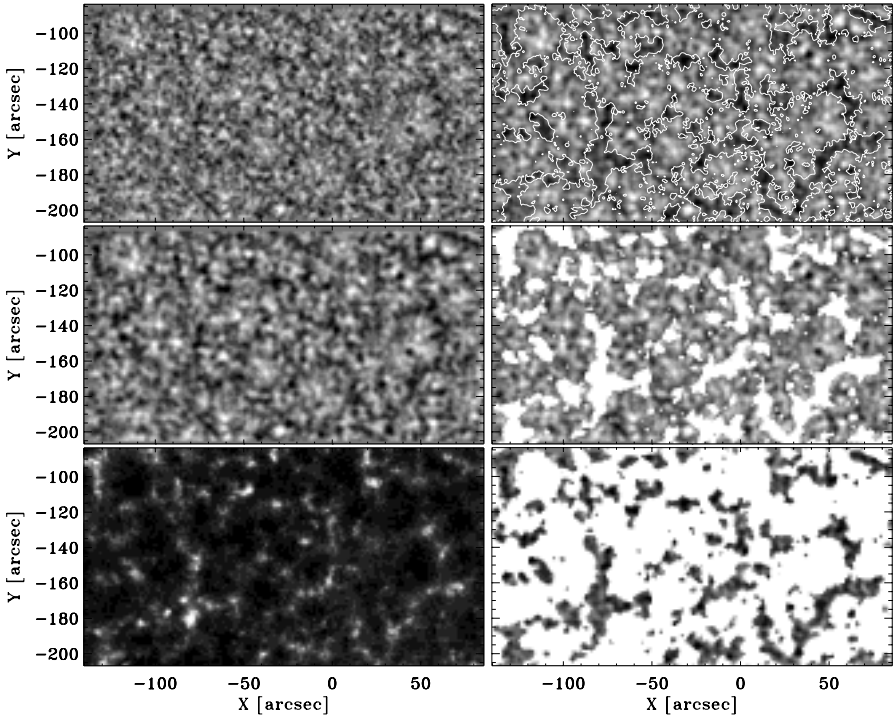


Figure 2.6: Top left: classic divergence defined by Eq. (2.1) averaged over the entire duration (228 min) of the observation. Bright areas indicate locations where the flows are diverging, dark areas indicate converging flows. Middle left: same as first panel, but showing isotropic divergence as defined by Eq. 2.2. Large scale structures become more distinct. Bottom left: the average of the 1700 Å sequence taken at the same time and location. The greyscale is logarithmic in order to bridge the large contrast. Top right: again showing the time-averaged isotropic divergence but now overlaid with the contours of the bright network from the bottom-left panel. A clear correlation between the dark converging areas and the bright network can be seen. Middle and bottom right: split of the top-right panel into internetwork-only and network-only displays, using a mask defined by the network contours. The split produces yet clearer visualisation of the spatial correlation between the dark converging areas and the bright network. Axes:  $X$  and  $Y$  in arcsec from disk center, all panels show the same subfield.

and the bright chromospheric network. The righthand panels of Fig. 2.6 visualises this correlation by showing different comparisons between the isotropic divergence and the 1700 Å image. In the top-right panel the isotropic divergence is shown overplotted with the network contours of the 1700 Å image. The two lower panels in the righthand column show the difference directly.

Finally, the spatial correlation between convergence sites and chromospheric network is illustrated in Fig. 2.7 by plotting 1700 Å brightness versus the average divergence as a scatter diagram. It shows that most bright network features are located at convergence (negative

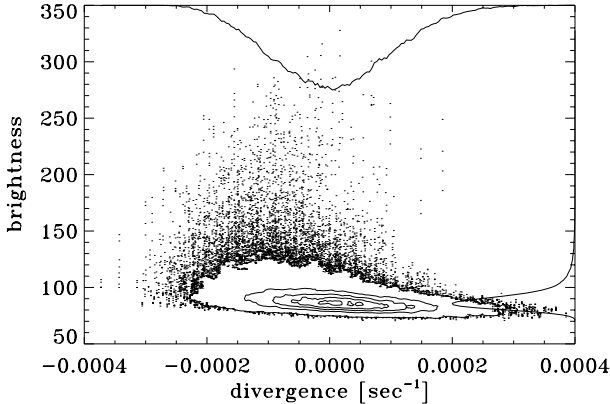


Figure 2.7: Correlation between average 1700 Å brightness and average velocity field divergence shown as a pixel-by-pixel scatter plot, with density contours replacing individual points where they become too close. The curves along the axes measure the first moments per row and column, respectively. The locations with the brightest network (upward tail of the scatter cloud) correspond to negative divergence in the flow field.

divergence) locations. This proves that the surface flows which we have measured with our correlation tracking indeed represent long-term supergranular motions, even though Fig. 2.5 shows that not all corks have reached their final position in the supergranular cell borders.

## 2.4 Conclusions

We have demonstrated that, although TRACE resolution (1 arcsec) is not good enough to fully resolve the solar granulation, it does suffice to determine the flow patterns over the solar surface that produce and control the topology of the solar network. Using the  $LCT_{bin}$  method high spatial (1 arcsec) and temporal (5 min) resolutions can be obtained. These resolutions have not been achieved before on seeing-free data with such a large FOV ( $226 \times 123 \text{ arcsec}^2$ ) and long duration (228 min). TRACE allows a FOV up to  $512 \times 512 \text{ arcsec}^2$  and observations centered at a given (co-rotating) solar location up to a week duration. Combination of such measurements with our method allows study of the distribution and network assembly over long time scales with longer TRACE WL sequences. These higher temporal and spatial resolutions allow a gain in the analysis of the signal (velocity) from high to low frequencies in the two domains. In particular, it helps to distinguish the smoothing effects of the data reduction and analysis from the solar flow fields at medium and low frequencies (spatial and temporal) and to learn about the influence of the smaller scales on to the largest ones. Our approach allows us to locate more precisely the largest diverging amplitude events of the flow field and to correlate their evolution to the UV bright points (oscillations, motions, etc...) which are located on the border of the supergranule.

*Acknowledgements.* J.M. Krijger's research is funded by The Netherlands Organization for

Scientific Research (NWO). J.M. Krijger thanks the Observatoire Midi-Pyrénées for their hospitality and financial support during his visit there. We are indebted to R.J. Rutten for suggesting this research and many improvements to the manuscript and to referee J.G. Beck for his valuable comments.



# Chapter 3

## Photospheric flows measured with TRACE II. Network formation

**Abstract.** We analyse a 7-day (167 hrs) sequence of TRACE white light images with 1 arcsec angular resolution taken at 1 min cadence. The TRACE resolution and the one-minute cadence allows us to produce maps of the horizontal flow fields with high spatial (1 arcsec) and temporal resolution (5 min). The field of view of  $128 \times 128 \text{ arcsec}^2$  ( $\sim 93 \times 93 \text{ Mm}^2$ ) covers approximately the area of 10 to 30 supergranules and was followed during solar rotation. Magnetic flux was artificially inserted into the successive flow maps in the form of ephemeral regions with positive and negative polarity. The emergence rate of  $2 \cdot 10^{22} \text{ Mx hr}^{-1}$  with an average flux per region of about  $11 \cdot 10^{18} \text{ Mx}$  produces good reproduction of the chromospheric network as observed in simultaneously taken 1600 Å images. In addition, we show that quiet network can be maintained only if field elements of both polarities are inserted into the flow fields. Our analysis suggests that the network is fully replenished on time scale of a day and the lifetimes of the magnetic elements are of similar duration.

### 3.1 Introduction

This paper addresses the formation of the quiet-sun chromospheric network by inserting artificial magnetic elements in observed velocity in observed fields employing long-duration white light image sequences obtained with *Transition Region and Coronal Explorer* (TRACE) (Handy et al. 1999a).

The chromospheric network consist of chains of bright patches visible in ultraviolet (UV) or Ca II observations. Each patch corresponds to a concentration of magnetic elements in the photosphere with fluxes in the range of  $10^{18}$  Mx up to a few times  $10^{19}$  Mx and field strengths in the order of a kilogauss. These photospheric elements, commonly modelled as fluxtubes (e.g. Steiner et al. 1986), appear as the bright grains visible in high-resolution ( $\leq 0.5$  arcsec) Fraunhofer G-band (around  $\lambda = 430.5$  Å) images or movies (e.g. Muller et al. (1989); Title & Berger (1996); Berger et al. (1998); movies on the Dutch Open Telescope website at URL <http://dot.astro.uu.nl>). On snapshot images the chromospheric network can hardly be separated from the intermittent internetwork (corresponding to the supergranular cell interior) brightenings. However, when averaged over long-duration the network stands out since the transient internetwork features are averaged out.

Magnetic flux concentrations emerge intermittently in the internetwork in the form of ephemeral regions, i.e., bipoles with an average magnetic flux in the order of  $10^{19}$  Mx (Harvey-Angle 1993; Hagenaar 2001). After their initial emergence the bipoles split and quickly drift apart, after which the individual elements follow the (super)granular flow passively. The associated flux merges with the existing network or cancels when it encounters opposite-polarity network (Schrijver et al. 1997).

Simon et al. (2001, henceforth STW01) constructed a two-dimensional model describing horizontal supergranular flows in which they inserted artificial test particles continually in order to simulate the emergence of ephemeral regions. With this procedure they were able to steadily sustain a model representation of the magnetic network. So far, no observational sequence of sufficient duration exists to measure the actual horizontal flow fields over the supergranular lifetime of a few days which would enable a check of their model.

The SOHO and TRACE missions provide continuous solar observing capability with sufficient cadence, angular resolution and pointing stability to permit such long-duration flow mapping. A study of this type by Lisle et al. (2000, henceforth LRT00) employed a 6 day observation with the Michelson Doppler Interferometer (MDI) onboard SOHO, however in low-resolution mode with only 4 arcsec resolution. Details of the MDI instrument are given by Scherrer et al. (1995).

Another study of this type employing MDI was done by Shine et al. (2000a) using the high-resolution mode. Although MDI offers 1.3 arcsec resolution (0.65 arcsec pixels in high-resolution mode) at the required cadence, the duration of the observation was limited (as are all high-resolution mode MDI observations) by the fixed pointing of the high-resolution field with a size of about  $600 \times 600$  arcsec<sup>2</sup>. Solar rotation limits the maximum duration of a continuous observation to about two days for a solar area about 300 arcsec wide. TRACE has a somewhat better resolution (1 arcsec) and its pointing capability permits tracking a fixed solar surface area while it rotates around the sun. The foreshortening of such an area near the limb limits the effective duration of such sequences to 5–7 days. As shown in Krijger et al. (2002) TRACE white light images can be used to study horizontal velocity fields at a 5 min

temporal and 1 arcsec spatial resolution.

In this paper we use a continuous imaging sequence of 167.25 hr (almost 7 days) duration obtained by TRACE. When telemetry allowed 1600 Å images were obtained also and the cadence was increased to 30 sec, but we use only the regular 1 min cadence images. Using the  $LCT_{\text{bin}}$  method described in Krijger et al. (2002) optimized for TRACE white light observations we derive flow maps for this white light 167 hr sequence. In these flow maps we sprinkle corks in bipolar structures resembling ephemeral regions, similar to STW01, and allow these corks to passively flow in the measured flow maps. We use the 1600 Å images as a check for the resulting network.

The organization of the paper is as follows. The observations are presented in the next section. In Sect. 3.3 we briefly describe our local correlation tracking method. The cork insertion techniques are described in Sect. 3.4. In Sect. 3.5 the results of the analysis are presented with the discussion and conclusion following in Sect. 3.6 and Sect. 3.7, respectively.

## 3.2 Observations

Between 00:44 UT April 22, 2000 and 00:09 UT April 29, 2000 TRACE tracked a region mostly free of active regions across the solar disc along the equator between Stonyhurst latitude 45E and 45W for 167.25 hr. The satellite pointing was changed several times to correct for the solar rotation and keep the same region in the used field of view of  $768 \times 768 \text{ px}^2$  or  $384 \times 384 \text{ arcsec}^2$  since the TRACE pixel size is 0.5 arcsec. Only part of the CCD was used to increase the cadence to one white-light image per minute. During this time TRACE took white light continuum images at a cadence of at least 1 minute (EUV 171 Å images were taken as well but are not used in this study). Some gaps appear in the data due to planned synoptic observations or errors in the data transfer. There are only 9 gaps longer than 10 min, with the longest lasting 45 min. Since supergranular flows evolve on timescales of hours to days, these gaps do not impair the analysis presented in this paper. When sufficient bandwidth was available (about half the time) also 1600 Å passband images of the same field were taken at a 1 min cadence. See Fig. 3.1 for sample white light and 1600 Å images. The white light image shows the granulation with a small pore in the upper central part. The 1600 Å image shows the same field with the internetwork appearing dark with intermittent bright grains. The network is present as bright patches, corresponding to the non-visible magnetic network in the underlying photosphere.

The data was kindly made available to us by R.A. Shine. The co-alignment of the images was done by him and is described in more detail in Shine et al. (2001).

All white light images were carefully co-aligned using cross-correlation. The useful field of view shrank to  $287 \times 320 \text{ arcsec}^2$  area due to the effect of solar rotation and satellite drift. After a temporal gap the co-alignments retain an amount of uncertainty because solar patterns evolved during the temporal gap. The images of the other TRACE passbands were aligned to the white light by adjusting for the offset in pointing between different TRACE passbands and by interpolation from the derived white light displacements.

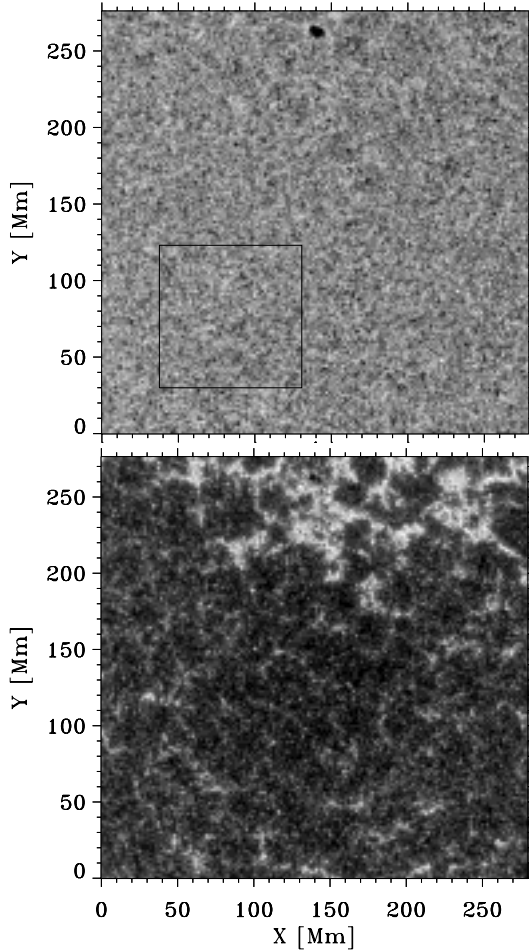


Figure 3.1: Left: sample TRACE white light image obtained at April 25, 2000, 13:55 UT. Right: sample 1600 Å passband image obtained 58 sec earlier. The solid box in the upper panel indicates the subfield for which we derived the velocity field.

### 3.3 Local Correlation Tracking

Due to computer memory limitation we only used a  $256 \times 256$  px<sup>2</sup> subfield corresponding to  $128 \times 128$  arcsec<sup>2</sup> or about  $93 \times 93$  Mm<sup>2</sup>, indicated by the solid contours in the upper panel of Fig. 3.1 We again use the same technique

We use the technique described by Roudier et al. (1999) and Krijger et al. (2002) and briefly describe it here. Each individual white-light image was four times enlarged through

interpolation. This data resampling makes the subsequent correlation computations more precise because the noise is proportional to the square-root of the number of samples used in the calculations. Each resampled subfield was then spatially filtered using an  $1 \text{ arcsec}^2$  gaussian window. Subsequently the local curvature of the intensity pattern was used to derive a binarized granule map following Strous (1995).

From each pair of successive images we measured the horizontal flow field by dividing the first image into  $1 \times 1 \text{ arcsec}^2$  ( $8 \times 8 \text{ px}^2$ ) patches and determining the vector translation of the patch (as marked by its fine structure) to its position in the next image through local cross-correlation. Using this Local Correlation Tracking (LCT) method of November & Simon (1988) on binarized maps was named  $\text{LCT}_{\text{bin}}$  by Roudier et al. (1999). To reduce noise we average these offsets over 5 min, a good compromise between granule lifetime and the resulting flow map noise. Any shift found outside the three-sigma limit due to cross-correlation failure was replaced by the average offset of the surrounding 8 patches. Conversion of the pixel translation vectors then resulted in sequence of flow field maps with a 5 min temporal and 1 arcsec spatial resolution. Missing maps due to data gaps were interpolated from the preceding and following velocity images. Various systematic errors related to the distance to the solar limb were corrected for by subtracting the average over each flow map as suggested by Shine et al. (2000a).

A useful property that can be derived from horizontal flow maps is the divergence:

$$\frac{v_x(x+1, y) - v_x(x-1, y) + v_y(x, y+1) - v_y(x, y-1)}{2W}, \quad (3.1)$$

at location  $(x, y)$  in a regular discrete grid, with  $W$  the distance between two gridpoints and  $v_x, v_y$  the respective velocity components. Divergence maps show where matter presumably disappears from the surface by flowing downwards (convergence) and where matter presumably appears at the surface by flowing upward (divergence). Figure 3.2 shows a sample flow and divergence map, respectively. Diverging and converging patterns at mesoscale ( $\sim 7 \text{ Mm}$ ) dominate the 5 min average flow map. The distribution of the flow speed magnitudes has a maximum around  $0.6 \text{ km s}^{-1}$  (Fig. 3.3<sup>1</sup>). It is nearly identical to the distribution found by Shine et al. (2000a). The lower limit detectability is determined by the (resampled) TRACE CCD pixel size, the cadence, and the sub-pixel accuracy of the LCT method.

## 3.4 Cork Insertion

Corks are hypothetical free particles that are allowed to flow freely in the horizontal flow maps (Simon et al. 1988). At each time step the position of the cork is updated according to the velocities on the location of the cork at that timestep.

The pioneering flow study of Simon et al. (1988) used data of such short duration (20 min) that the velocity field had to be extrapolated to a much longer duration. Later studies, e.g., Brandt et al. (1992) and Shine et al. (2000a) used data durations of several hours, still much shorter than the multi-day lifetime of supergranules. The long sequence used for this study

<sup>1</sup>Note that the amplitude of the flow speed derived in similar fashion by Krijger et al. (2002) was much smaller because an error was made in the numerical interpolation.

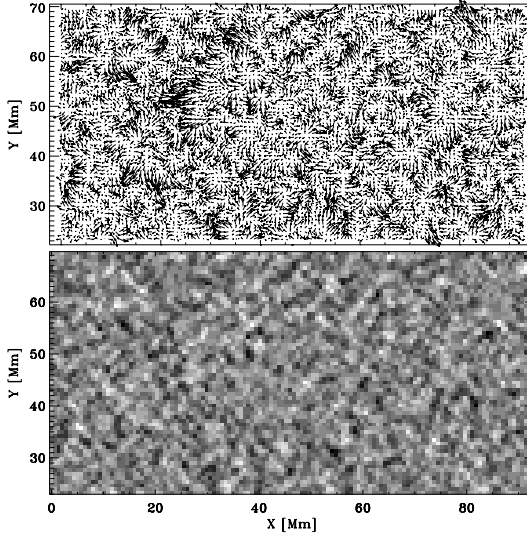


Figure 3.2: Top: sample flow map. Shown is the central half of the horizontal velocity field between 13:51 and 13:56 UT, 25 April 2000. Bottom: divergence map of the same horizontal velocity field. Converging areas where matter presumably disappears from the surface by flowing downwards are dark in greyscale, while diverging areas where matter presumably appears at the surface by flowing upward are bright. Axes: distance from the lower-left origin of the observational field of view in Mm.

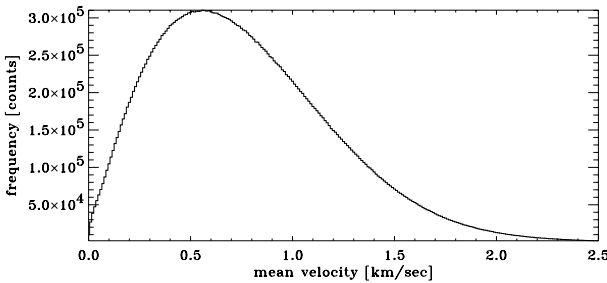


Figure 3.3: Distribution of the horizontal flow in the flow map sequence. The standard deviation is about equal to the thickness of the curve.

shows that the network and flow field evolve significantly over several days. The most common method of using corks is to insert all corks initially at regular spacing across the entire velocity field and then follow them as they flow. The results of this technique applied to our data is shown in Fig. 3.4. Each concentration of corks is indicated by a circle with an area proportional to the number of overlapping corks on the central location. After 90 hrs only a few very dense corks concentrations can be distinguished because the corks end up in strong

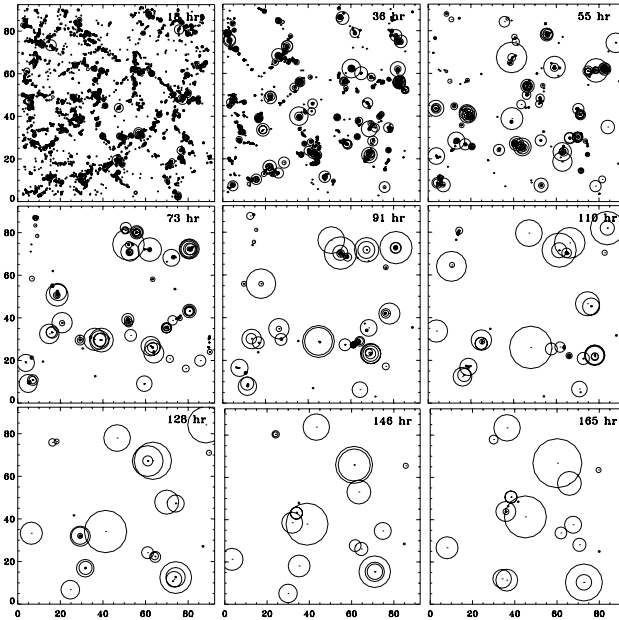


Figure 3.4: Evolution of an initially regular distribution of  $128 \times 128$  corks, each with a size  $0.1 \times 0.1 \text{ arcsec}^2$ . Overlapping corks are replaced by a circle with an area proportional to the overlapping number of corks. Time elapsed since the insertion of the corks is indicated in the upper right-hand corner of each panel. Axes are in Mm.

convergence points (“sinks”) or are moved outside our observed field. To study the magnetic network over a period as long as our observation, a more sophisticated cork insertion method is needed including cork cancellation due to opposite polarity.

We follow STW01 in comparing our cork insertion technique to the ephemeral active regions observed with MDI (Schrijver et al. 1997). Most of the solar magnetic flux emerges in the form of small bipoles, called ephemeral regions (Harvey-Angle 1993; Hagenaar 2001). After their initial emergence the bipoles split and quickly drift apart apparently floating passively on the (super)granular flow. Individual magnetic flux elements can be described as passive corks that follow the flow fields at each moment. According to this method, new corks are introduced in bipole structures similar to ephemeral regions consisting of two opposite-polarity clusters of corks. For comparison purposes we initially use the same values for the different parameters that are used in STW01. A cork possesses a position and a sign (either positive or negative). The structures are inserted at a random position in the centre two-thirds area of the field to avoid edge effects. The clusters are always separated by the same distance  $D$  (10 arcsec) and contain the same number of unipolar corks (20). The corks in each cluster are distributed in a Gaussian pattern with a standard deviation of 1 arcsec around the centre of the cluster. Figure 3.5 shows a typical sample of such a bipolar structure. After inserting the

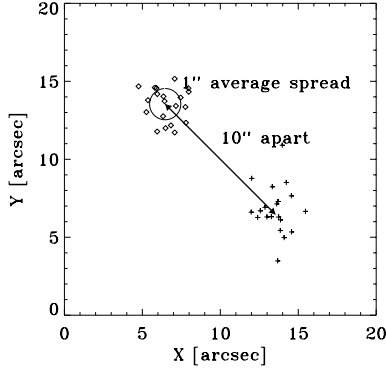


Figure 3.5: An sample of the type of bipolar cork structures inserted into the velocity field. The centres of the two clusters are always 10 arcsec apart. Each cluster consists of 20 corks of the same sign, while the corks themselves are randomly distributed in a random pattern with Gaussian cork density distribution with a standard deviation of 1 arcsec around the cluster centre location. Locations of corks with a positive sign are indicated with a plus, corks with negative sign with a diamond.

bipole structure we allow the corks to flow with the flow map speeds, sampling the flow maps at their 5-min intervals. If two corks of opposite sign come within 0.1 arcsec of each other they cancel against each other. Corks that are carried off the edges of the field are accumulated until enough corks of either sign are available to form a new bipole structure which is then inserted in the field again. This minimizes the loss of corks at the field edges.

According to Schrijver et al. (1997) magnetic flux concentrations emerge intermittently at a rate of  $3 \cdot 10^{21} \text{ Mx hr}^{-1}$  over the whole solar surface. The average magnetic flux of ephemeral regions is in the order of  $10^{19} \text{ Mx}$  (Harvey-Angle 1993; Hagenaar 2001). In STW01 where each cork represents a fluxtube with a 1500 G field strength and a magnetic flux of  $7.5 \cdot 10^{16} \text{ Mx}$ , the resulting flux for each a bipole structure would be of  $3 \cdot 10^{18} \text{ Mx}$ , which implies that on average 1000 ephemeral regions (each with  $3 \cdot 10^{18} \text{ Mx}$ ) appear each hour on the sun. To simulate this we insert a new bipolar structure every 40 min in our  $128 \times 128 \text{ arcsec}^2$  field.

Another possible source of magnetic flux are elusive weak internetwork magnetic patches or elements (Wang et al. 1995; Lin 1995; Zhang et al. 1998; Lin & Rimmele 1999). These magnetic elements play only a minor role in sustaining the magnetic network (Martin 1990; Wang et al. 1996; Zhang et al. 1998) and have been ignored.

## 3.5 Results

We use the cluster-insertion recipe presented in Sect. 3.4 to sprinkle bipolar cork groups onto the sequence of flow maps derived from the TRACE images described in Sect. 3.2. Figure 3.6 shows results concerning the total cork number evolution. The dotted curve in Fig. 3.6 shows the surviving cork number when the insertion of new clusters (every 40 min) is stopped after

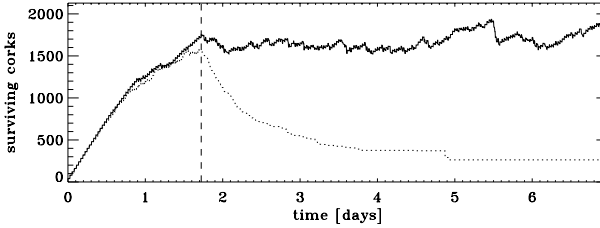


Figure 3.6: Solid curve: number of surviving corks as a function of time with new clusters of corks inserted every 40 min. Dotted curve: similar cork survival when the insertion is halted after 1.7 days (indicated by the vertical dashed line).

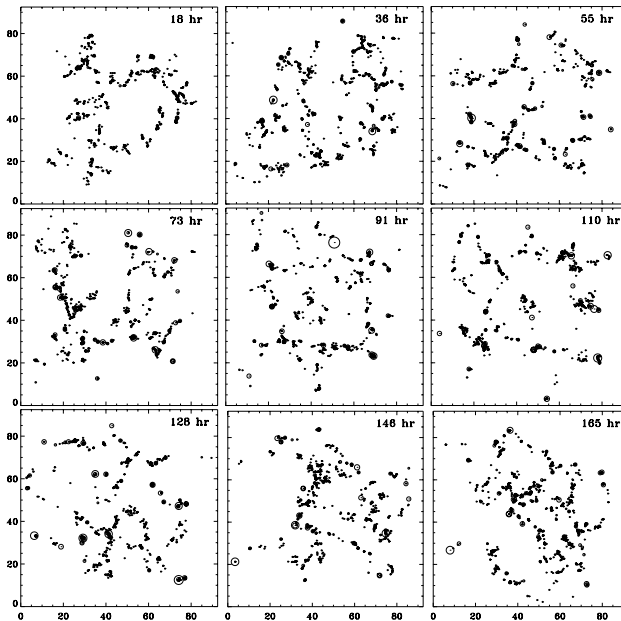


Figure 3.7: Formation of a statistically steady network, same format as Fig. 3.4. Corks were inserted into the observed flow maps in bipolar clusters as illustrated in Fig. 3.5 every 40 min. Axis units: Mm.

a total of 2480 corks are inserted after 1.7 days. The sudden drops mark occasions at which whole unipolar clusters meet and cancel against a cluster of the opposite sign.

The solid curve in Fig. 3.6 shows the surviving cork number when new clusters are inserted every 40 min during the whole duration of the experiment. After the initial cork build-up which takes about two days, a statistically steady state develops with  $N \approx 1600$ . An insertion rate of 40 corks every 40 min with  $N \approx 1600$  means that the network is fully refreshed every 1600 min or within almost 27 hrs, half the value found by SWT01. The average lifetime of

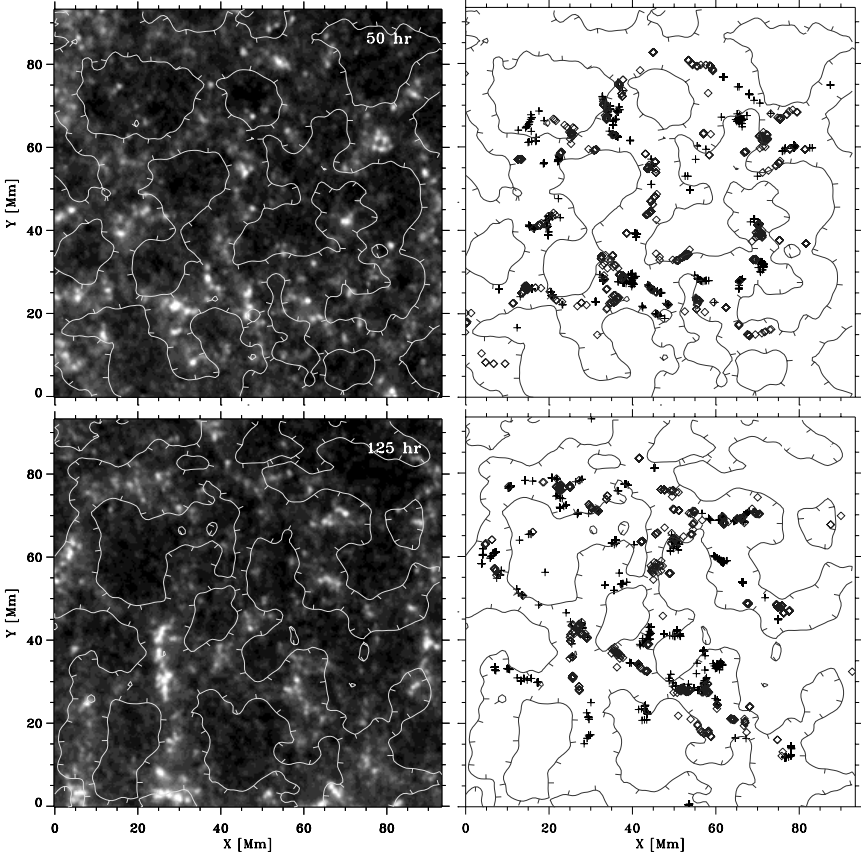


Figure 3.8: Greyscale images: sample temporal averages over 50 min duration TRACE 1600 Å images. The greyscale is logarithmic in order to bridge the contrast between network and internetwork. The contour curves mark the transition between divergence and convergence, with ticks directed to converging regions. The mid-times of the averaging periods are specified in the upper right-hand corner in minutes after the start of the observing run. Scatter plots: locations of the corks at mid-time of the averaging period with positive sign are indicated with a plus, corks with negative sign with a diamond. The zero divergence contours are repeated.

the corks must have the same order of magnitude. The modelled supergranular velocity field of STW01 resembles our and other observations, so only their granular displacement and assumed supergranule radii can make a difference. The granular displacement of STW01 that created a network most similar to other observations was 0.5 arcsec per 10 min, which equals an average speed of 0.6 km/sec, the same mean speed as found by us. As STW01 showed, the lifetime of corks decreases when supergranules are smaller as the corks travel smaller dis-

tances to the supergranule borders where they can be cancelled. Our findings support such a smaller supergranule radius, in agreement with the supergranule sizes found by Hagenaar et al. (1997) in the order of 13-18 Mm. Figure 3.7 shows the evolution of the network for this continuous cluster insertion similar to Fig. 3.4. The corks outline supergranular boundaries as the pattern evolves over time.

Figure 3.8 shows on the lefthand side two temporal averages of TRACE 1600 Å image sequences with durations of 50 minutes. Their mid-times are indicated in each panel. The contours that are superimposed on the average images show the smoothed zero divergence levels. On the right hand side the cork positions halfway the averaging interval are indicated by plus symbols for positive polarity corks, diamonds for negative polarity corks. The zero divergence contours are repeated for ease of comparison. The network coincides with the converging areas as shown in Krijger et al. (2002). There is also generally a spatial coincidence between the cork positions and the chromospheric network. However, it seems that the cork density is too low to fully reproduce the chromospheric network. The network in the outer part of the field is not well reproduced as the corks were all inserted in the inner two thirds of the field.

Figure 3.9 displays various cork properties. The first panel of Fig. 3.9 displays the cork lifetime  $\tau$  distribution for the corks. Corks that have not yet cancelled or are accumulated at the edges of the field at the end of our flow map sequence are ignored. This has little effect since these corks form only a minor fraction of the total amount of corks. While the cork is moved around by the instantaneous flow patterns, it travels over a total path length  $d_a$  between its insertion and its eventual cancellation. The second panel in Fig. 3.9 displays the total path length  $d_a$  distribution. From these two quantities we can derive the average actual velocity  $\langle v_a \rangle$  shown in the third panel in Fig. 3.9. Not surprisingly, the histogram of  $\langle v_a \rangle$  (Fig. 3.9d) shows as a sharply peaked distribution around the original mean solar flow velocity in Fig. 3.3. Yet corks are following a flow, which at small timescales resembles a random walk so the net displacement  $d_n$  is much smaller than the total path length  $d_a$ . The fourth panel of Fig. 3.9 displays the net displacement  $d_n$  distribution. The distribution of the net-speed  $v_n$ , derived from the lifetime  $\tau$  and the net displacement  $d_n$ , is displayed in the fifth panel of Fig. 3.9. The net displacements  $d_n$  in the fourth panel of Fig. 3.9 are ten times smaller than the actual displacement  $d_a$  in the second panel. This difference illustrates that the corks are moving chaotically in random-walk fashion due to the buffeting by individual granules.

Figure 3.10 shows the correlation between the lifetime  $\tau$  and the actual speed  $\langle v_a \rangle$  and the correlation between lifetime  $\tau$  and the net speed  $v_n$ , respectively. The former displays a sharply peaked profile around the mean value of the measured flows (Fig. 3.3). This can be explained with each displacement between timesteps being considered as a statistical draw from this velocity parent-distribution (multiplied by the timestep size). Corks with a long lifetime had more draws from this distribution and will most likely have an actual speed  $\langle v_a \rangle$  close to the mean of the parent-distribution. We find a weak inverse correlation between the net velocity  $v_n$  and lifetime  $\tau$ .

Our corks live considerably longer than the magnetic elements of LRT00 or Hagenaar et al. (1999) as can be seen in Fig. 3.9b. As our corks live until they are cancelled it is clear that besides cancellation an additional process must be responsible for shortening the lifetime of real magnetic elements.

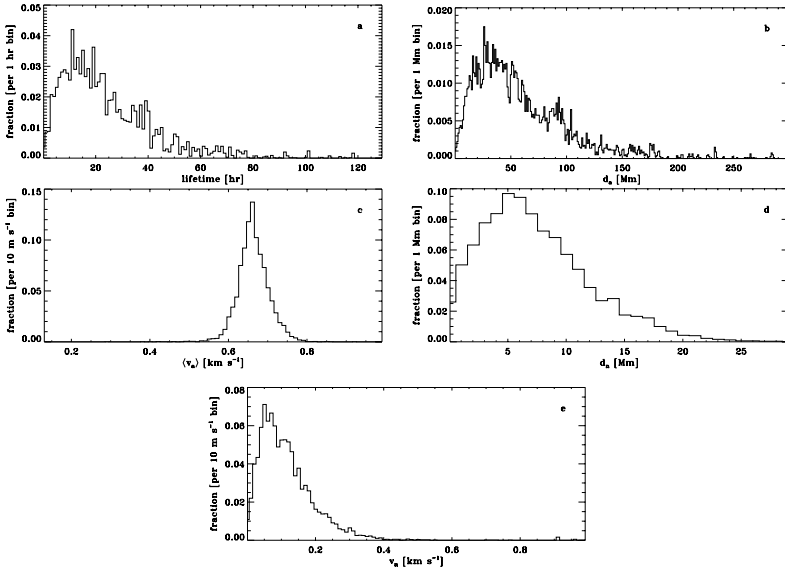


Figure 3.9: Histograms of a) cork lifetime  $\tau$ . b) actual cork travel distance measured along the cork path  $d_a$  c) actual cork speed  $\langle v_a \rangle$  along its path averaged over the lifetime of the cork d) net cork displacement  $d_n$  between insertion and cancellation; e) net cork speed  $v_n$

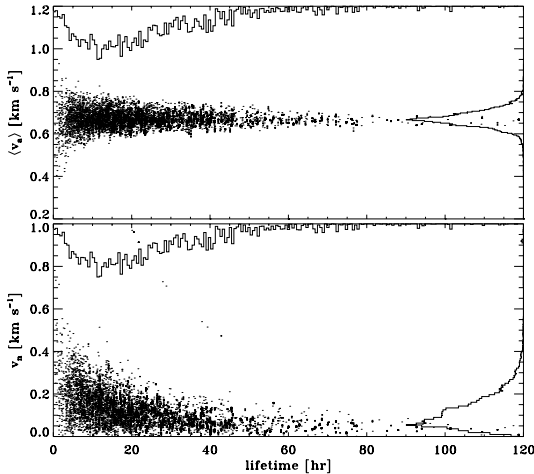


Figure 3.10: Scatterplot of the actual speed  $\langle v_a \rangle$  (top) and the net velocity  $v_n$  (bottom) against the lifetimes  $\tau$ , respectively. The solid curves show the inverted normalized distributions.

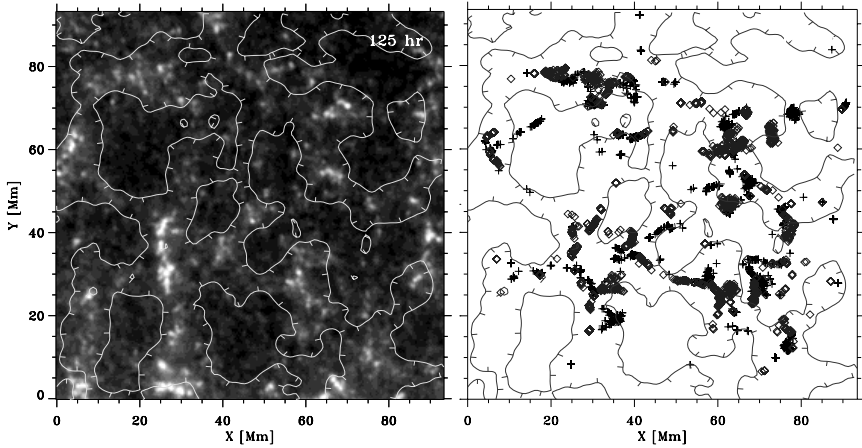


Figure 3.11: Similar to Fig. 3.8 but now with a 6 times higher flux emergence rate.

### 3.5.1 Increased emergence rate

So far we have used the same emergence rate as STW01, namely  $3 \cdot 10^{21} \text{ Mx hr}^{-1}$  over the whole solar surface. This corresponds to one ephemeral region of  $3 \cdot 10^{18} \text{ Mx}$  per 40 min in our  $128 \times 128 \text{ arcsec}^2$  field. Using a 3.5 days MDI observation Hagenaar (2001) found a much higher value for the flux emergence rate, namely  $2 \cdot 10^{22} \text{ Mx hr}^{-1}$ , with an average flux per region of about  $11 \cdot 10^{18} \text{ Mx}$ . To best match these observations we inserted a bipole structure every 25 min, each consisting of a total of 150 corks. This results only in an increase by a factor of 6, instead of  $\sim 6.7$ , because we are limited by our 5 min timestep resolution. The total number of corks in the steady-state network in our field increases from  $N \approx 1600$  to  $N \approx 7000$ . As expected,  $N$  does not increase proportionally to the six times larger insertion rate because the cancellation rate increases also. The lifetime  $\tau$  of the corks also decreases significantly. The lifetime distribution peak shifts to 14 hrs, the same period needed to replace all the magnetic field in the network found by Hagenaar (2001). Figure 3.11 displays a superposition similar to Fig. 3.8, but using the larger cork insertion rate. The actual chromospheric network is much better outlined by the corks than in Fig. 3.8. Again the network in the outer part of the field is not well reproduced as the corks were all inserted in the inner two thirds of the field.

## 3.6 Discussion

Use of the emergence rate of  $3 \cdot 10^{21} \text{ Mx hr}^{-1}$  and  $3 \cdot 10^{18} \text{ Mx}$  per ephemeral region, i.e. the values found by Schrijver et al. (1997), reproduces the network only sparsely. The higher emergence rate of  $2 \cdot 10^{22} \text{ Mx hr}^{-1}$  with an average flux per ephemeral region of  $\sim 11 \cdot 10^{18} \text{ Mx}$  found by Hagenaar (2001) produces much better reproduction of the actual network.

There are some differences between our study and the work of STW01. In STW01 the bipole cork structure was inserted within 5 arcsec of the centre of a randomly selected supergranule. In our method we do not know the position of the supergranules before inserting the corks into the velocity field. We have thus inserted the centre of the bipole structure at a random position anywhere in the inner two thirds of the measured velocity field. This insertion method can result in some corks being inserted closer to the supergranule boundaries and thus having to travel less far before reaching the network where there is a larger chance of being cancelled. Also, indications exist that ephemeral regions preferably appear close to the boundaries instead of the centre of supergranules (Harvey & Harvey 1995). However, STW01 tested the effect of increasing the area within the supergranule where the ephemeral regions could emerge and found it has little effect on the resulting network.

In STW01 the positions of the corks are updated in a 10 min timestep scheme, while in this paper we use a 5 min timestep. A test (not shown here) using 10 min average velocity maps showed that this does not have much effect on the cork statistics.

Following STW01, we have investigated the sensitivity of our results to variation of the parameter values. We find that varying the separation between clusters  $D$  from 5 arcsec to 25 arcsec does not have a great effect on the formed network. Changing the spread of the Gaussian pattern around the clusters centre from 1 arcsec to 0.5 arcsec and 2 arcsec also has little effect, although decreasing the spread of the clusters causes more corks to survive as they are less likely to encounter a cork with an opposite sign. Similarly to STW01, we find that the results are quite insensitive to the parameters of the cork insertion (except for the amount of corks per cluster).

There is an inverse correlation between the net velocity  $v_n$  and lifetime  $\tau$ . A similar but stronger correlation was seen by LRT00, but the lifetimes found by LRT00 are significantly shorter than ours. This might be due to correlation between the lifetime and the magnetic field strength of a magnetic element, as shown by LRT00 and Schrijver et al. (1997). Short-lived and weak magnetic elements occur more frequently than strong, long-lived elements. Since our corks all have the same amount of magnetic flux we do not include such short-lived magnetic elements in our modelling. Future modelling of magnetic elements using artificial corks will not only have to take magnetic sign but also magnetic strength of the corks into account.

### 3.7 Conclusion

We have measured solar surface flows at high spatial (1 arcsec) and temporal (5 min) resolution over much longer duration than has been achieved so far, sufficiently long to permit flow measurements over time scales covering the full range from granular to supergranular evolution. Confirming the work of STW01, we have shown the necessity to include cork polarity. We inserted magnetic flux into the supergranules in the form of ephemeral regions consisting of a number of corks with either positive or negative polarity. In order to maintain the network longer than two days continuous insertion of new magnetic elements is needed as older magnetic elements cancel when they encounter opposite polarity flux.

The network is fully replenished on a timescale of a day. The magnetic elements move in a random walk with a preferential direction towards supergranular boundaries as an effect

of being buffeted by individual granules. Also the lifetimes for our corks is in the order of a day, confirming the work of STW01 and Schrijver et al. (1997), preferring the smaller supergranules in the model of STW01. Our corks do not take into account the correlation between the magnetic strength and the lifetime of a magnetic element as found by e.g. Hagenaar et al. (1999).

Our work shows that chromospheric network is well reproduced by using emerging magnetic elements that passively flow in observed velocity fields when using the higher emergence rate of  $2 \cdot 10^{22} \text{ Mx hr}^{-1}$  with an average flux per ephemeral region of about  $11 \cdot 10^{18} \text{ Mx}$  as found by Hagenaar (2001). However, several improvements can be made to our cork evolution recipe, for example, by introducing weak internetwork fields or a reactive force for each cork related to the intensity of the magnetic field and not consider them a passive scalar or by removing limitations such as identical magnetic strength and infinite lifetime unless cancelled.

*Acknowledgements.* J.M. Krijger's research was funded by The Netherlands Organization for Scientific Research (NWO). We also would like to thank R.A. Shine for making the aligned data available to us. We are indebted to R.J. Rutten for many improvements to the manuscript.



# Chapter 4

## Dynamics of the solar chromosphere III. Ultraviolet brightness oscillations from TRACE

**Abstract.** We analyze oscillations in the solar atmosphere using image sequences from the *Transition Region and Coronal Explorer* (TRACE) in three ultraviolet passbands which sample the upper solar photosphere and low chromosphere. We exploit the absence of atmospheric seeing in TRACE data to furnish comprehensive Fourier diagnostics (amplitude maps, phase-difference spectra, spatio-temporal decomposition) for quiet-Sun network and internetwork areas with excellent sampling statistics. Comparison displays from the ground-based Ca II H spectrometry that was numerically reproduced by Carlsson & Stein are added to link our results to the acoustic shock dynamics in this simulation. The TRACE image sequences confirm the dichotomy in oscillatory behaviour between network and internetwork and show upward propagation above the cutoff frequency, the onset of acoustic shock formation in the upper photosphere, phase-difference contrast between pseudo-mode ridges and the interridge background, enhanced three-minute modulation aureoles around network patches, a persistent low-intensity background pattern largely made up of internal gravity waves, ubiquitous magnetic flashers, and low-lying magnetic canopies with much low-frequency modulation. The spatio-temporal occurrence pattern of internetwork grains is found to be dominated by acoustic and gravity wave interference. We find no sign of the high-frequency sound waves that have been proposed to heat the quiet chromosphere, but such measurement is hampered by non-simultaneous imaging in different passbands. We also find no signature of particular low-frequency flux-tube waves that have been proposed to heat the network. However, internal gravity waves may play a role in their excitation.

## 4.1 Introduction

This paper addresses oscillations of the quiet solar atmosphere from image sequences taken with the *Transition Region and Coronal Explorer* (TRACE). TRACE images the Sun from a Sun-synchronous orbit at characteristic temperatures between  $10^4$  K and  $10^7$  K by sequentially selecting different spectral passbands to feed a  $1024 \times 1024$  px<sup>2</sup> CCD camera with 0.5 arcsec pixels (366 km/px on the Sun) that covers nearly 10% of the solar disk. Details are given by Handy et al. (1999a). First results from the spectacular coronal movies taken through the TRACE far-ultraviolet passbands were presented by Schrijver et al. (1999).

In this paper we use image sequences taken through the ultraviolet TRACE passbands centered at  $\lambda = 1700$ , 1600, and 1550 Å to study quiet-Sun oscillations in the upper photosphere and low chromosphere. We so return to the domain of the pioneering rocket studies of 1600 Å “cell grains” by Brueckner (1980) and Dere & Cook (1983) using the HRTS rocket spectrograph, and by Bonnet et al. (1982), Foing & Bonnet (1984a, 1984b), Foing et al. (1986), and Damé et al. (1986) using the TRC rocket filtergraph. The obvious improvement that TRACE brings over the TRC flights is enormous sequence duration increase and digital data registration per CCD instead of emulsion. TRACE has no spectrograph so that emulation of the HRTS flights requires multi-spacecraft campaigns as in the recent TRACE-plus-SUMER (and MDI) analysis of Judge et al. (2001). The strength of the present analysis is the large statistical significance offered by TRACE image sequences and the use of comprehensive and complementary Fourier diagnostics to provide a complete inventory.

In standard models of the solar atmosphere such as VAL-C of Vernazza, Avrett & Loeser (1973, 1976, 1981) and FAL-C of Fontenla et al. (1993), the disk-center intensity at 1700 Å emerges from the “upper photosphere”, 1550 Å radiation from the “lower chromosphere”, and 1600 Å radiation from the “temperature minimum region”, where the temperature minimum at  $h = 500$  km above continuum optical depth  $\tau_5 = 1$  at  $\lambda = 5000$  Å defines the transition from photosphere to chromosphere (see the formation panels in Fig. 36 of Vernazza et al. 1981). The ubiquitous existence of a chromospheric temperature rise in shell-like (“plane-parallel”) stratification over  $h = 500 - 1000$  km is presently in debate on the basis of the very oscillations discussed here and reviewed below, but we maintain this nomenclature for clarity. Also, we prefer to use “chromospheric dynamics” even for the upper-photosphere diagnostics since the TRACE UV passbands essentially sample the onset of chromospheric oscillations and the chromospheric network.

The same atmospheric regime is accessible to ground-based observation and has been studied extensively using the cores of strong absorption lines and the Ca II K<sub>2V</sub> and H<sub>2V</sub> inner-wing reversals. Although TRACE does not reach the angular resolution of ground-based telescopes at good seeing, TRACE image sequences offer the important advantage of distortion-free sampling over relatively long duration. Compared with oscillation studies employing Fraunhofer line spectrometry in the visible to probe these and lower heights in the solar atmosphere or ultraviolet line spectrometry to probe greater heights, the lack of Dopplershift information is a disadvantage, but TRACE imaging yields data from a far larger area than is sampled by a spectrograph slit and so permits a much more complete view of solar variations as well as much better statistical reliability in their diagnosis. In addition, the wide-band continua sampled by the TRACE 1700 and 1600 Å passbands do not suffer Dopplershift contamination as is the case for the apparent brightness modulation of optically

thick lines (including the inner wings of Ca II H & K, see Sect. 4.4.3). These outstanding TRACE capabilities are exploited here to wrap up much previous work.

The extensive older literature on oscillations in the upper photosphere and lower chromosphere has been reviewed by Rutten & Uitenbroek (1991); more recent work is reviewed by Rutten (1994, 1995, 1999, 2001), Stein & Carlsson (1997), Carlsson & Stein (1998), Carlsson (1999), Deubner (1998), and Deubner & Steffens (1999). Even in quiet-Sun areas strict distinction must be made between network and internetwork. The first term denotes those parts of the supergranular cell boundaries that contain kilogauss magnetic elements at sufficient spatial density to show up on photospheric magnetograms and on chromospheric images taken in the core of Ca II K or the ultraviolet TRACE passbands. On such filtergrams the chromospheric network appears as chains of bright patches, each corresponding to a cluster of thin magnetic elements in the underlying photosphere. The latter, commonly identified with the modeller's fluxtubes, make up the magnetic network and may appear as individual bright grains in high-resolution (better than 0.5 arcsec) movies made in the Fraunhofer G band around  $\lambda = 430.5 \text{ \AA}$  (e.g., Muller et al. 1989; Title & Berger 1996; Berger et al. 1998; movies on the Dutch Open Telescope website<sup>1</sup>).

The bright patches on chromospheric filtergrams map the supergranular cell boundaries too sparsely to make the network identifiable as cellular patterning on snapshot images (cf. Hagenaar et al. 1997), but they stand out in longer-duration image sequences by being generally brighter and much more stably present than the transient, often briefly repetitive and often fast-moving, grainy brightness features seen in the intervening "internetwork" areas corresponding to supergranular cell interiors.

The high degree of co-spatiality of the brightness features seen in Ca II K and the TRACE ultraviolet channels has been demonstrated by Rutten et al. (1999). The correspondence between network grains in Ca II K and clusters of smaller G-band magnetic elements located in underlying intergranular lanes is illustrated in Fig. 2 of Lites et al. (1999). The dynamical behaviour of the Ca II K internetwork brightness patterning is illustrated in Fig. 3 of the same paper. Figure 5 of Rutten et al. (1999b) illustrates similar behaviour in a TRACE 1550 Å image sequence. Figure 4.5 below shows a comparable 1700 Å sequence.

The internetwork "three-minute" oscillations (often in their "internetwork grain" disguise and often called " $K_{2V}$  grains", see Rutten & Uitenbroek 1991) are intensely discussed in the recent literature after their identification as weak acoustic shocks by Carlsson & Stein (1992, 1994, 1995, 1997, 1998). Major issues that are presently in debate are, respectively: (i) – the degree of correlation between internetwork grain occurrence and enhanced internetwork field (Lites et al. 1999 and references therein; Worden et al. 1999), (ii) – the presence of identifiable pistons at or below the surface that cause enhanced acoustic flux higher up in the atmosphere (Hoekzema & Rutten 1998; Hoekzema et al. 1998; Hoekzema & Brandt 2000; Kiefer & Balthasar 1998; Goode et al. 1998; Skartlien 1998; Rast 1999; Skartlien et al. 2000), (iii) – the relation between such pistons and observed velocity–intensity ( $V-I$ ) phase-difference patterns in photospheric ( $k, \omega$ ) diagrams (Straus et al. 1999; Oliviero et al. 1999; Skartlien & Rast 2000) with additional interest concerning  $p$ -mode asymmetries (Nigam & Kosovichev 1999a, 1999b; Georgobiani et al. 2000), (iv) – the amount of wave reflection in the upper chromosphere (Deubner et al. 1992, 1996; Kneer & von Uexküll 1993; von Uexküll

---

<sup>1</sup>URL <http://dot.astro.uu.nl>

& Kneer 1995; Jefferies et al. 1997; Schmitz & Steffens 1999; Carlsson & Stein 1999), (*v*) – the penetration height of the shocks into the higher chromosphere as evidenced by ultraviolet spectrometry with HRTS (Hoekzema et al. 1997) and SUMER (Steffens et al. 1997; Carlsson et al. 1997, 1999; Curdt & Heinzel 1998; Gouttebroze et al. 1999; Doyle et al. 1999; Curdt et al. 1999; Carlsson 1999; Wikstøl et al. 2000; Judge et al. 2001), (*vi*) – the shock contribution to chromospheric heating (Theurer et al. 1997a, 1997b; Kalkofen et al. 1999), (*vii*) – the shock contribution to the basal flux observed from cool stars (Cuntz et al. 1999; cf. Ulmschneider 1999), and (*viii*) – the shock contribution to the FIP split affecting solar wind abundances (Rutten 1997; Judge & Peter 1998). Our TRACE results displayed below bear, directly or indirectly, on all these internetwork debates.

Network oscillations are often invoked to supply chromospheric or coronal heating, but there is no firm identification yet nor have they so far benefited from detailed observation modelling comparable to the Carlsson–Stein internetwork shock simulation. No high-frequency modes have been identified. Well-established (and often rediscovered) dichotomies are that the chromospheric network brightness modulation differs distinctly from the internetwork in showing primarily periodicities of  $P \approx 5$  min and longer, and that these modulations are much clearer in Dopplershift than in brightness (e.g., Jensen & Orrall 1963; Liu & Sheeley 1971; Cram 1978b; Lites et al. 1993). Kneer & Von Uexküll (1985, 1986) have suggested that the observed slow periodicities represent erratic fluxtube footpoint motions whereas Kalkofen (1997, 1999) argues that they are magnetoacoustic modes that are generated impulsively as transverse waves in the photosphere and become longitudinal higher up, and Goodman (2000) proposes that linear fluxtube waves drive transverse charged-particle currents which provide heating by resistive dissipation. An additional network issue is posed by the three-minute “power aureoles” around dense network and plage (Braun et al. 1992; Brown et al. 1992; Toner & Labonte 1993; Hindman & Brown 1998; Braun & Lindsey 1999), and the reversed-sign “power shadows” found by Judge et al. (2001). We address the network issues below as well.

This paper is an initial TRACE study of oscillations in the quiet-Sun temperature-minimum domain. Our goal is to provide a comprehensive inventory and to place that in the context summarised above, combining standard oscillation analysis techniques with a variety of display formats: (*i*) – space-time displays plotting spatial development patterns; (*ii*) – power-map displays plotting Fourier amplitude per spatial element and per temporal frequency bin; (*iii*) – one-dimensional Fourier spectra of oscillatory power, phase difference and phase coherence, with separation of the network and internetwork contributions, and (*iv*) – two-dimensional ( $k_h, f$ ) phase-difference spectra. These displays represent a space-based counterpart to the similar ones from ground-based filtergram sequences in Kneer & von Uexküll (1993). It is worthwhile to combine these different formats in a single paper to enable interpretative comparisons, but the disadvantage is that the interpretation ranges widely, from acoustic to gravity to canopy waves.

We also add pertinent comparison displays of the Ca II H spectrogram sequences that were used by Lites et al. (1993, henceforth Paper I) to describe chromospheric network oscillations in the first paper of this series. The internetwork part of these sequences provided both the photospheric input and the chromospheric testing ground for the numerical simulations of Carlsson & Stein (1997, henceforth CS1997). These data merit a revisit here in order to link our TRACE results to this numerical modelling and to the properties of the same oscillations

when sampled by the Ca II H core and wings.

The organization of the paper is as follows. The observations are presented in the next section. Section 4.3 defines our Fourier methods. In Sect. 4.4 we display TRACE results from May 12, 1998 together with Ca II H comparisons in the various graphical forms listed above. We add an extensive error analysis in Sect. 4.5, including comparison with an independent TRACE data set from October 14, 1998. Some results are discussed in the context of other work in Sect. 4.6. The conclusions follow in Sect. 4.7.

## 4.2 Observations and reduction

**TRACE sequences.** We use two different TRACE data sequences in this paper, from May 12, 1998 and October 14, 1998, respectively. Both were downloaded from the public TRACE archive<sup>2</sup>. Details are given in Table 4.1; background information is available in the TRACE Analysis Guide<sup>3</sup>. During the first run (which was part of Joint Observing Program JOP72 in which most of us participated) TRACE was programmed to observe a rectangular quiet region near disk center sequentially in its three ultraviolet passbands. In the second run, TRACE observed an even quieter rectangular disk-center area with broad-band white light imaging added into the passband sequence. The white light images show (but do not resolve) the solar granulation. They are not used in this paper but may serve for photospheric piston searches in future analyses.

Following the TRACE Analysis Guide we subtracted the readout pedestal of 86 readout units from the images for the 12 May data. We did not apply flat-field corrections or bad-pixel eliminations since none are specified for this date. For the 14 Oct data we used the nominal dark field and the flat field measured on 31 August. The top and bottom pixel rows of the May 12 images are very noisy and were discarded. Only two frames in each data set were affected by telemetry errors; they were replaced by the averages of the preceding and subsequent images. Minor effects from the data compression appear in the data, for example as a low-amplitude interference pattern in spatial frequency in Fig. 4.23.

**Passbands.** Transmission curves for the three ultraviolet passbands are given by Handy et al. (1998) together with a numerical recipe to isolate the contribution of the C IV doublet at  $\lambda = 1548 \text{ \AA}$  and  $1550 \text{ \AA}$  through optimised combination of images taken in the three ultraviolet passbands. The C IV lines dominate the  $1550 \text{ \AA}$  brightness in active areas, but in quiet areas contributions from C I lines, from other lines, and from the continuum dominate in the  $20 \text{ \AA}$  wide  $1550 \text{ \AA}$  passband. We display Fourier results for such C IV “constructs” below in which the combination recipe was applied to the Fourier transforms of the three sequences, after Fourier demodulation to correct for the time delays between the sequentially exposed images.

**Exposure timing.** The TRACE housekeeping data specify the exposure duration and the moment at which the shutter closed for each individual image. The nominal delay between

---

<sup>2</sup>RL <http://vestige.lmsal.com/TRACE/>

<sup>3</sup>URL <http://diapason.lmsal.com/~bentley/guides/tag/>

Table 4.1: TRACE observations used in this paper

date	May 12, 1998	October 14, 1998
program sequence	TDT.trnotsofast	TDT.any_frames
image size [px]	$256 \times 1024$	$512 \times 512$
number of images	354	612
$X_{\text{cen}}, Y_{\text{cen}}$ [arcsec]	$-40, 308$	$-13, -82$
$L_{\text{cen}}, B_{\text{cen}}$ [deg]	$-2.51, 15.98$	$-0.77, 1.04$
duration [UT]	14:30–16:00	08:12–12:00
cadence [s]	15.0573	21.8625
exposure $1700 \text{ \AA}$ [s]	2.0479	2.0480
exposure $1600 \text{ \AA}$ [s]	1.0239	1.0239
exposure $1550 \text{ \AA}$ [s]	5.7919	9.7400
exposure white [s]	—	0.0064

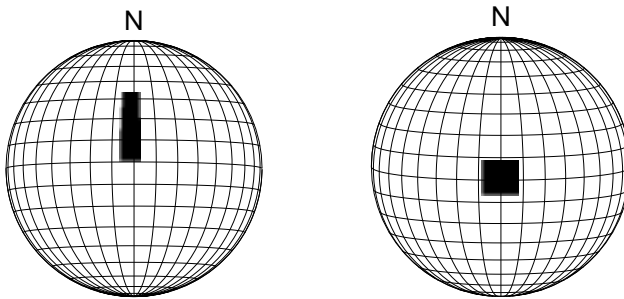


Figure 4.1: Solar location of the fields observed with TRACE on May 12, 1998 (left) and October 14, 1998 (right). The grid shows heliocentric longitude and latitude for each date.

successive images in a given passband was 15 s for May 12 and 21 s for October 14. Occasionally there were 1 s longer intervals on May 12 and up to 10 s longer intervals on Oct 14; the cadence values in Table 4.1 are sequence averages. These erratic increments upset the use of standard Fast Fourier Transform (FFT) routines which assume equidistant spacing. We therefore defined an equidistant time scale for each dataset, combining the average interval with an optimum starting time, and then selected the image closest to each equidistant time step for FFT analysis. For the May 12 data, the offset from the actual mid-exposure time is always shorter than half the exposure duration. The slower cadence and longer  $1550 \text{ \AA}$  exposures of the October 14 data combine into larger offsets. However, worse effects result from the non-simultaneity of the imaging in the different passbands (Sect. 4.6).

**Observed fields.** The  $(X_{\text{cen}}, Y_{\text{cen}})$  values in Table 4.1 specify the location of the center of the field in the TRACE coordinate system measuring distance from apparent disk center in

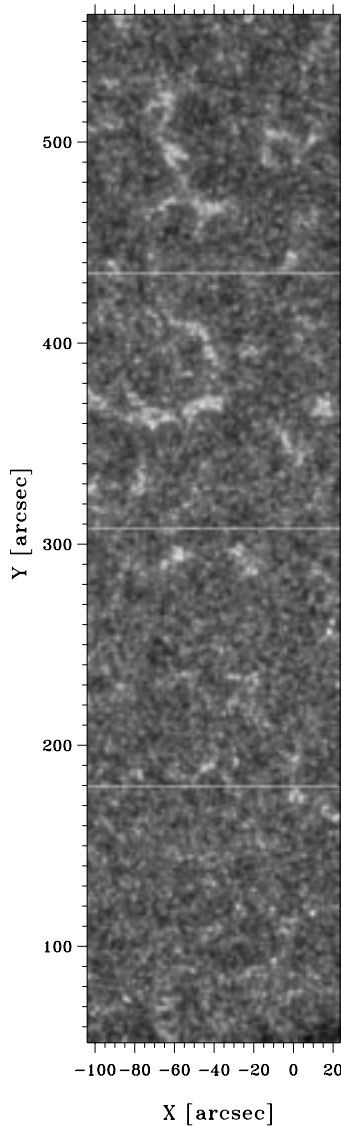


Figure 4.2: Sample image taken by TRACE on May 12, 1998, at 15:26:32 UT in the  $1700 \text{ \AA}$  passband. The upper half contains stronger network. Axes: solar  $X$  and  $Y$  in arcsec from disk center. The greyscale is logarithmic in order to bridge large contrast. The field was split into the four indicated subfields for this analysis.

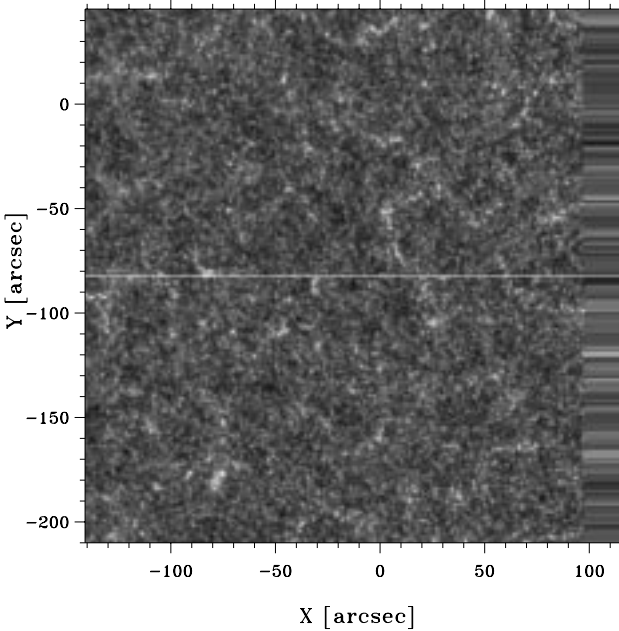


Figure 4.3: Sample image taken by TRACE on Oct 14, 1998, at 10:05 UT in the  $1700 \text{ \AA}$  passband. The observed area was very quiet. Axes:  $X$  and  $Y$  in arcsec from disk center, same scale (on the paper) as in Fig. 4.2. Greyscale: logarithmic. The field was split into two subfields as indicated. The horizontal striping at right marks incomplete sampling which results from solar rotation correction.

arcsec on the sky along the solar meridian (north positive) and latitude circle (west positive) through disk center. The  $(L_{\text{cen}}, B_{\text{cen}})$  coordinates specify the corresponding heliographic longitude and latitude of the field center midway the sequences. Figure 4.1 shows the field orientations. Figures 4.2 and 4.3 show sample  $1700 \text{ \AA}$  images from the May 12 and October 14 sequences, respectively. The intensity scaling is logarithmic in order to accommodate both network and internetwork variations; this is the case for all greyscale image displays in this paper. The May 12 field contained some active network. The October 14 field sampled an area that was very quiet. Both fields were divided into smaller subfields to fit our computer memory during the analysis.

Solar rotation causes a drift of the entire field during the observation period while differential rotation causes differential drifts within the field. The split of the May 12 field into four subfields and of the October 14 field into two subfields, each covering  $256 \text{ px}$  in  $Y$ , reduces the differential variation. Each subfield was “derotated” by co-alignment through cross-correlation. This was done for the four May 12 subfield sequences by aligning each frame to the average of 10 mid-sequence frames. Direct comparison between different wave-

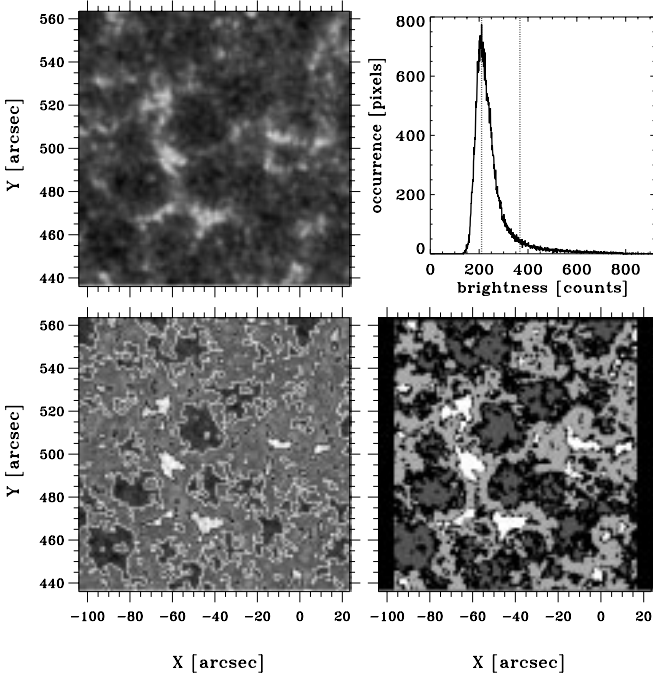


Figure 4.4: Network and internetwork masks for the top subfield of the May 12 data shown in Fig. 4.2. Upper left: 30-min average (15:00–15:30 UT) for  $1600 \text{ \AA}$ , logarithmic greyscale,  $X$  and  $Y$  axes in arcsec from disk center. Upper right: histogram of the number of pixels per brightness bin in this average. Dotted lines: division into internetwork (left), intermediate (middle strip), and network (right) categories. Lower left: logarithmic average overlaid with white and black contours corresponding to the demarcations. Lower right: final mask resulting from three successive 30-min averages. Dark grey: internetwork. White: network. Light grey: intermediate category in all three averages. Black: pixels which switch category between averages, discarded. The left and right edges are sampled incompletely due to solar rotation tracking and are also discarded.

lengths was made possible by co-aligning each subfield sequence to the corresponding  $1600 \text{ \AA}$  one.

The longer duration of the October 14 subfield sequences (nearly four hours) and the consequent evolution of the solar scene necessitated a more elaborate three-step alignment procedure. It consisted of first aligning each sequence of 20 images to the last previously aligned image, then replacing image shifts above three-sigma rms value by the average shift of the preceding and subsequent images in order to reduce pointing jitter extremes, and finally co-aligning all images per sequence to the  $1600 \text{ \AA}$  sequence. The resulting October 14 alignments are generally accurate to a few tenths of a pixel. The May 12 alignments show larger displacements and were smoothed through  $3 \times 3$  pixel spatial boxcar averaging.

These alignments make fixed-pixel locations  $(X, Y)$  in each  $(X, Y, t)$  sequence corre-

spond to fixed solar locations with respect to the local co-rotating solar frame. The rotation produces incomplete solar sampling at the east and west field edges where pixels rotated in or out of the field during the sequence. These are excluded from the measurements below by using edge masks as illustrated in Fig. 4.4.

**Network/internetwork separation.** Each observed subfield was divided into network, internetwork, and remaining area called “intermediate”. The latter may (and indeed does) mix properties of the two regimes and was introduced at appreciable fill factor in order to achieve better isolation of characteristic properties of the network and internetwork, respectively.

The separation was defined in terms of the average 1600 Å brightness per pixel over periods of 30 min for May 12, 80 min for October 14. The more stably present network patches survive such averaging, whereas the faster varying internetwork emission is washed out (compare the sequential variations in Fig. 4.5 with the 30-min average in the first panel of Fig. 4.4 and with the 90-min average in the first panel of Fig. 4.14). The upper-right panel of Fig. 4.4 shows a sample 30-min brightness distribution in the form of a histogram. It is characteristic for all our data and shows a Gaussian peak with an extended tail towards large brightness. Network/internetwork masks were constructed from the three successive 1600 Å histograms per subfield by assigning a pixel to be “internetwork” if its average brightness was below the Gaussian peak location in all three histograms, to be “network” if it belonged in all three histograms to the non-Gaussian high-intensity tail demarcated in Fig. 4.4, and to be “intermediate” if it fell between these extremes in all three histograms. Pixels that changed category between the three histograms were excluded. The mask that resulted for the May 12 top subfield is shown at lower right in Fig. 4.4. It restricts the pixels labeled network to the brightest areas in the first panel of Fig. 4.14 and the internetwork to rather small “heartland” regions relatively far from network, with a large zone of intermediate-category pixels (light grey) separating the two.

### 4.3 Fourier analysis

We briefly review our evaluations of Fourier quantities from the TRACE data. The analysis is standard following Edmonds & Webb (1972), Paper I, and Lites et al. (1998), but there are various display choices that require discussion. We write the temporal Fourier transform of a time sequence  $f_1(x, y, t)$  for solar location  $(x, y)$  as

$$F_1(x, y, f) = a_1(x, y, f) + i b_1(x, y, f) \quad (4.1)$$

where  $a_1$  and  $b_1$  are real numbers,  $t$  represents time and  $f$  temporal frequency. The subscript 1 indicates a particular TRACE sequence. The cross-correlation spectrum between two simultaneous sequences 1 and 2 per location  $(x, y)$  is

$$\begin{aligned} F_{12}(x, y, f) &= F_1(x, y, f) F_2^*(x, y, f) \\ &= c_{12}(x, y, f) + i d_{12}(x, y, f) \end{aligned} \quad (4.2)$$

where the asterisk indicates the complex conjugate and  $c_{12}$  and  $d_{12}$  are real numbers.

**Power normalisation.** Standard choices for the display of power spectra are to plot the modulation energy

$$P_E(x, y, f) = a(x, y, f)^2 + b(x, y, f)^2, \quad (4.3)$$

the fractional modulation

$$P_f(x, y, f) = \frac{a(x, y, f)^2 + b(x, y, f)^2}{a(x, y, 0)^2 + b(x, y, 0)^2}, \quad (4.4)$$

or to use Leahy normalisation

$$P_L(x, y, f) = \frac{a(x, y, f)^2 + b(x, y, f)^2}{\sqrt{a(x, y, 0)^2 + b(x, y, 0)^2}} \quad (4.5)$$

(Leahy et al. 1983, cf. van der Klis 1989, appendix of Doyle et al. 1999). The latter serves to estimate the significance of periodic signals but is not used here.

This choice in normalisation does not affect the relative shape of an individual power spectrum but becomes important when comparing or averaging different signals. For example, if some wave process dissipates the same amount of energy at the wave frequency both in network and internetwork locations, using (4.3) without normalisation is appropriate. Fractional power normalisation (4.4) would underestimate the network dissipation in that case because network is consistently brighter, but it becomes the right measure when both network and internetwork are affected by the same multiplicative modulation process. We illustrate such differences below.

**Phase differences.** The phase-difference spectrum is

$$\Delta\phi(x, y, f) = \arctan\left(\frac{d_{12}(x, y, f)}{c_{12}(x, y, f)}\right) \quad (4.6)$$

where positive values of  $\Delta\phi$  imply that signal 1 is retarded with respect to signal 2. Different strategies exist to display and average phase differences  $\Delta\phi$ . The simplest one is to simply display all samples per temporal frequency in an unweighted scatter diagram (e.g., Gouttebroze et al. 1999), neglecting the amplitudes of the contributing Fourier components, or to display the scatter point density as brightness (e.g., Kneer & von Uexküll 1993). Another extreme is to display only spatial averages per frequency through averaging over a spatial wavenumber  $k_h$  segment or an annulus in the  $(k_x, k_y)$  spatial transform plane (e.g., Deubner et al. 1992). We prefer, as in older work, to visualise also the scatter itself in order to permit appreciation of its distribution. Lites & Chipman (1979) applied weighting per  $(x, y, f)$  sample by the cross-power amplitude  $\sqrt{P_1 P_2}$  (with  $P_1 = a_1^2 + b_1^2$  and  $P_2 = a_2^2 + b_2^2$ ) to produce binned greyscale  $\Delta\phi$  displays with normalisation per temporal frequency bin. In Paper I only the samples with the highest mean Fourier amplitude  $(\sqrt{P_1} + \sqrt{P_2})/2$  were plotted as scatter diagrams. In this paper we show binned greyscale scatter plots with cross-power amplitude sample weighting following Lites & Chipman (1979).

We overlay spatially-averaged phase difference curves following Lites et al. (1998), given per sampled frequency by

$$[\Delta\phi]_{xy}(f) = \arctan\left(\frac{[d_{12}(x, y, f)]_{xy}}{[c_{12}(x, y, f)]_{xy}}\right) \quad (4.7)$$

where the square brackets express averaging over locations  $(x, y)$ . This procedure equals vector addition of the individual cross-correlation samples with each vector length set by the product of the two Fourier amplitudes so that the cross-power amplitudes again act as weights in setting the slope of the summed vector. The procedure avoids wraparound errors that occur in straightforward averaging from the arctan evaluation, for example when a value just above  $\pi$  is transformed into one just above  $-\pi$  and then averages erroneously with one just below  $\pi$  to  $\Delta\phi \approx 0$  instead of  $\Delta\phi \approx \pi$ .

**Coherence.** There is also a choice for the evaluation of the degree of coherence between two signals. It requires some sort of local temporal or spatial averaging, because without any smoothing the coherence between two sinusoidal Fourier components at given  $(x, y, f)$  is unity regardless of the corresponding Fourier amplitudes and phase difference. The Würzburg practice of annular  $k_h$  averaging has the advantage that adjacent frequencies are treated independently, but the disadvantage that the modulations are assumed isotropic. Note that in this case the mean coherence goes to zero for pure noise. In contrast, Lites and coworkers treat each spatial pixel as an independent sample of solar behaviour but average over a frequency interval (Paper I<sup>4</sup>, Lites et al. 1998), a tactic necessarily followed also in the one-dimensional phase modelling of Skartlien et al. (1994). For pure noise this procedure yields positive coherence  $C = 1/\sqrt{n}$  when averaging a sufficiently large sample, with  $n$  the number of frequency resolution elements per averaging interval. We use the latter method, selecting boxcar frequency smoothing that is represented by angle brackets in writing the coherence as

$$C^2(x, y, f) \equiv \frac{\langle F_{12} \rangle \langle F_{12}^* \rangle}{\langle F_1^2 \rangle \langle F_2^2 \rangle} \quad (4.8)$$

$$= \frac{\langle c_{12} \rangle^2 + \langle d_{12} \rangle^2}{\langle a_1^2 + b_1^2 \rangle \langle a_2^2 + b_2^2 \rangle}. \quad (4.9)$$

The spatially averaged coherence per frequency is then:

$$[C^2]_{xy}(f) = \frac{[\langle c_{12} \rangle^2]_{xy} + [\langle d_{12} \rangle^2]_{xy}}{[\langle a_1^2 + b_1^2 \rangle \langle a_2^2 + b_2^2 \rangle]_{xy}}. \quad (4.10)$$

**Fourier reduction.** We determined and Fourier-transformed the temporal brightness variation per pixel using equidistant time sampling with closest-neighbour image selection as discussed above, 10% cosine bell windowing, and replacing the zero-frequency transform values by the original mean brightness. We applied frequency smoothing for the coherence evaluations with  $n = 5$  so that pure noise has  $C = 0.45$ . The phase differences between different TRACE passbands were corrected for the temporal shifts between their respective sampling scales. The shifts result from the sequential TRACE image taking and produce artificial phase shifts that increase linearly with frequency when measured as phase-difference angle. Other effects from the sequential sampling are discussed in Sect. 4.6.

The resulting Fourier power spectra, phase-difference spectra and coherence spectra per solar location were spatially averaged over the network and internetwork pixel categories,

---

<sup>4</sup>The angle brackets and squares in Eq. (4) of Paper I are in the wrong order (but not in the actual code used there).

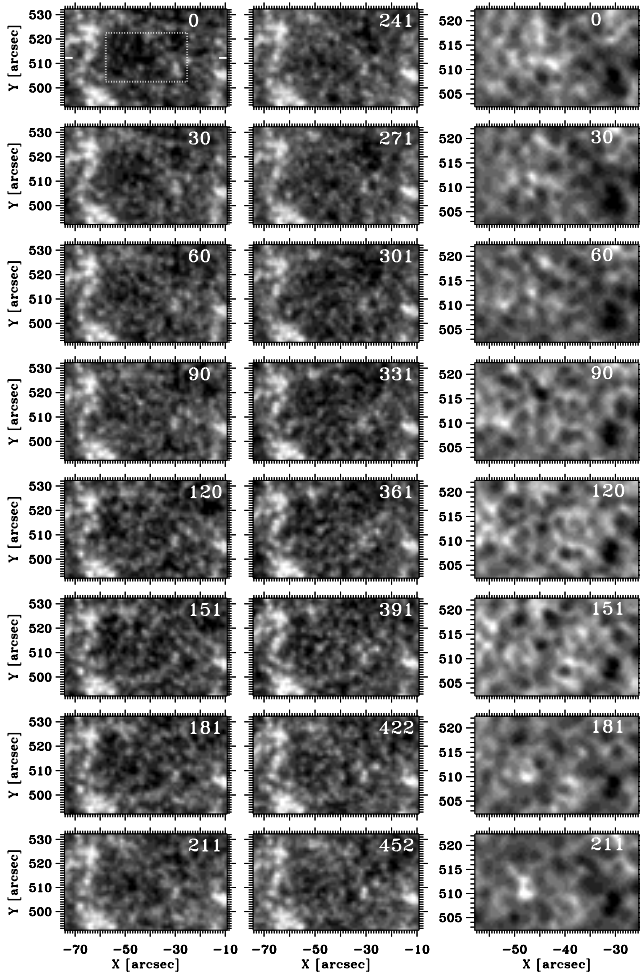


Figure 4.5: Partial cutouts from the May 12 1700 Å sequence illustrating temporal variations at 30 s cadence. The numbers specify elapsed time from 15:26:32 UT in seconds. Axes:  $X$  and  $Y$  in arcsec from disk center. The greyscale is logarithmic. The first panel is a central cutout of the top panel in Fig. 4.2. The white markers along the sides of this panel specify the horizontal cut location used in Figs. 4.6–4.7. The white box marks the yet smaller subfield which is duplicated in the third column using a sign-reversed logarithmic greyscale to display the slowly-varying internetwork background pattern. Taking the inverse emphasizes the internetwork features by darkening the network and makes the brightness minima of the three-minute oscillation appear as brightest features. These reversed extrema appear to travel fast along the strands of a more persistent background mesh which we attribute to gravity-wave interference. Similar behaviour is seen, in counterphase, for the bright internetwork grains on non-inverted but rapidly displayed movies such as the ones on URL <http://www.astro.uu.nl/~rutten/trace1> from which this figure is derived. The grain-to-mesh superposition is also visualized in Fig. 4.11.

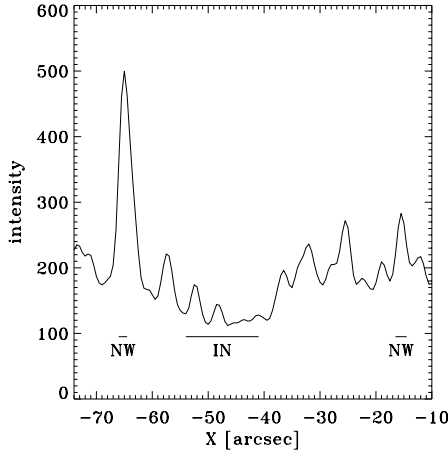


Figure 4.6: Linear intensity variation along  $Y = 512.5$  arcsec in the first panel of Fig. 4.5. The same cut location is used for the  $X-t$  slices in Fig. 4.7. The short bars specify the small segments selected as network and internetwork by the mask in Fig. 4.4.

respectively. We do not show results for the intermediate pixel category when these are indeed intermediate between network and internetwork.

## 4.4 Results

### 4.4.1 Spatio-temporal behaviour

**Sample images and timeslices.** Figure 4.5 illustrates the dynamical nature of the solar atmosphere sampled by the  $1700 \text{ \AA}$  passband in the form of a short sequence of small cutouts from the May 12 top subfield shown in Fig. 4.2. The cutout contains network at left and right, and internetwork in the center. The greyscale is logarithmic to show the grainy nature of both network and internetwork in these displays, which resemble  $\text{Ca II K}$  line-center filtergrams. Each of the network grains results probably from multiple close-lying magnetic elements in the photosphere (we tried but did not succeed to obtain simultaneous G-band imaging with the Swedish Vacuum Solar Telescope to resolve the chromospheric network into photospheric magnetic element clusters). The internetwork area contains bright grains that appear only briefly, for example at  $x = -45$ ,  $y = 516$  in the  $\Delta t = 90$  panel. The network grains vary also with time, but are generally more stable.

The third column in Fig. 4.5 shows further enlargements of the cutouts in the first column with sign-reversed logarithmic greyscaling. The flip in contrast emphasises the spiderweb background pattern to which we return below.

Figure 4.6 shows actual linear intensity along the cut defined by markers in the first panel of Fig. 4.5. The high peak at  $X = -65$  and the peak at  $Y = -25$  are network grains; the

others are internetwork grains with the one at  $X = -33$  a “persistent flasher” (see below). The bright grains ride as enhancements on a general background, as shown already by Foing & Bonnet (1984a). The severity with which the mask defines network and internetwork is illustrated by the shortness of the corresponding cut segments, with only the darkest background classified as internetwork. The flasher is located in the generally brighter intermediate zone.

The traditional way of displaying spatio-temporal variability is to construct space-time plots or “timeslices”. Figure 4.7 shows examples in the form of  $X-t$  graphs that cover the full May 12 sequence temporally but only the  $Y = 512.5$  cut marked in the first panel of Fig. 4.5 spatially. The sequence in Fig. 4.5 samples only the brief duration between the white markers in Fig. 4.7. The  $X-t$  slices in Fig. 4.7 resemble spectrometer data taken with the slit programmed to follow solar rotation (the format is directly comparable to many time evolution displays in the SUMER papers listed in the introduction). They typically show network as bright striping and internetwork oscillations (when present) as dappled grain sequences at lower brightness. Square-root or logarithmic greyscaling or subtraction of the mean intensity per pixel is usually required to enhance the visibility of the internetwork brightness modulation. Figure 4.7 illustrates this morphology with a bright network grain at left, some weaker network grains at right, and internetwork oscillations in the dark area around  $X = -50$ . The oscillatory internetwork patterning is roughly equal in the three TRACE passbands, but the network features become brighter and coarser at shorter wavelength. Additional emission contributed by the C IV lines shows up in the 1550 Å panel and dominates in the C IV construct. The internetwork parts of the latter are very noisy.

A general comment with respect to Figs. 4.5 and 4.7 is that such cutouts and slices constitute a poor proxy for viewing the data cubes in fast on-screen computer display. We use an IDL “cube slicer” developed by C.A. Balke to view concurrent  $(X, Y, t_0)$ ,  $(X, Y_0, t)$  and  $(X_0, Y, t)$  plane cuts through multiple data cubes simultaneously, with mouse control to select and move the  $X_0$ ,  $Y_0$  and  $t_0$  cut location with co-moving cross-hairs in each, up to nine co-changing movie and timeslice panels in total. It enables inspection of such data sets using visual pattern recognition of variations, correlations, time-delay relationships, etc. Such slicing through TRACE data cubes makes one appreciate fully the richness and the variety of the solar scene – effectively sampling a manifold instead of the single cut plotted in a timeslice or observed by a spectrograph slit, and with displacements of one arcsec already showing significant pattern difference. The next-best option is to play TRACE sequences as movies, for example with SolarSoft Xstepper (URL <http://www.lmsal.com/solarsoft/>) or the ANA browser (URL <http://ana.lmsal.com/>). We urge the reader to do so in order to appreciate the dynamical nature of the quiet-Sun internetwork, and have made sample TRACE movies from this work available at URL <http://www.astro.uu.nl/~rutten/trace1>.

What do we see in our TRACE datacube visualizations? Just as on Ca II  $K_{2V}$  movies from ground-based telescopes, the network grains appear as islands of stability in an internetwork sea made up of fast-changing grainy emission features that are superposed on a spiderweb background mesh which is modulated with three-minute periodicity but evolves much slower. The internetwork background is best seen in negative, as in the third column of Fig. 4.5, because its mesh structure then stands out without visual contamination from the brighter network and internetwork grains. It then resembles reversed granulation with 2–5 arcsec cell size, but it cannot be just that since it shows large three-minute modulation. It was detected by

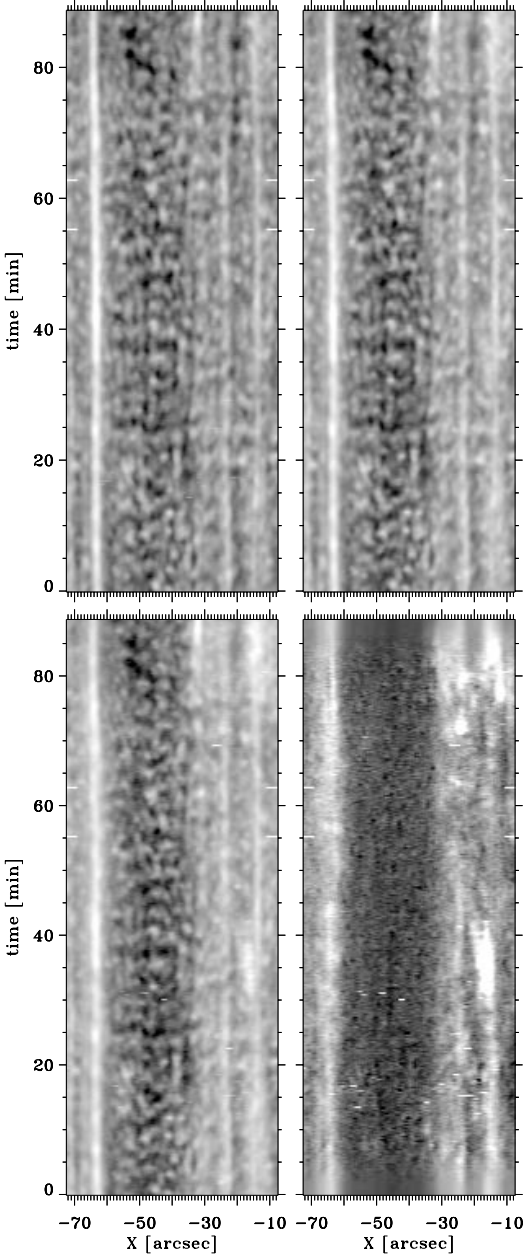


**Figure 4.7.** Partial  $X-t$  slices from the May 12 sequence at  $Y = 512.5$  arcsec, illustrating temporal behaviour of network patches (bright stripes) and internetwork oscillations (grains on dark background). Axes:  $X$  in arcsec from disk center, elapsed time in minutes covering the full sequence duration. Panels: upper left 1700 Å, upper right 1600 Å, lower left 1550 Å, lower right C IV construct. The snapshots in Fig. 4.5 sample the 7.5 min period between the white markers. Greyscale: logarithmic, clipped for C IV. Bright horizontal dashes result from cosmic ray hits.

Martić & Damé (1989) as a 8 Mm spatial power peak in a 4.5 min sequence of TRC 1560 Å filtergrams that was Fourier-filtered passing three-minute modulations; the reverse display in Fig. 4.5 shows it directly without Fourier tuning. The pattern becomes fuzzier with height: the 1700 Å sequences show it sharper than the 1550 Å sequences.

The internetwork grains appear as localised enhancements of the background mesh pattern. They are not as sharp and bright as on  $K_{2V}$  filtergrams but show similar rapid morphology changes on a 2–4 min time basis. Sometimes, they reappear a few times at locations within soundspeed ( $7 \text{ km s}^{-1}$ ) travel distance. Fairly frequently, pairs of grains 5–10 arcsec apart brighten repeatedly in phase. Other grains appear only once. Many brightenings move with apparent supersonic speeds, up to  $100 \text{ km s}^{-1}$ , along the strands of the background mesh pattern. Such travel is more obvious for the darkest locations seen as bright in reversed-greyscale display, peaking when such traveling enhancements “collide” at mesh strand junctions. Occasionally, the timeslices exhibit wavy patterns that indicate oscillatory coherence over spatial scales as long as 20 arcsec. The reversed-greyscale movies also display slower modulation in which the mesh junctions brighten (darken in reality) together in patches covering about 10–20 arcsec. Such large-area coherence was noted already by Cook et al. (1983).

**Comparison with Ca II H & K.** It is of interest to compare the TRACE ultraviolet timeslices in Fig. 4.7 with Ca II H & K results using similar display formats. Most Ca II K filtergram movies are made with passbands between 0.5 and 3 Å, integrating over a fairly wide segment of the Ca II K core and mixing  $K_3$  line-center variations with the  $K_{2V}$  grain and inner-wing whisker phenomena (cf. Rutten & Uitenbroek 1991). This implies both a wider response function including contributions from lower heights as well as phase averaging for upwards propagating waves. The difference in signature can be displayed from spectrogram sequences by integrating over appropriate spectral passbands. Such a comparison is shown between the Ca II  $H_{2V}$  feature and the passband of the Mount Wilson H & K photometer in Fig. 2 of Rutten (1994) and Fig. 1 of Rutten et al. (1999), based on the Ca II H spectrum sequence of Lites et al. (1994) taken in 1991 at the NSO/Sacramento Peak Dunn Solar Telescope. It shows that limiting the bandpass to the  $K_{2V}$  feature itself produces sharper grains with higher contrast than from the integrated Ca II H core, but also that the dynamical time-slice patterning is quite similar for the wider passband.

We add a similar timeslice comparison in Fig. 4.9 that is based on the Ca II H spectrum sequence of Paper I taken with the Dunn telescope in 1984. These data have special interest for internetwork dynamics because they were numerically simulated in great detail by CS1997. Figure 4.8 identifies various spectral features discussed here and below. The first panel of Fig. 4.9 measures the peak brightness of the Ca II  $H_{2V}$  emission feature (following its wavelength shifts), the middle panel integrates brightness over a stable 0.16 Å band around its mean location ( $H_{2V}$  index), and the rightmost panel integrates brightness over a 0.9 Å wide band around mean line center. The noise decreases with bandpass width. The second panel gains grain contrast by sampling low intensity when the  $H_3$  core shifts into the  $H_{2V}$  passband. The third panel shows the internetwork grains at lower contrast and appreciably fuzzier due to response smearing, but nevertheless, the dynamical morphology is similar in all three panels. Thus, wider-band Ca II K movies are indeed suited to study the spatio-temporal patterns of the oscillations that cause  $K_{2V}$  and  $H_{2V}$  grains.

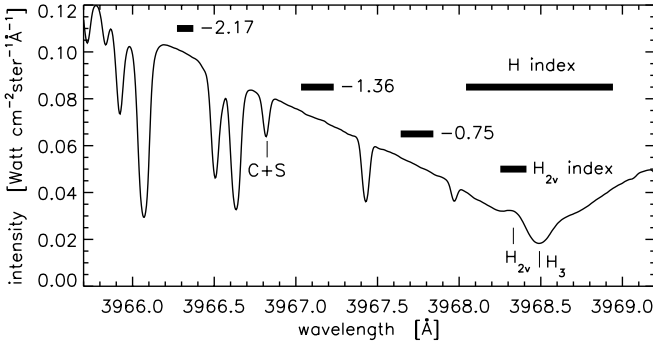


Figure 4.8: Ca II H segment of the disk-center spectrum atlas of Neckel (1999). The horizontal bars mark spectral windows used in Paper I for oscillation measurements shown below. The label C+S identifies the Fe I line used by CS1997 to derive subsurface piston driving in their numerical simulation of the Ca II H line core behaviour in the same data.

CS1997 simulated the four solar locations that are marked in Fig. 4.9 and are labeled with the slit positions specified in their paper. Their simulations reproduced the spectral grain occurrence patterns at positions 110 and 132 remarkably well (their Plate 20). They computed too many and overly bright grains for positions 149 and 30 – which they attributed to a preceding computational excess of high-frequency (14 mHz) oscillations – but nevertheless, the overall agreement between the simulated and observed Ca II H spectral behaviour is impressively good. This success has brought general acceptance of the notion that  $K_{2V}$  internetwork grains are primarily an acoustic weak-shock phenomenon as advocated by Rutten & Uitenbroek (1991a, 1991b).

The ultraviolet slices in Fig. 4.7 are very similar to the wider-band Ca II H slice in the rightmost panel of Fig. 4.9. The TRACE images therefore appear to have adequate angular resolution to display grain patterns similarly to a  $1 \text{ \AA}$  Ca II K filtergram sequence. The considerable spectral width of the TRACE passbands must cause considerable height-of-formation and propagative phase mixing, so that the 1 arcsec TRACE resolution is perhaps not too far from the intrinsic detail observable in these passbands. The direct comparison of a selected Ca II K image with simultaneous TRACE images in Fig. 2 of Rutten et al. (1999) demonstrates that TRACE is not resolving the grains as well as a  $3 \text{ \AA}$  Ca II K filter at excellent La Palma seeing. Note that the ultraviolet continua sampled by TRACE are affected by bound-free scattering which is similar to the bound-bound resonance scattering affecting Ca II K (cf. Fig. 36 of Vernazza et al. 1981; Figs. 2–4 of Carlsson & Stein 1994; lecture notes by Rutten 2000) and produces similar smearing of the source function response to thermal fine structure along the line of sight.

Apart from its lower resolution the  $1700 \text{ \AA}$  image in Fig. 2 of Rutten et al. (1999) is virtually identical to the Ca II K image. The Ca II slices in Fig. 4.9 show several episodes of reduced seeing quality (greyish horizontal wash-outs) that do not occur in the TRACE slices. Thus, the TRACE ultraviolet passbands sample network and internetwork much as

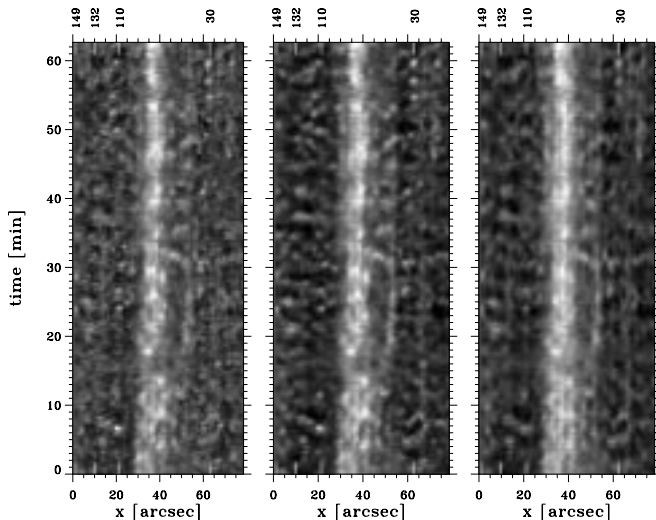


Figure 4.9: Ca II H  $X-t$  slices from the data analysed also in Paper I. Left: Ca II  $H_{2V}$  peak brightness. Middle: Ca II  $H_{2V}$  index = brightness integrated over  $3968.33 \pm 0.08 \text{ \AA}$ . Right: Ca II H index = brightness integrated over  $3968.49 \pm 0.45 \text{ \AA}$ . Bright column markers: solar locations simulated by CS1997, with the “slit positions” specified by them added at the top. A Fourier decomposition of the middle slice is shown in Fig. 4.10.

1–3  $\text{\AA}$  Ca II K passbands do – but they do so seeing-free, without geometrical distortions or temporary degradations.

**Internetwork background.** The grains represent the most striking feature in the internetwork parts of Ca II K and ultraviolet filtergram sequences, but there is also the spiderweb emission pattern that makes up the greyish background in Figs. 4.5–4.7. It is observed most clearly in reversed-greyscale movies as the one at URL <http://www.astro.uu.nl/~rutten/trace1>, here emulated by the third column in Fig. 4.5, has 2–5 arcsec mesh size, is modulated with 2–4 min periodicity, and evolves at longer time scales. Enhancements (both brightenings and darkenings, the latter standing out more clearly in reversed-greyscale display) travel at large apparent speed along the strands (cf. Fig. 3 of Lites et al. 1999). Internetwork grains occur always as local, point-like enhancements of the mesh in its bright phase, as emphasised by Cram & Dame (1983) whose V/R timeslice shows the background as a “wavy curtain” oscillatory pattern with considerable spatial extent (cf. Rutten & Uitenbroek 1991).

Figure 4.10 analyses the internetwork background and grain occurrence with another unpublished display from the 1984 Ca II H data of Paper I. The upper part is a Fourier decomposition of the  $H_{2V}$  index slice in Fig. 4.9 into low-frequency, five-minute and three-minute oscillatory components, similar to the  $H_{2V}$  decompositions of 1991 data in Fig. 4 of Rutten (1994) and Fig. 6 of Rutten (1995). The split is obtained by temporal Fourier filtering per spa-

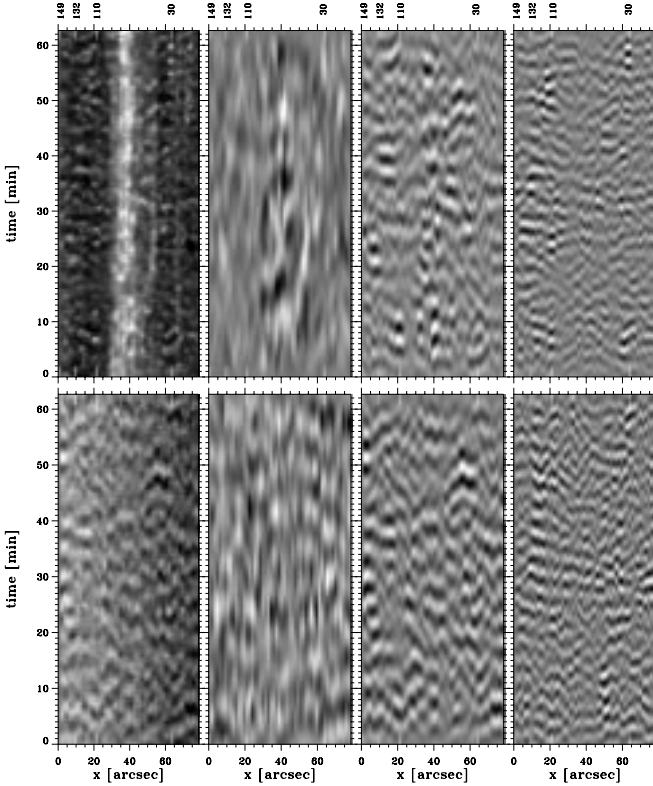


Figure 4.10: Fourier-decomposed timeslices of the spectral data presented in Paper I. Upper panels: Ca II  $H_{2V}$  decomposition. The  $H_{2V}$  brightness slice at left is also shown in Fig. 4.9. The other panels display its decomposition into low-frequency modulation, five-minute modulation and three-minute modulation, obtained by temporal filtering of the sequence for each spatial position along the slit. The greyscale is set to maximum contrast for each panel independently. Lower panels: similar decomposition for the Dopplershift of Fe I 3966.82 Å, the blend from which CS1997 derived a subsurface piston to simulate the intensity in the upper panels at the locations marked along the top.

tial  $x$ -position along the slit, so that adjacent columns are independently decomposed. As in any timeslice, horizontal structures imply instantaneous spatial coherence in the spatial direction while tilted structures suggest motion along the slit (real motion for a round feature, but for an elongated one moving at a small angle the apparent velocity of the slit-feature intersection exceeds the real motion). The lower part of Figure 4.10 decomposes the simultaneously measured Dopplershifts of the photospheric Fe I line from which CS1997 obtained their subsurface piston excursions. The Fe I low-frequency panel (second in bottom row) presumably shows granular overshoot and/or internal gravity waves. The Fe I five-minute and three-minute panels show wavy-curtain patterns with considerable propagative spatial coherence and finer

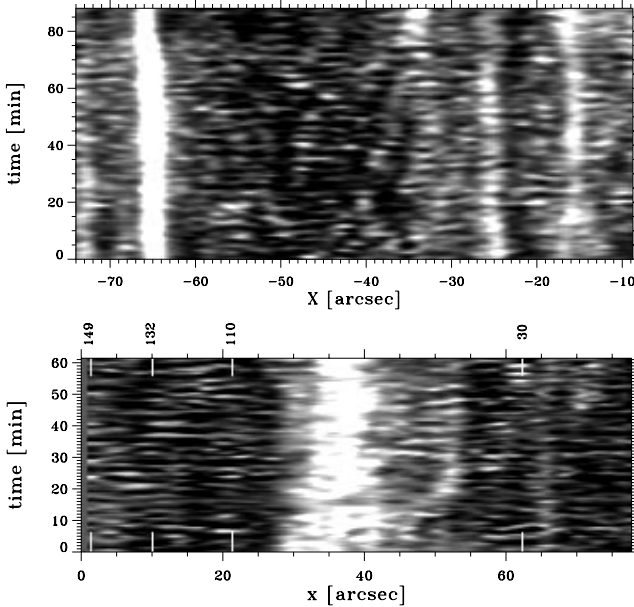


Figure 4.11: Compressed timeslices. Upper panel: the  $1700\text{ \AA}$  data of Fig. 4.7 compressed in the time direction, expanded in the spatial direction, and clipped in greyscale so that the network becomes heavily saturated. Lower panel: similar format for the  $\text{Ca II H}_{2V}$  index data in the middle panel of Fig. 4.9, including Carlsson-Stein markers. The internetwork background mesh shows up as 2–5 arcsec wide columns on which the three-minute oscillation is superimposed.

substructure at shorter periodicity. They extend across the network strip without obvious pattern change. The chromosphere (upper panels) shows qualitatively similar patterns, with appreciable correspondence with the underlying photospheric pattern at least for the five-minute components in internetwork areas. The  $\text{H}_{2V}$  low-frequency panel (second in upper row) is the only modulation panel in which the presence of network (strip at  $x = 30 - 40$  arcsec) is recognisable, having slower and larger-amplitude modulation than the internetwork areas on both sides.

The photospheric wavy-curtain patterns in the third and fourth lower panels represent interference between the ubiquitous acoustic waves of the global and local  $p$ -mode oscillations that dominate the dynamics of the middle photosphere where convective motions have died out. The similar patterns in the upper row indicate that the rapidly varying modulation of the internetwork background mesh in  $\text{Ca II K}$  and ultraviolet filtergram movies is also dominated by acoustic wave interference. However, the background pattern in the low-frequency panels differs morphologically between the upper and lower rows, without obvious direct correspondence.

The internetwork grains in the first panel occur at spatio-temporal locations where the decomposed brightnesses to the right sum up to a bright total. For example, the bright grain at  $t = 7$  min in Carlsson-Stein column 110 marks coincidence of bright five-minute and bright three-minute phases as present in a broad-band impulse. A much weaker grain follows after five minutes because the three-minute modulation is then out of phase. A sequence of bright grains at three-minute periodicity, as the one at the top of Carlsson-Stein column 30, requires the combination of strong three-minute modulation, weak five-minute modulation, and a bright phase of the low-frequency modulation in the second panel. The component weighting follows the  $H_{2V}$  power spectrum which is similar to the  $H_{2V}$  index power spectra shown in Fig. 4.21 and is dominated by the three-minute modulation.

The chromospheric background pattern, its three-minute modulation, and the internetwork grain superposition on this pattern become more evident in timeslices when these are severely compressed in the time direction and clipped as in Fig. 4.11. The internetwork background pattern shows up as dark and bright structures of 20–40 min duration with three-minute modulations that often seem spatially coherent over lengths of 5–10 arcsec, occasionally as long as 20 arcsec – much longer than the coherence extents evident in Figs. 4.7 and 4.9–4.10. This is because the compression reduces the tilts caused by the apparent motion of brightenings and darkenings along the strands of the background pattern, so that the eye interprets the total travel distance as a single coherent feature. A similar pattern seen in Dopplershifts of C II and O VI lines from SUMER was reported by Wikstøl et al. (2000) as a new phenomenon with unexpectedly large spatial coherence, but their timeslice is similarly compressed.

**Persistent flashers.** Some internetwork grains seem to mark a location with longer spatial memory than 5–10 min by reappearing repeatedly, sometimes with extended intervals of absence. An example is seen near  $X = -33$  in the upper half of Fig. 4.7. A bright grain appears in the 1700 Å passband at  $t = 62$  (also in the  $\Delta t = 391$  panel of Fig. 4.5), seems to reappear at  $t = 66$  and  $t = 72$ , and then to become part of a bright streak towards the end of the sequence. In the 1550 Å panel this location has enhanced brightness all the time (at least on our screen). What looks like an isolated 1700 Å grain at first sight is actually part of a long-lived (though modulated) brightness feature.

A particular  $K_{2V}$  grain of this type has been described by Brandt et al. (1992, 1994), who found it by playing a video movie of Ca II K images very fast. It was occasionally absent for some time; fast movie display made its longer persistence recognisable. It flashed at 3–5 min periodicity when seen and it behaved as an actual solar “cork”, the chromospheric emission patch following the surface flows derived from local correlation tracking of granulation features and migrating from cell center to network within a few hours.

Such intermittently present persistent features are not easily identified without movie display. Only when stationary in  $Y$  do they become discernible in an  $X-t$  slice by leaving an extended trail. We find that many isolated bright features which, when seen on a single frame might be taken to represent acoustic shock grains, are in fact such flashers, reappearing over a longer period and often with slightly higher background emission producing a thin trail between flashes in 1550 Å timeslices if the feature doesn’t move “off the slit”. A shift of the slice position over one pixel (0.5 arcsec) often shortens or lengthens the apparent trail considerably. The sample slices in Fig. 4.7 contain a number of such weak long-duration streaks at right.

The weakest ones fall in the intermediate pixel category in our mask definition and are not easily identifiable as network in Fig. 4.5. Only the dark area with dappled grain appearance around  $X = -50$  in Fig. 4.7 seems to represent streak-less internetwork.

This split confirms the present conclusion from a long debate on magnetic internetwork grain anchoring (cf. Lites et al. 1999; Worden et al. 1999) that the internetwork areas may be locally dominated by grain-producing shock acoustics but may also contain features with a longer location memory that presumably mark magnetic field entities of sufficient strength to maintain an identity. We designate the latter “persistent flashers” following Brandt et al. (1992, 1994). The three features marked in Fig. 2 of Lites et al. (1999) represent other examples in the form of isolated chromospheric Ca II K grains that are clearly connected to photospheric G-band bright points of the type commonly believed to represent strong-field fluxtubes.

The flashers seem to appear more frequently near regular network. It is tempting to wonder whether such loose features build up the network or originate from it. The Brandt et al. flasher migrated from cell center towards network as one might expect for a split-apart ephemeral region marking field emergence. Our TRACE movies also show such cell-crossing flashers (plus some brightness features which move very fast along chromospheric mottles or higher-lying loops and stand out as such in the C IV-construct movie, see below), but most flashers appear fairly stationary near network and produce intermittent streaks lasting from half an hour to multiple hours with drifts below 10 arcsec. These may portray products of network shredding rather than network assembly.

By having a large intermediate pixel category we have eliminated most of the persistent non-network features from what our masks define as internetwork, a very stringent selection that should limit the internetwork Fourier results below to the darkest streakless regions in our data, such as the one around  $X = -50$  in Fig. 4.7. Presumably, their brightness modulation is acoustically dominated.

#### 4.4.2 Spatial modulation variations

**Mask-averaged modulation.** Figure 4.12 shows spatially averaged power spectra per mask category for the three ultraviolet wavelengths and the C IV construct. Fourier amplitudes ( $\sqrt{P}$ ) are plotted on linear scales that are scaled per panel (wavelength) to the internetwork value at  $f = 3$  mHz. This represents amplitude scaling analogous to Eq. (4.3). The heights of the different-category curves in each panel are directly comparable. Between panels, they are quantitatively comparable if the evanescent five-minute waves have similar brightness power at different heights in internetwork areas.

The curves in Fig. 4.12 show standard modulation behaviour (but with unprecedented precision) of network and internetwork. The brightness modulation power is highest at the lowest frequencies and reaches secondary maxima in the acoustic oscillation band, which grow in relative importance and in high-frequency extent with sampling height. Note that the acoustic peaks are less pronounced in these brightness modulation spectra than they appear in Dopplershift samples from the same atmospheric domain, largely because Dopplershift modulation lacks prominent low-frequency modulation peaks. The acoustic peak is less clearly defined for the C IV construct.

Network power exceeds internetwork power up to  $f = 5$  mHz but drops faster at higher frequencies. Higher up in the atmosphere, this distinction grows into fully disparate network-

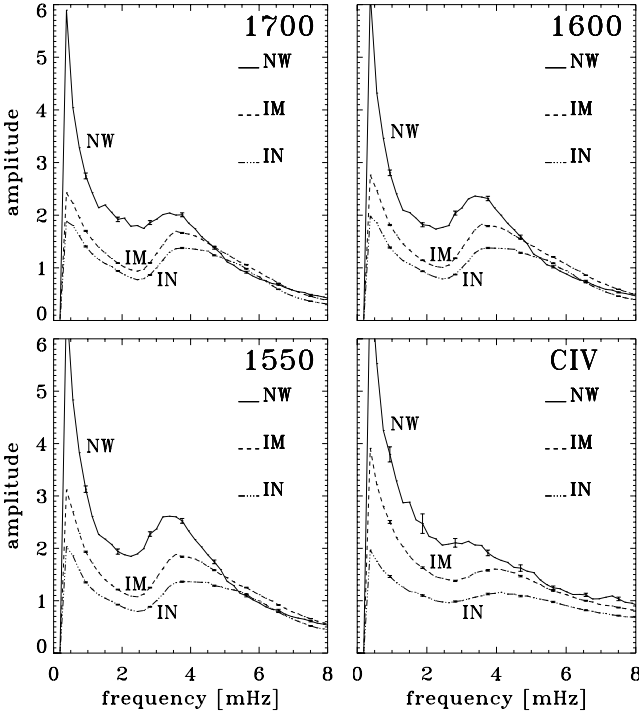


Figure 4.12: Mask-averaged brightness modulation spectra from the May 12 sequences, split between the network (NW), intermediate (IM), and internetwork (IN) pixel categories. Each curve shows linear Fourier amplitude scaled by the internetwork value for that wavelength at  $f = 3$  mHz, against temporal frequency. The mean value and trend (zero and first frequencies) are removed. Error bars: standard error of the average. Upper panels: 1700 and 1600 Å. Lower panels: 1550 Å and the CIV construct.

internetwork modulation behaviour, as illustrated below in Fig. 4.21. Around  $f = 6$  mHz the intermediate-pixel category is no longer intermediate between network and internetwork but has the largest amplitude. We return below to these “power aureoles”.

**Choice of normalisation.** Figure 4.13 duplicates the 1700 and 1550 Å amplitude spectra in the first column of Fig. 4.12, but after normalisation by the mean amplitude, showing fractional modulation analogous to Eq. (4.4). The amplitude scales again have unity at the 3 mHz internetwork value. In the lefthand panel the fractional modulation of network and internetwork appears roughly equal over  $f = 0.5 - 3$  mHz. In the righthand panel the network category is lower than internetwork at all frequencies and the intermediate pixel class shows a “power shadow” for  $f > 4$  mHz.

Comparison with Fig. 4.12 shows that the choice of normalisation affects the network/internetwork modulation ratio. It is not obvious which choice is physically preferable. The

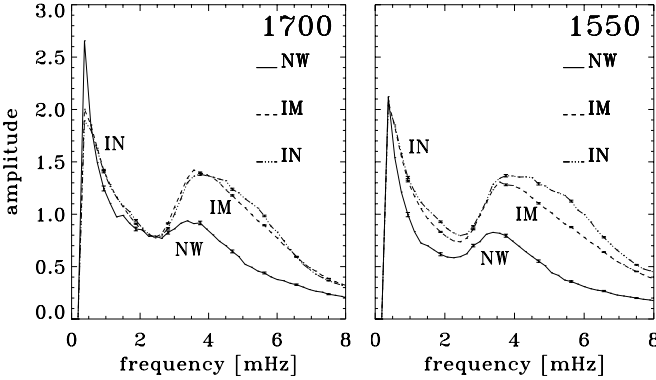


Figure 4.13: Mask-averaged 1700 and 1550 Å fractional brightness modulation spectra, as in Fig. 4.12 but normalised by the temporal mean (zero frequency value, subtracted) per curve.

internetwork 3–6 mHz peak consists of acoustic waves (a mixture of the “photospheric five-minute” and “chromospheric three-minute” oscillations, where none of these names should be taken literally as meaning exclusive). The internetwork low-frequency peak is attributed to internal gravity waves (cf. Sect. 4.4.4). For these wave phenomena absolute power or amplitude specifies the importance of the wave itself, whereas fractional modulation scales the amplitude to the total time-averaged amount of photon emission which may be dominated by other processes. Even if the wave field inside network elements is the same as outside (fractionally or absolutely), the observed modulation does not need to be the same with either normalisation since density differences also affect the sampling height.

**Spatially-resolved modulation.** Figure 4.14 resolves the results in Fig. 4.12 spatially by displaying the brightness modulation per pixel for selected temporal frequency bands, with brighter greyscale indicating larger Fourier amplitude. Cuts along  $Y = 500$  are shown in the top panels and display linear modulation amplitudes normalised by the mean of the whole subfield.

The first column represents the sequence-averaged intensities (zero-frequency modulation). The averaging increases the contrast between the fairly stable network and the rapidly varying internetwork. The logarithmic greyscale permits identification of the darkest internetwork areas; they correspond closely to the internetwork pixel category (dark grey) of the mask in Fig. 4.4. The network grains appear coarser at shorter wavelength in these averages; the C IV construct loses detail. The network contrast increases towards shorter wavelength (cuts on top).

The second and third columns show modulation maps for slow variations, respectively with periodicities  $P > 13$  min and  $P \approx 5$  min. The network appears bright in the greyscale maps, with comparable modulation amplitudes at the different wavelengths (tracings at the top). Both the network and the internetwork areas are finely grained on a 1–2 arcsec scale in these long-duration modulation maps. There is no obvious morphology difference be-

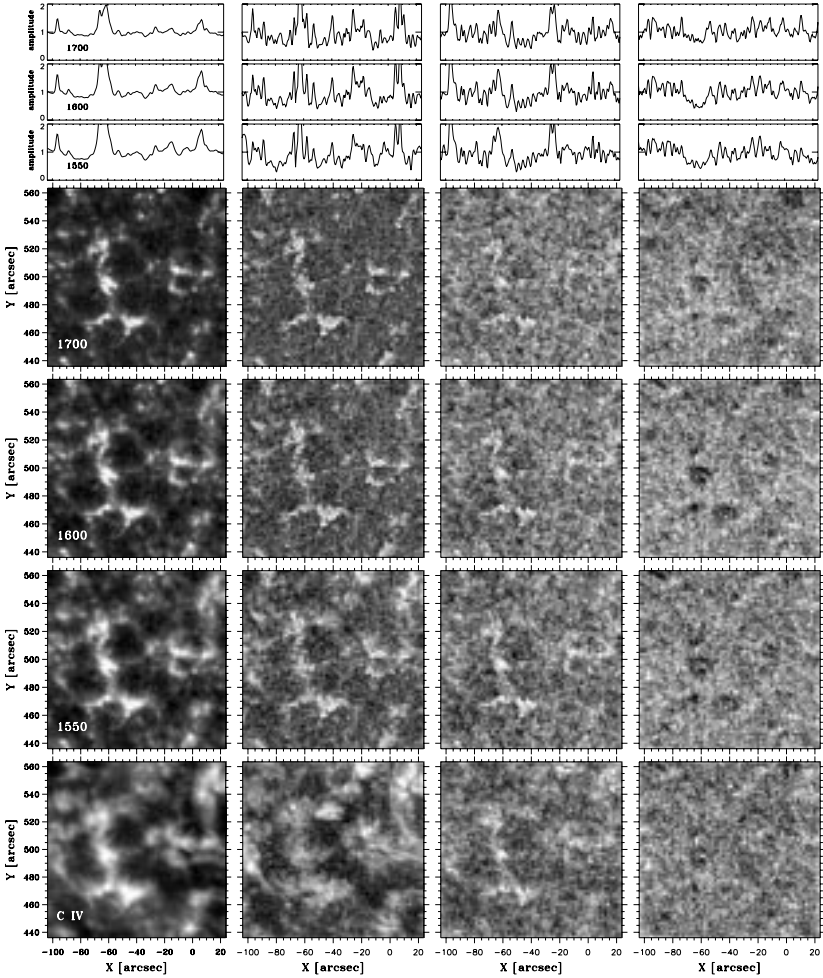


Figure 4.14: Fourier modulation over the top subfield of the May 12 data. Axes: solar  $X$  and  $Y$  at mid-observation in arcsec. Greyscale: logarithm of the temporal Fourier amplitude ( $\sqrt{P}$ ) of the brightness per pixel, clipped and rescaled per panel to improve display contrast. Columns from left to right: average intensity over the full 14:30–16:00 UT sequence duration (also with clipped logarithmic greyscale), Fourier amplitude in the 0.1–1.2 mHz frequency bin, in the 2.6–3.6 mHz bin (periodicity  $P \approx 5$  min) and in the 6–8 mHz bin ( $P \approx 2.5$  min). Graph rows: brightness modulation amplitude along  $Y = 500$  for the 1700, 1600, and 1550 Å passbands, in linear units normalised by the mean modulation over the subfield. Image rows: brightness modulation maps for the 1700, 1600, and 1550 Å passbands and the C IV construct.

tween high and small amplitude regions as in the short-duration modulation amplitude maps of Hoekzema et al. (1998b), probably due to pattern migration during the much longer durations that are Fourier-mapped here.

The normalised modulation amplitudes decrease with frequency (tracings at the top). At all three ultraviolet wavelengths the internetwork modulation gains amplitude with respect to the network modulation and exceeds the latter for frequencies  $f \approx 4$  mHz. The rightmost column illustrates this in the form of dark patches that roughly correspond to the bright network areas in the first column. The high-frequency panel for the C IV construct (bottom right) does not show internetwork contrast reversal, but its internetwork areas are unreliable since these do not contribute C IV signal. The C IV construct images contain many artifacts from cosmic ray hits that have been removed.

**Magnetic canopies.** The C IV low-frequency amplitude map (second from left in the bottom row) differs strikingly from the other amplitude maps. It resembles a H $\alpha$  filtergram by showing the onset of fibrils extending away from the network. There is also a long curved arch in the upper-right corner. When viewing this C IV subfield as a movie, bright blobs are seen to be traveling along the arch at apparent speeds of about  $100 \text{ km s}^{-1}$ . The map also shows bright modulation patches that are much more pronounced than in the longer-wavelength panels, for example around  $(-40, 530)$ . These non-photospheric features indicate substantial contribution by the C IV lines that appears to be visualised easiest through their slow modulation. The fibril-like extensions are barely visible in the C IV  $P \approx 5$  min map.

The C IV fibrils clearly depict magnetic field topology in which the field lines fan out from the network in the form of low-lying bundles. Magnetic canopies are a standard feature of magnetostatic fluxtube modelling (e.g., Spruit 1976; Solanki & Brigljevic 1992; Solanki & Steiner 1990) and were first reported by Giovanelli (1980) and Giovanelli & Jones (1982, 1983) who concluded that the fibrils observed in chromospheric lines such as H $\alpha$  map the actual canopies only partially, showing only those low-lying magnetic loops that have sufficient population density in the H I  $n = 2$  level. We take the bright areas in the low-frequency C IV panel of Fig. 4.14 therefore as an incomplete indicator of canopy presence. The darkest areas in this panel correspond closely to the internetwork part of the mask in Fig. 4.4. This implies that the intermediate pixel category that we derived from the mean 1600 Å brightness behaviour does not only correspond to more frequent occurrence of persistent flashers as discussed above, but also corresponds to the presence of overlying canopy fields that stretch out from the network over the adjacent internetwork at relatively low height.

**Network aureoles.** The amplitude spectra in Fig. 4.12 around  $f = 6$  mHz and the rightmost column in Fig. 4.14 indicates the presence of weak “halos” or “aureoles” of enhanced high-frequency power around the network patches. They are seen as extended, though very patchy, bright rings around the dark areas marking network power deficits. They roughly cover the intermediate pixel zones and make the corresponding IM curves in the 1600 Å and 1550 Å panels of Fig. 4.12 exceed the other curves around  $f = 6$  mHz.

Power aureoles at 3-min periodicity around plage were first reported from a chromospheric Ca II K image sequence by Braun et al. (1992) and from photospheric Dopplershift modulation maps by Brown et al. (1992) as patchy areas that contain small-scale 3-min mod-

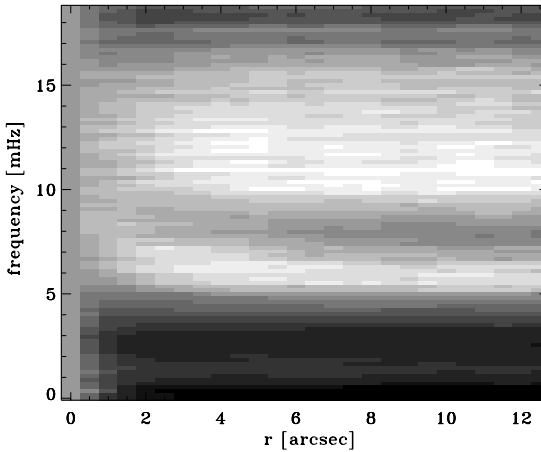


Figure 4.15: Frequency-resolved aureole map, showing temporal power (grey scale) for the May 12 1600 Å data as a function of distance  $r$  to the nearest network border, averaged over all non-network pixels in the whole May 12 field excluding edge pixels and normalised to the mean network power (value at  $r = 0$ , grey) per frequency bin.

ulation enhancements and are associated, but not cospatial, with magnetic regions. They were also seen in Ca II K image sequences by Toner & Labonte (1993), in MDI Dopplergram sequences by Hindman & Brown (1998), and in local-helioseismic images constructed from MDI Dopplershift data by Braun & Lindsey (1999) who renamed them “acoustic glories” and suggested that the aureoles result from subsurface oscillation deficits underneath active regions as a result of wave refraction or scattering. Thomas & Stanchfield (2000) studied them in both the photosphere using a Doppler-sensitive iron line and the chromosphere using Ca II K, finding that the photospheric aureoles favour pixels of intermediate field strength but are not clearly related to the Ca II K aureoles. Hindman & Brown (1998) did not find aureoles in photospheric continuum intensity fluctuations in MDI data and use that to advocate that the halo oscillations are incompressible, a suggestion extended by Thomas & Stanchfield (2000) to the height of formation of their Fe I line .

The network patches in our quiet fields of observation represent much smaller field concentrations than the active regions in the aureole literature above and our TRACE data do not sample Dopplershift, which displays 3–min modulation much clearer than brightness at chromospheric heights (e.g., Cram 1978b), but nevertheless the TRACE images bring additional information because they sample intrinsic brightness modulation in the upper photosphere that result from temperature and/or opacity variations without crosstalk from Dopplershifts.

Figures 4.15–4.16 attempt to quantify the visual impression of aureoles in Fig. 4.14 by plotting 1600 Å Fourier power as a function of the distance of a pixel to the nearest network area with spatial averaging over the whole May 12 data set. Figure 4.15 is a frequency-resolved greyscale plot of this mean dependence for all pixels outside network. The average presence of aureoles shows up as a power peak (bright) between  $r = 3 - 7$  arcsec and  $f =$

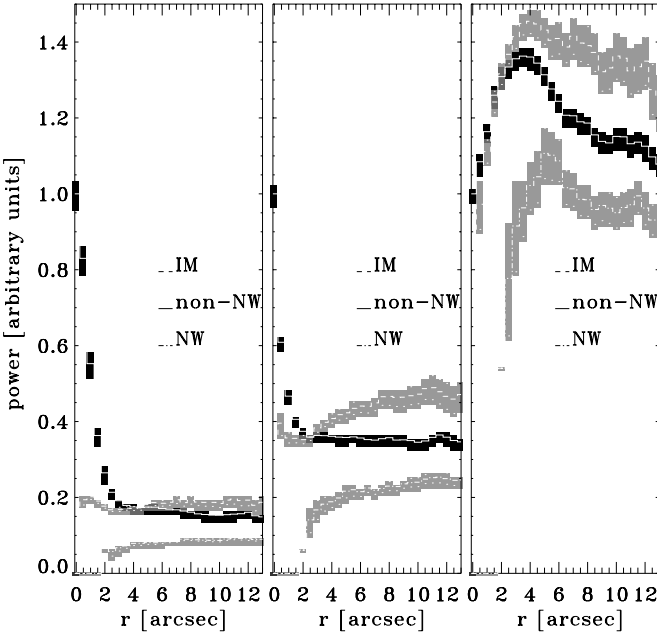


Figure 4.16: Spatially-averaged modulation aureoles for different pixel categories. Each curve measures the mean temporal modulation power of the May 12 1600 Å data as a function of distance  $r$  to the nearest network border, excluding edge pixels and normalised to the mean network power (the value at  $r = 0$ ) per frequency bin. The shaded contours specify  $3\sigma$  error estimates for each mean. Curves with dark contours: averaged over all non-network pixels in the whole May 12 field. Lower curves with grey contours: averaged only over all internetwork pixels. Upper curves with grey contours: averaged only over all intermediate-category pixels (light grey in Fig. 4.4). Panels from left to right: 0.1–1.2 mHz frequency bin, 2.6–3.6 mHz bin (periodicity  $P \approx 5$  min) and 6–8 mHz bin ( $P \approx 2.5$  min). At right, all three curves peak near  $r \approx 4$  arcsec.

5 – 7 mHz.

Figure 4.16 displays the same power-versus-distance measurements for selected frequencies with spatial division between internetwork pixels, intermediate-category pixels, and their sum (“non-network”) according to the mask definition in Figs. 4.4. The first panel illustrates that at low frequencies network power generally exceeds non-network power. The five-minute power distributions in the middle panel show a remarkable split between the intermediate and true internetwork pixels. Both categories display an initial dip followed by a rise of mean power with distance from the nearest network. The intermediate category does so at a much higher value.

The 6–8 mHz panel at right shows similar but steeper initial increases for all three pixel categories, peaks at  $r = 3$ –5 arcsec, and average decreases further out. The intermediate-category pixels provide the largest contribution to this pattern, also at large distance  $r$ . Thus,

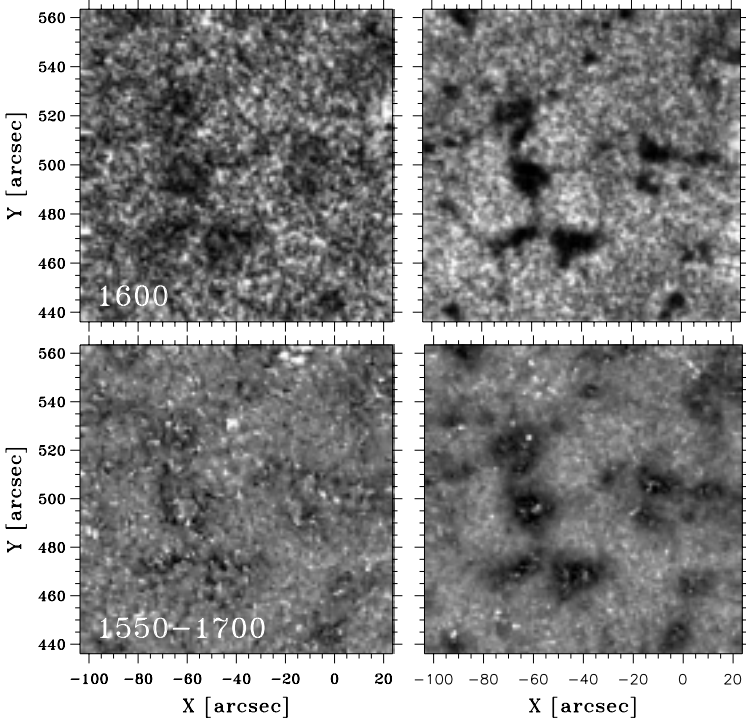


Figure 4.17: Network shadows in normalised amplitude maps. Upper row: Fourier modulation maps for the top subfield of the 1600 Å May 12 data, similar to the third and fourth panels in the second row of Fig. 4.14 but with the greyscale representing linear Fourier amplitude per pixel normalised by the temporal mean per pixel. Lower row: ratio of 1550 and 1700 Å normalised amplitude maps. Left column: 2.6–3.6 mHz bin (periodicity  $P \approx 5$  min). Right column: 6–8 mHz bin ( $P \approx 2.5$  min).

the high-frequency aureoles seem to favour the relatively large time-averaged brightness that make up the intermediate-category pixels – possibly marking the presence of persistent flashers, or the presence of overlying canopy fibrils as evidenced by the low-frequency C IV modulation map in Fig. 4.14.

**Network shadows.** Recently, Judge et al. (2001) have detected “magnetic shadows” in time-slice projections from SUMER measurements which they attribute to mode conversion in canopy fibrils (cf. McIntosh et al. 2001). In contrast to the power aureoles, these shadows are near-network areas that lack both in brightness and oscillatory power. Judge et al. (2001) plotted fractional modulation as defined by Eq. (4.4) which suggests that the shadows may correspond to the drop of the intermediate-category curve below the network one in the righthand panel of Fig. 4.13. Spatially resolved examples of such power normalisation are

given in the top panels of Fig. 4.17, selecting the 5-min and 2.5-min frequency bands of the 1600 Å subfield that are shown in Fig. 4.14 without normalisation. The low power (darkness) of the network areas illustrates the relative lowering of the network curves from Fig. 4.12 to Fig. 4.13. These dark patches extend slightly beyond the brightest cores of the network (first panel of Fig. 4.4) and so overflow into our intermediate pixel category (light grey in the fourth panel of Fig. 4.4). Blinking these normalised-amplitude maps against the mean brightness maps shows that the dark patches correspond closely to the network at a somewhat less restrictive brightness contour, i.e., that their darkness derives primarily through the normalisation from the averaged network brightness. The aureoles quantified in Fig. 4.16 extend further and remain discernable as patchy bright borders in the upper-right panel.

Blinking the normalised-amplitude maps between wavelengths shows that the dark patches darken and grow with decreasing wavelength. This is illustrated with the second row of Fig. 4.17 which displays the 1550/1700 Å normalised-map ratio. Bright noise results from division by small numbers; greyish areas mark comparable modulation amplitude at the two wavelengths. The dark areas in the 2.5-min panel result from contrast increase with formation height, with appreciable dark-patch widening. The same areas darken slightly in the 5-min ratio map at left.

In the interpretation of Judge et al. (2001) the dark-patch increase should map magnetic canopy expansion with height as increasing loss of wave amplitude due to mode conversion, but it actually follows the growth of the temporal-mean network patches in the first column of Fig. 4.14 through the pixel-by-pixel normalisation. The apparent growth of the latter patches with formation height is indeed likely to mark canopy spreading, but the shadow behaviour in Fig. 4.17 cannot be attributed to mode conversion unless the wave amplitudes indeed scale with the mean brightness. Again, it is not clear *a priori* whether this is the case. Magnetic mode conversion seems better established at larger atmospheric height than sampled by the TRACE ultraviolet passbands (McIntosh et al. 2001).

### 4.4.3 One-dimensional modulation spectra

Figures 4.18–4.22 provide a variety of Fourier spectra in a compact format, showing power spectra, coherence spectra and phase-difference spectra for different pairs of diagnostics with spatial averaging split between internetwork and network through masks as in Fig. 4.4. We first discuss Figs. 4.18–4.19 which are derived from the TRACE May 12 image sequences. Figure 4.18 compares the 1700 Å brightness modulation to 1600 Å brightness modulation; Fig. 4.19 does the same for the 1600 Å and 1550 Å pair. The latter pair samples somewhat greater heights but the large similarity of the two figures indicates that the oscillations persist without major change of character over the increase. This is not the case for the Ca II H diagnostics shown in Figs. 4.20–4.22 from the data of Paper I simulated by CS1997, which again provide a useful comparison.

**Power and coherence.** The mask-defined spatial means of the temporal power spectra for each of the two passbands are shown at the bottom of each panel. They are the same as in Fig. 4.12 and are added here for reference, but now plotted on logarithmic scales to permit appreciation of the mean value and the high-frequency noise level. The units are the arbitrary

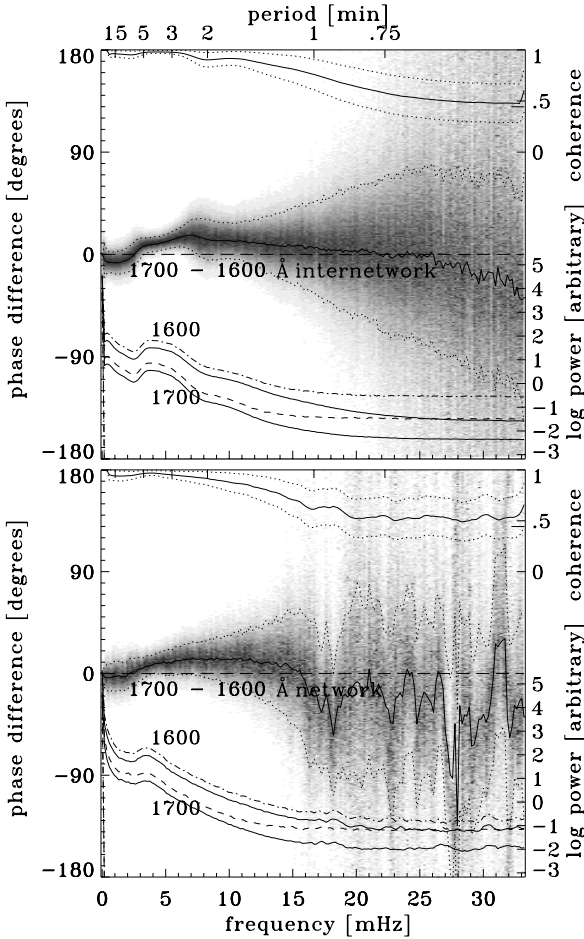


Figure 4.18: Temporal Fourier spectra of the May 12 brightness data for 1700 and 1600 Å, spatially averaged over internetwork (upper panel, 7838 pixels) and network (lower panel, 37712 pixels). Abscissae: temporal frequency, corresponding periodicity specified along the top. Solid curves in the lower half of each panel: power spectra on a logarithmic scale (at right), with  $1\sigma$  estimates (dash-dotted and dashed curves, the lower ones drop below the panel due to the logarithmic scaling). Solid curve in the upper half of each panel: coherence  $C$  between 1700 and 1600 Å, with  $1\sigma$  estimates (dotted; scale at right, the extra tick indicates the  $C = 0.45$  random noise value). Scatter diagram in the middle of each panel: phase differences  $\Delta\phi(1700-1600)$ , scale at left, positive values corresponding to 1700 Å brightness leading 1600 Å brightness. Each spatial sample per frequency was weighted by the corresponding cross-power amplitude  $\sqrt{P_1 P_2}$  and then binned into a greyscale plot normalised to the same maximum darkness per frequency bin (column). The solid curve is the spatial vector average defined by Eq. (4.7); the dotted  $1\sigma$  curves are determined from the weighted phase differences. Pure noise produces  $\Delta\phi$  scatter over all angles and correspondingly jagged behaviour of the mean  $\Delta\phi$  curve.

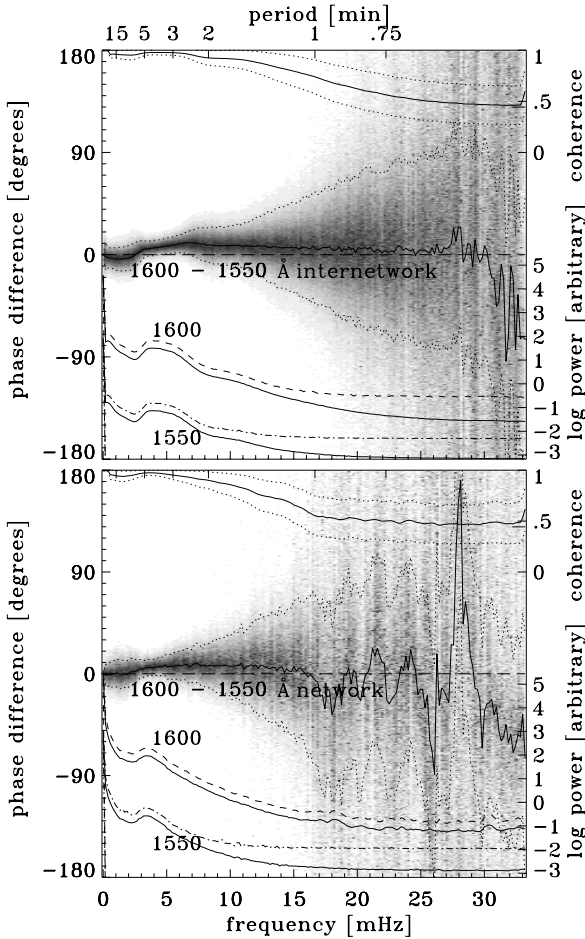


Figure 4.19: Temporal Fourier spectra of the May 12 brightness data for 1600 Å and 1550 Å, spatially averaged over internetwork (upper panel) and network (lower panel). Format as for Fig. 4.18.

TRACE data units. The same power spectra are shown with zero-frequency normalisation in Fig. 4.26. The combined network plus internetwork 1700 Å power spectrum is shown on a linear power scale in Fig. 4.23.

The mean brightness (zero frequency) and lowest-frequency modulation have much larger power than the acoustic oscillation peaks. The spectra show a gradual decline to the noise level at high frequency, with noisier behaviour of the network curves in the lower panel due to the smaller number of pixels.

The coherence  $C$  between the members of each pair is plotted at the top of each panel,

also with  $1\sigma$  error estimates (scale at right). We remind the reader that random noise gives  $C = 0.45$  with our method of frequency averaging plus spatially independent sampling. The coherences are significant for  $f < 15$  mHz in all panels of Figs. 4.18–4.19 and are very high in the 5–3 min band.

**Phase differences.** The phase-difference spectra are the most informative part of Figs. 4.18–4.19. The pixel-by-pixel  $\Delta\phi(x, y, f)$  values are shown as binned greyscale images in the format of Lites & Chipman (1979), weighting each  $(X, Y, f)$  sample by the cross-power amplitude. The greyscale is scaled to the same maximum blackness for each frequency bin (column) in order to appreciate the spread also at low power. The spatial averages are obtained vectorially as defined by Eq. (4.7) in Sect. 4.2 and are plotted as solid curves through the scatter clouds, with  $1\sigma$  curves determined from the weighted and binned distributions.

The spatial samples bunch up tightly in the acoustic oscillation band where the coherence is high, especially for the internetwork. The large amount of spatial sampling in our large-field image sequences yields very good statistics so that the average phase differences (solid curve) are very well determined in this band. At higher frequency the scatter increases. Note that pure random noise causes random scatter over all angles which does not average out to zero but produces equally erratic excursions of the average curves, with  $1\sigma$  spread over 0.68 of the figure height. Such behaviour is seen at high frequency for the network averages, which are based on a smaller spatial sample.

The internetwork phase-difference behaviour in Figs. 4.18–4.19 follows a well-defined pattern. It was observed earlier using optical lines (e.g., Fig. 7 of Lites & Chipman 1979; Fig. 7 of Lites et al. 1982; Fig. 7 of Paper I) and far-infrared continua (Kopp et al. 1992), but it is recovered here with much higher precision. At the lowest frequencies the internetwork shows a small but significant negative phase difference, meaning that the deeper-formed (longer wavelength) intensity lags the higher-formed intensity. This is attributed to internal gravity waves below. The 5-min oscillation ( $f = 3.3$  mHz) has slightly positive  $I-I$  phase difference due to radiative damping (comparable  $V-V$  spectra as in the lower-left panel of Fig. 4.20 have zero phase difference as expected for evanescent waves). The phase difference then shows a gradual increase out to  $f \approx 7$  mHz, implying upward acoustic wave propagation with the higher-formed 1600 Å brightness lagging 1700 Å brightness. The gradual increase follows the tilted line through  $\Delta\phi = 0$  which would hold if the same height difference  $\Delta h$  is sampled at each frequency and if all waves propagate up at the same speed  $c_s$  so that  $\Delta\phi = (\Delta h/c_s)f$  (cf. Lites & Chipman 1979). In this interpretation the increase has  $\Delta h \approx 100$  km as characteristic value until  $f = 7$  mHz where a slow decrease to  $\Delta\phi = 0$  sets in. We return to this pattern after a comparison with Ca II H formation.

**Comparison with Ca II H.** It is again useful to compare our TRACE results with the Ca II H spectrogram sequence of Paper I. That analysis targeted network oscillations; Figs. 4.20–4.22 present unpublished but informative internetwork measurements from these data in a comprehensive Fourier format similar to Figs. 4.18–4.19. Figure 4.20 displays wing modulation sufficiently far from H-line center to portray acoustic oscillations in the middle photosphere where they behave linearly in well-known fashion. Figures 4.21–4.22 use the  $H_{2V}$  brightness index which portrays nonlinear chromospheric kinetics in complex fashion.

These figures bracket our TRACE data in formation height.

The upper panels of Fig. 4.20 compare  $I-I$  internetwork Fourier modulation of the brightness in three blend-free spectral windows in the blue wing of Ca II H indicated by bars in Fig. 4.8. The oscillatory power peak becomes more pronounced at smaller separation from line center, i.e., higher formation. The  $I-I$  phase-difference patterns are very similar to the phase-difference patterns in Figs. 4.18–4.19.

The lower panels of Figure 4.20 add Dopplershift analysis for the weakest Fe I blend in the Ca II H spectra, which is the line at  $\lambda = 3966.82 \text{ \AA}$  used by CS1997 to define their simulation piston. It samples height  $h \approx 250 \text{ km}$  above the  $\tau_{5000} = 1$  surface. The lefthand panel shows a  $V-V$  comparison with the strongest Fe I blend in the Ca II H spectra (cf. Fig. 4.8) which was estimated to represent  $h \approx 390 \text{ km}$  in Paper I from the phase difference at  $f = 8 \text{ mHz}$  in this panel. The two power spectra have the same shape. Both lack the prominent low-frequency peak present in the brightness power spectra in the upper panels, but it should be noted that substantial spectrograph wavelength drift was removed from these Dopplershift measurements through nonlinear fit subtraction, a procedure which suppresses the small low-frequency peaks that do show up in the very similar (but more stable) data of Lites et al. (1994). The corresponding overshoot motions were therefore also not included in the simulation piston of CS1997, as shown by the piston power spectrum in Fig. 1 of Theurer et al. (1997a).

The  $V-V$  phase-difference spectrum shows evanescent behaviour for the five-minute waves and again displays upward propagation at higher frequencies up to  $f \approx 10 \text{ mHz}$  (blueshift is positive in this paper). The  $V-V$  five-minute band shows very high coherence and a smaller spread than in the  $I-I$  upper panels but the spread becomes slightly larger for the propagating regime because Dopplershift measurement is noisier.

The lower-right panel of Figure 4.20 shows a  $V-I$  comparison between Fe I 3966.82 Dopplershift and the Ca II H wing intensity at  $\Delta\lambda = -1.36 \text{ \AA}$ . Such  $V-I$  comparisons usually assume that brightness represents temperature, Dopplershift measures velocity, and that the two sample the same atmospheric height for a given spectral line. These assumptions are often erroneous and can be very misleading (cf. Skartlien et al. 1994; Stein & Carlsson 1997); are they valid here? The Ca II H wing is not too much affected by coherent resonance scattering this far from line center (e.g., Uitenbroek 1989) and should obey LTE reasonably well, and the Fe I blends are also quite likely to have LTE source functions even when their opacity is depleted by radiative overionization (Athay & Lites 1972, cf. Rutten 1988). Figure 4.8 shows that the Fe I 3966.82 line core and the  $-1.36 \text{ \AA}$  wing window have the same spatially-averaged emergent intensity, which with LTE and the Eddington-Barbier approximation implies formation at the same average temperature and so at the same height. Indeed, their acoustic power peaks coincide and their phase differences are roughly constant with frequency. Thus, the classical assumptions do hold in this case. At the coherence peak at  $f = 5 \text{ mHz}$  the  $V-I$  lag of about  $-120^\circ$  fits the compilations from many lines in Figs. 1 and 3 of Deubner (1990) at the  $h \approx 250 \text{ km}$  formation height and fits the classical interpretation of near-adiabaticity with some thermal relaxation (Schmieder 1976, 1977, 1978; Lites & Chipman 1979; Kopp et al. 1992).

Thus, all is well in Figure 4.20. The TRACE Fourier spectra in Fig. 4.18 show comfortably similar  $I-I$  behaviour with much better measurement statistics. Although the ultraviolet continua are not formed in LTE they apparently sample the same oscillations with similar height discrimination.

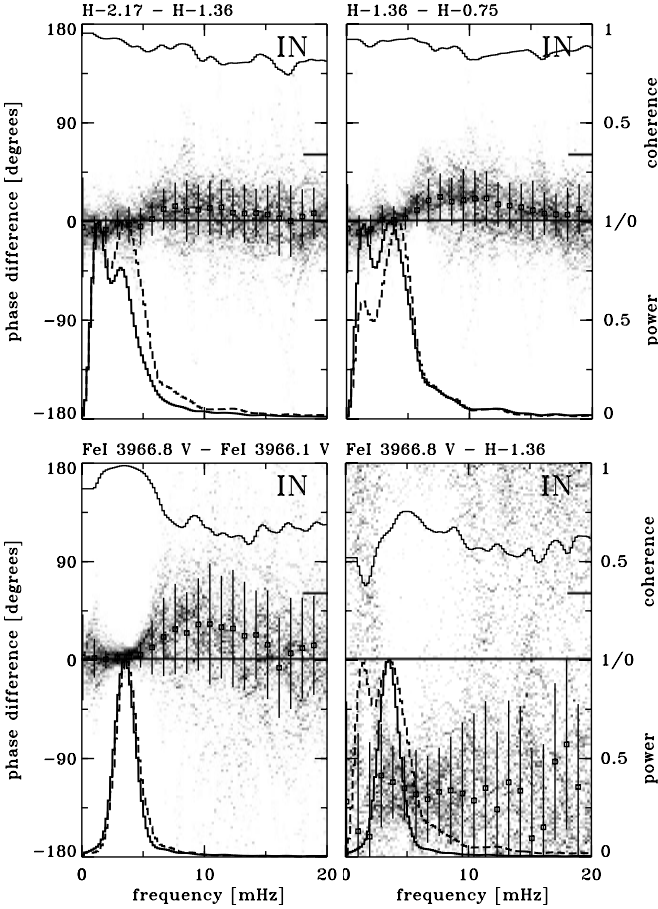


Figure 4.20: Photospheric comparison Fourier spectra from the Ca II H data presented in Paper I. The format follows Lites et al. (1994) and is similar to that of Figs. 4.18–4.19, but the power spectra (curves in lower half) are on linear scales normalised to their peaks with the mean removed, the coherence (curve in upper half) was evaluated with 9-point frequency averaging so that  $C = 0.33$  for random noise (dash at right), the vector averages of the phase differences are shown as solid dots, and the  $1\sigma$  estimates around the averages are plotted as bars. The lowest Dopplershift frequencies were removed in spectrograph drift correction ( $V$  spectra in lower panels). The various diagnostics are indicated in Fig. 4.8, are formed well away from the H-line center, and are measured from internetwork only (IN). First panel:  $I-I$  spectra for Ca II H wing brightness at  $\Delta\lambda = -2.17 \text{ \AA}$  and  $-1.36 \text{ \AA}$  from H center. Second panel: the same for wing brightness at  $-1.36 \text{ \AA}$  and  $-0.75 \text{ \AA}$ . Third panel:  $V-V$  spectra for Fe I 3966.82  $\text{\AA}$  and Fe I 3966.07  $\text{\AA}$  Dopplershifts. Fourth panel:  $V-I$  spectra for Fe I 3966.82  $\text{\AA}$  Dopplershift and wing brightness at  $-1.36 \text{ \AA}$ .

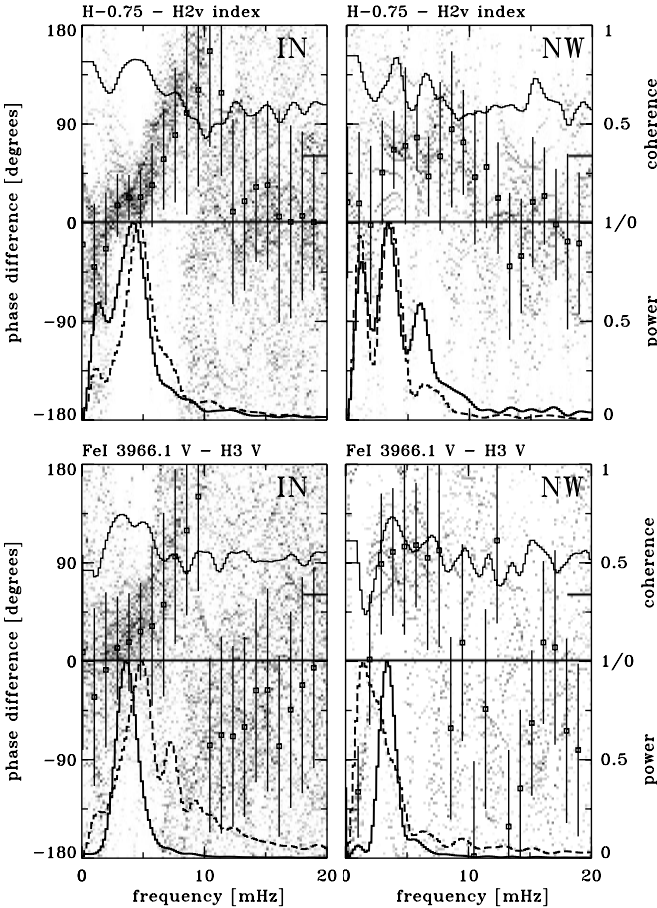


Figure 4.21: Chromospheric comparison spectra from the Ca II H data discussed in Paper I in the format of Fig. 4.20. Left: internetwork. Right: network. Upper panels:  $I-I$  spectra for wing brightness at  $\Delta\lambda = -0.75 \text{ \AA}$  and  $H_{2V}$  index brightness. Lower panels:  $V-V$  spectra for Fe I 3966.07  $\text{\AA}$  Dopplershift and Ca II  $H_3$  line-center Dopplershift.

However, TRACE images and timeslices as in Figs. 4.5–4.7 display internetwork grains much like Ca II K filtergrams, so that comparison should also be made with Ca II H formation closer to line center. This is done in Figs. 4.21–4.22. The upper panels of Fig. 4.21 show internetwork and network  $I-I$  comparisons using the  $H_{2V}$  brightness index of which the timeslice is shown in Fig. 4.9 and decomposed in Fig. 4.10. Its internetwork power spectrum is dominated by the  $f = 5 \text{ mHz}$  peak and its phase differences with the  $\Delta\lambda = -0.75 \text{ \AA}$  brightness rise steeply with frequency, reaching  $180^\circ$  at  $f = 10 \text{ mHz}$ . Spectrally, this upward

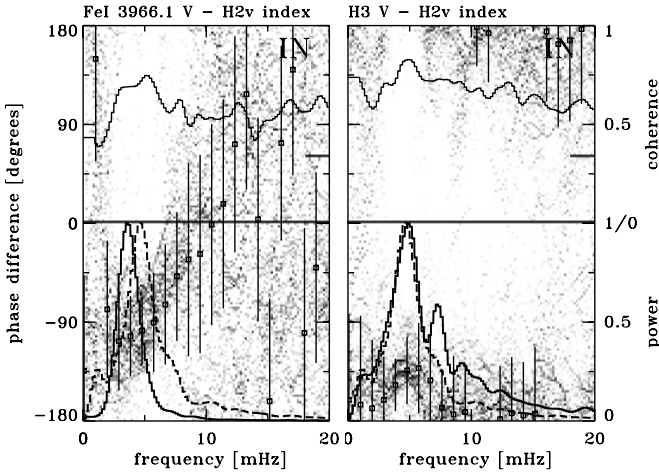


Figure 4.22: Chromospheric  $V-I$  spectra from the Ca II H data in Paper I for internetwork. Left: Fe I 3966.07 Å Dopplershift and  $H_{2V}$  index. Right:  $H_3$  Dopplershift and  $H_{2V}$  index. The rms  $\Delta\phi$  bars wrap around from below  $-180^\circ$  to above  $+180^\circ$  and vice-versa.

propagation of the brightness modulation in the Ca II H & K wings was diagnosed from inward wing whisker contraction already by Beckers & Artzner (1974). It causes the fuzziness in the time direction of the  $H_{2V}$  grains in the wide-band timeslice at right in Fig. 4.9. The steep  $\Delta\phi(I-I)$  gradient across the three-minute band also contributes apparent dissimilarity between the two three-minute slices of Fig. 4.10 because it washes out timeslice structure with sampling height even at high coherence. The larger similarity of the internetwork parts of the two five-minute slices in Fig. 4.10 corresponds to constancy across the five-minute band of the total  $\Delta\phi$  sum of the two righthand panels of Fig. 4.20 and the upper-left panel of Fig. 4.21.

The steep  $\Delta\phi(I-I)$  increase is in conflict with the small amount of propagative difference in Fig. 4.19 if one assigns  $H_{2V}$  brightness formation to temperature behaviour at temperature-minimum formation height. This would be the case if one assumes that equal time-averaged emergent intensity implies the same formation height, as proven above for the Fe I 3966.82 Å and  $\Delta\lambda = -1.36$  Å pair. One would then assign Fe I 3966.82 Å and the  $H_{2V}$  index to the same layer on the basis of their equal mean intensity in Fig. 4.8, but the assumption is wrong as indicated by the Fe I 3966.82 – Ca II  $H_3$   $V-V$  comparison in the lower-left panel which shows a similar  $\Delta\phi(f)$  gradient but spans a much larger height interval. The similarity illustrates that  $H_{2V}$  brightness is strongly influenced by the Dopplershift excursions of the  $H_3$  core well above the layer where the  $H_{2V}$  photons escape, with  $H_{2V}$  enhancements corresponding to  $H_3$  redshifts. This well-known relationship, initially proposed and modelled by Athay (1970), Cram (1972), and Liu & Skumanich (1974), is explained in detail in the informative H-line formation break-down diagrams in Figs. 4–7 of CS1997 and is here demonstrated observationally by the  $V-I$  diagrams in Fig. 4.22. In the righthand panel the coherence is higher, the two three-minute power peaks are virtually identical, and  $\Delta\phi(V-I)$  is roughly constant

with frequency. Thus, the steep  $\Delta\phi$  increases in the  $I-I$  and the  $V-V$  internetwork panels of Fig. 4.21 are both set by  $H_3$  Dopplershift modulation. The same increase was observed in Fig. 5 of Lites & Chipman (1979) and the grain-rich  $V-V$  diagram from 1991 data in Fig. 5 of Rutten (1994), and it is also present (with a sign-definition flip) in Fig. 4 of Skartlien et al. (1994) which evaluates  $V-V$  phase difference for the Ca II  $H_3 - 8542 \text{ \AA}$  line pair from the CS1997 simulation, confirming that the increase is a characteristic of acoustic shock dynamics.

We conclude from this comparison that the internetwork Fourier behaviour diagnosed in Figs. 4.18–4.19 samples oscillations comparably to the inner wings of the Ca II H & K lines, but without the brightness enhancement that internetwork grains gain when observed at the  $K_{2V}$  and  $H_{2V}$  wavelengths from the large-amplitude shock modulation of the  $H_3$  Dopplershift in higher layers.

**High-frequency waves.** Phase-difference measurements with TRACE should permit recognition of oscillation signatures to higher frequencies than is possible in ground-based observations. The interest in diagnosing high-frequency oscillations is large, for example to settle the current debate on chromospheric heating by high-frequency acoustic waves and their presence or absence in the Carlsson & Stein piston (Musielak et al. 1994; Theurer et al. 1997a; Theurer et al. 1997b; Ulmschneider 1999; Kalkofen et al. 1999) and its stellar ramifications (Cuntz et al. 1999).

The phase-difference spectra in Figs. 4.18–4.19 show gradual decrease above  $f \approx 7 \text{ mHz}$ . In older oscillation studies such declines have generally been attributed to atmospheric seeing (e.g., Endler & Deubner 1983; Deubner et al. 1984; Deubner & Fleck 1990; see Lites et al. 1994 for a discussion). In TRACE observations, however, there is no seeing apart from the small-scale guiding jitter that has mostly been removed by our alignment procedures. However, also from space acoustic oscillations are harder to measure at higher frequency because the wavelength shortens: at soundspeed propagation it drops to 350 km for  $f = 20 \text{ mHz}$ . An upwards propagating wave may fit from maximum compression to maximum rarefaction within the response function width, so that much less power is detected than actually present – but even in that case phase difference may yet be measurable.

In this context the phase-difference behaviour for  $f = 10 - 20 \text{ mHz}$  in the two lefthand panels of Fig. 4.21 should be noted. The noise is large (the  $1\sigma$  bars nearly reaching their maximum extent of 68% of the panel height) but the averages seem to display a pattern which we deem possibly significant because similar behaviour is seen in Fig. 5 of Lites & Chipman (1979) and Fig. 7 of Rutten (1994).

Figures 4.18–4.19 show no high-frequency behaviour analogous to the internetwork behaviour to Fig. 4.21 at all, only the gradual  $\Delta\phi$  decrease. The latter seems significant even though the power drops strongly towards  $f = 10 \text{ mHz}$ . We suggest that the phase difference decline results primarily from non-linear wave steepening. On their way to become weak acoustic shocks in the low chromosphere, the higher-frequency components travel faster and arrive earlier at the higher sampling location. In the TRACE brightness measurements the steepening is sampled far below the level that produces the patterns seen in Fig. 4.21, which must both be attributed to  $K_3$  Dopplershift behaviour as discussed above. Thus, the  $\Delta\phi$  decreases in Figs. 4.18–4.19 sample nonlinear wave steepening at its onset, well below the

level where shocks result and produce  $H_{2V}$  and  $K_{2V}$  grains as well as observable sawtooth behaviour. The question to what maximum frequency these  $\Delta\phi$  decreases are significant is addressed in Sect. 4.5 where we conclude that the non-simultaneity of the TRACE imaging in the different passbands sets the  $\Delta\phi$  reliability limit to  $f = 15$  mHz at best.

**Network–internetwork differences.** The network panels in Figs. 4.18–4.19 differ only slightly from the internetwork panels. The differences in power spectra are exhibited more clearly in Figs. 4.12–4.13 and correspond to the relative lack of network power in the 2.5–min maps in Fig. 4.14. The coherences drop a bit faster with frequency in the network and the phase-difference scatter is slightly larger even in the five-minute band. The large similarity with the internetwork behaviour shows that the acoustic oscillations pervade network at these heights without much modification, as they do in the photosphere (plots as in Fig. 4.20 for network, not shown, are identical apart from small-sample noise).

The picture is drastically different for the chromospheric diagnostics in Fig. 4.21 where power spectra and phase difference behaviour are very different between network and internetwork. The fourth panel illustrates the conclusion of Paper I that the long-period modulation peak that is particular to chromospheric network sampled by  $H_3$  Dopplershift has no connection (low coherence) to the dynamics of the underlying photosphere. This disconnection is demonstrated here by the large disparity in internetwork–network differences between Fig. 4.19 (upper and lower panels nearly the same) and Fig. 4.21 (left and right panels very different).

#### 4.4.4 Two-dimensional modulation spectra

Figures 4.23–4.24 complete our suite of Fourier diagnostics for the May 12 data in the form of two-dimensional power and phase-difference spectra, resolving the oscillations in both temporal frequency  $f$  (vertical) and in spatial wavenumber  $k_h$  through annular averaging over the horizontal  $(k_x, k_y)$  plane. These spatially-averaged diagrams make no distinction between internetwork and network. Only the lower-left  $(k_h, f)$  quadrants with significant structure are shown.

**Acoustic oscillations.** Figure 4.23 shows the  $(k_h, f)$  power spectrum for the May 12 1700 Å data. The solid curves are the spatially and temporally averaged power spectra, respectively. The one at right is the combination of the internetwork and network 1700 Å power spectra in Fig. 4.18 but is here plotted on a linear scale with removal of the mean and trend to emphasise the low-frequency and acoustic modulation peaks.

The  $(k_h, f)$  power spectrum contains  $p$ -mode ( $f = 2–5$  mHz) and pseudo-mode (above the cutoff frequency  $f_{AC} = 5.3$  mHz) power ridges out to  $f = 8$  mHz and to  $k_h = 3.2 \text{ arcsec}^{-1}$  or spatial wavelength  $\Lambda_h = 2 \text{ arcsec}$  (scale on top; the latter limit may be set by the 1.5 arcsec boxcar image smoothing of the May 12 sequences). The pseudo-mode ridges do not originate from global mode selection through multi-pass interference, as is the case for the evanescent five-minute modes used in helioseismology, but come from waves that are excited near the surface in downward directions and are reflected only once at the inward temperature increase before propagating upwards out of the photosphere. They add power to

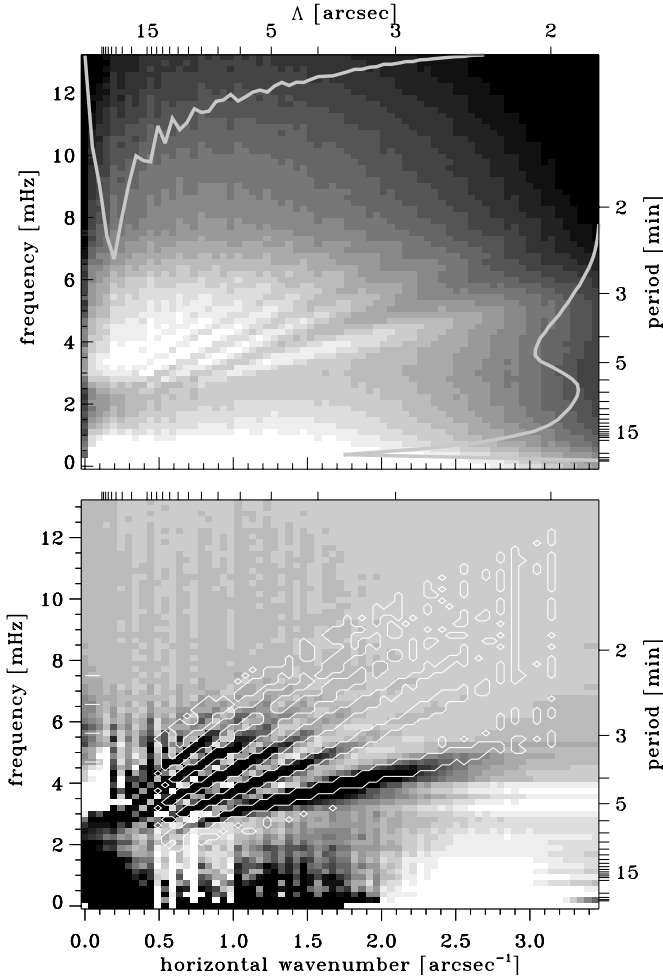


Figure 4.23: Partial two-dimensional power spectra of the 1700 Å brightness in the complete May 12 sequence (full field and duration). Only the significant part is shown. Axes: horizontal wavenumber  $k_h$  and temporal frequency  $f$ . The corresponding spatial wavelengths and temporal periodicities are specified along the top and at right. Upper panel: absolute brightness power on logarithmic greyscale. The solid curves show the temporally and spatially integrated power spectra on linear inverted scales with the mean and trend removed. Lower panel: the same after subtraction of the background variation to enhance the  $p$ -mode and pseudo-mode ridges, and with the greyscale inverted to display the contours better. The latter define the ridge mask. The vertical fringing is an artifact from TRACE data compression.

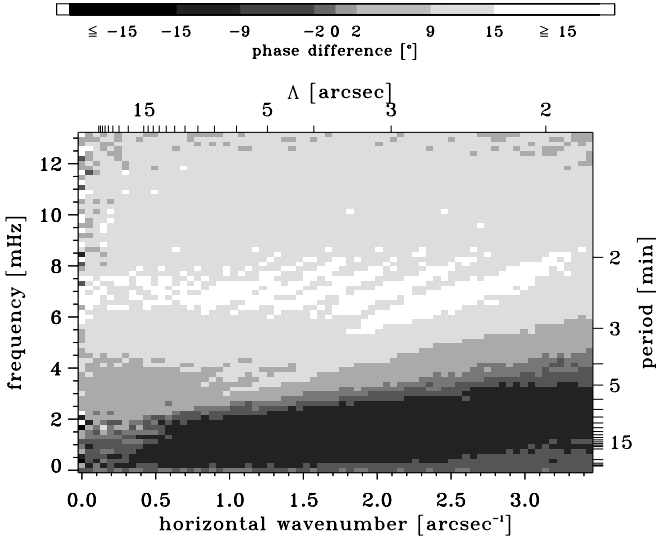


Figure 4.24: Two-dimensional  $\Delta\phi(1700\text{--}1600)$  phase-difference spectrum from the May 12 data. Axes: horizontal wavenumber  $k_h$  and temporal frequency  $f$ . The corresponding wavelengths and periodicities are specified along the top and at right. Greyscale: phase difference  $\Delta\phi$  coded as indicated at the top.

the directly excited outgoing wave at  $(k_h, f)$  locations corresponding to the one-bounce travel length and duration from the source. Thus, they do not represent global wave interference but local power addition. They correspond to first-bounce power ridges in time-distance plots in which the appearance of only one ridge for three-minute waves established the up-and-out loss after the first reflection (Duvall et al. 1993), and they roughly obey the Duvall dispersion law for a fixed waveguide with  $n$  nodes along its length (Duvall 1982; cf. Eq. 2.14 of Deubner & Gough 1984; see also Kumar et al. 1994, Kumar 1994, Jefferies 1998, Vorontsov et al. 1998).

Figure 4.24 shows the  $(k_h, f)$  diagram for the May 12 1700–1600 Å phase differences. The pseudo-mode ridges stand out by having larger  $\Delta\phi(1700 - 1600)$  values than between the ridges, representing a ridge-interridge split of the  $\Delta\phi$  averages in Fig. 4.18. Since the ridges correspond to single-bounce power enhancements in  $(k_h, f)$  selection, they are likely to correspond to locations where acoustic waves propagate vertically upwards. The on-ridge  $\Delta\phi(1700 - 1600)$  values then correspond to vertical travel time between the two sampling heights for such waves. They do not stand out through interference between spatially different locations but because outward propagation is enhanced at the  $(k_h, f)$  ridge locations.

The interridge background has smaller phase differences, implying partial non-propagative signature (oblique propagation would increase the delay). We suspect that these smaller differences are standing-wave contributions from partial reflections at larger height, possibly at shocks (e.g., Deubner et al. 1996; Carlsson & Stein 1999), or from deep penetration of ballistic post-shock downfall. In the Carlsson-Stein simulation, shocks are sometimes stopped in their upward propagation by such downdrafts after prior shocks. Such a case is observation-

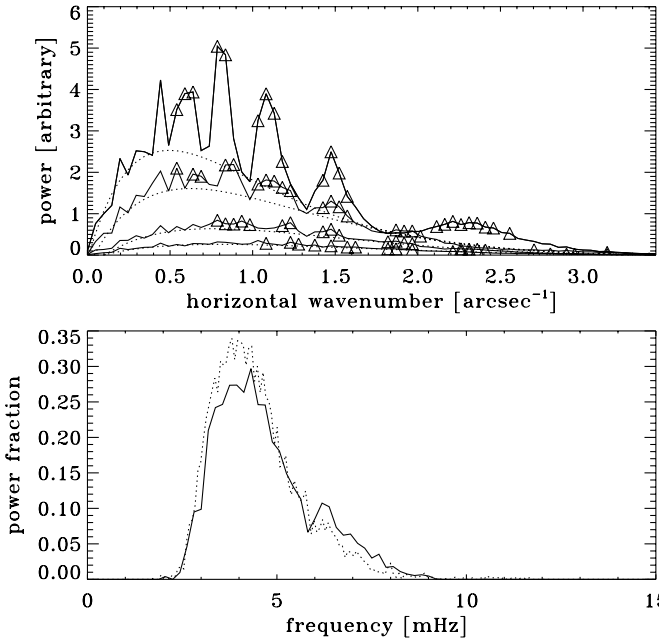


Figure 4.25: Upper panel: absolute power in 1700 Å brightness as function of horizontal wavenumber at different frequencies, from top to bottom 4.7, 5.6, 6.6, 7.5 mHz. Triangles: ridge locations as in Fig. 4.23. Dotted curves: background estimates underlying the ridges. Lower panel: fraction of the summed ridge power (above the dotted backgrounds in the upper plot) of the total power, as function of frequency. The dotted curve results from the longer-duration October 14 sequence.

ally present in the form of the triple-grain sequence at the top of C+S column 30 ( $x = 63$ ) in Figs. 4.9–4.11. When blinking the upper and lower rightmost panels of Fig. 4.10 against each other, the upward propagation of the three-minute waves is immediately evident as up-and-down jumping patterns – except for this particular grain train which appears standing still when blinked, so simultaneously present at the two sampling heights, with zero phase difference.

Not only does the interridge background have distinctly different phase behaviour at pseudo-mode frequencies but it also has appreciable power in the whole acoustic regime. This is quantified in Fig. 4.25. The upper panel shows power distributions along horizontal cuts through the  $(k_h, f)$  diagram in Fig. 4.23. The ridges defined by the ridge mask (lower panel of Fig. 4.23) are indicated by triangles. The dotted curves are background estimations. The lower panel shows the fraction of ridge power above the local background summed over all mask ridges along horizontal cuts. The ridge power is most important below the cutoff frequency but even there the background contribution is sizable. The latter rapidly gains importance with frequency above the cutoff frequency.

In the  $p$ -mode regime below the cutoff frequency the on-ridge power enhancements represent constructive interference of global oscillations with long-duration mode persistence, whereas the  $p$ -mode background represents shorter-duration wavetrains from local excitations without global mode selection. Long-duration sampling as in helioseismology increases the ridge/interridge power contrast because shorter wavetrains then cancel through having random phases. In contrast, pseudo-mode ridges do not correspond to such long-duration persistence and may actually be dominated by local excitations, whereas the pseudo-mode background may have a larger interference contribution from wave reflections. This intrinsic difference is illustrated by the difference between the two curves in the lower panel of Fig. 4.25. The twice longer duration of the October 14 sequence (dotted curve) produces higher contrast for the  $p$ -mode ridges but lower contrast for the pseudo-mode ones.

**Low-frequency oscillations.** At lower frequency, the dark wedge in Fig. 4.24 indicates downward propagation which corresponds to the initial  $\Delta\phi < 0$  dip in the upper panels of Figs. 4.18 and 4.20. The wedge shape, the location of the upper limit at the Lamb line, and the larger-than-granule wavelengths suggest strongly that this wedge is due to internal gravity waves (cf. Straus & Bonaccini 1997). It was previously observed in similar  $(k_h, f)$  spectra from ground-based filtergram sequences by Kneer & von Uexküll (1993) who tentatively made the same identification, as did Schmieder (1976), Cram (1978b), Brown & Harrison (1980), Deubner & Fleck (1989), Bonet et al. (1991) and Komm et al. (1991) from various other diagnostics. The same tentative identification was made in Paper I for the low-frequency power peaks shown here in Fig. 4.20. These are much higher, relatively to the acoustic peak, than the low-frequency Doppler modulation by convective overshoot (which is artificially suppressed in the lower panels of Figs. 4.20–4.21 as noted above but remains well below the acoustic peak height in other data). We now confirm the identification as gravity waves from the  $(k_h, f)$  phase-difference signature in Fig. 4.24.

It is no surprise to find gravity waves in the upper photosphere since they should be abundantly excited by convective overshoot. However, their detection is not easy because they combine long periods and short wavelengths with small Dopplershifts and because they travel preferentially in slanted directions, so that sampling widely different heights along radial lines of sight suffers loss of coherency (see the detailed descriptions and predictions in the fundamental papers of Mihalas & Toomre 1981, 1982).

Our TRACE  $\Delta\phi(1700 - 1600)$  measurement represents a particularly sensitive gravity-wave diagnostic because (i) – it samples brightness rather than velocity, (ii) – does so sufficiently high (the intensity modulation grows considerably with height), but (iii) – yet below the wave breaking height above which the waves vanish, and (iv) – compares brightness phase at sufficiently close heights with sufficient spatial integration (1.5 arcsec boxcar smoothing) to detect slanted waves. The negative-phase signature is smaller for the higher-located sampling in Fig. 4.19; the corresponding  $(k_h, f)$  diagram (not shown) has similar ridge-interridge difference at smaller amplitude.

The gravity wave signature is similarly present in the Ca II H wing brightness modulation spectra in the upper panels of Fig. 4.20, for the same reasons: gravity waves have much larger brightness modulation than Dopplershift modulation, the brightness modulation is sampled at heights where the amplitude grows large before reaching breaking height, and the Ca II H

wing windows sample a sufficiently small height difference to avoid spatial mismatch from oblique propagation. In addition, since the H wings are formed in LTE they may respond more faithfully to temperature modulation than the ultraviolet continua which suffer from scattering. The low-frequency power peak is still weakly present in the internetwork  $H_{2V}$  index spectrum in the upper-left panel of Fig. 4.21.

Note that both  $H-0.75$  power and  $H_{2V}$  index power have a (relatively) more pronounced low-frequency peak in the network (upper-right panel of Fig. 4.21) and that this peak seems to survive as the only peak in internetwork  $H_3$  Dopplershift power (lower-right panel). The tantalising suggestion is that the  $H_3$  Dopplershift peak may result from fluxtube interaction at mid-photospheric heights with gravity waves impinging sideways from the surrounding internetwork that get enhanced in the fluxtube. An alternative interpretation is that the network  $H_3$  Dopplershift peak represents mottle flow dynamics as mapped by the second bottom panel of Fig. 4.14.

## 4.5 Error analysis

**Comparison with October 14 data.** For reasons of space we have only displayed results from the May 12 TRACE sequences so far. The October 14 sequences produce comparable timeslices, Fourier amplitude maps and Fourier spectra, with as major difference that the extreme quietness of the solar field makes the C IV construct yet more unreliable and dominated by noise. Nevertheless, the October 14 sequences provide a different sample that we use here to judge the reliability of the May 12 results, in particular the high-frequency parts of the Fourier spectra which are most sensitive to the nonsimultaneities and the cadence and timing irregularities of the TRACE image acquisition, which differ between the two dates.

Figure 4.26 compares Fourier spectra between the two dates in the format of Fig. 4.18 (but without scatter clouds and rms curves to avoid overcrowding). The power spectra are again plotted logarithmically but are now made comparable by zero-frequency normalisation as in Eq. (4.4). The October 14 power spectra have a higher noise level at high frequency. The acoustic peaks are about the same for the two dates.

The phase-difference averages differ much between the two dates from  $f \approx 15$  mHz onwards, even in the well-sampled internetwork (upper panels). The averaged coherences disagree appreciably at even lower frequency.

The TRACE fields sample a sizable fraction of the solar disk. The October 14 field was even quieter than the May 12 field but there is no reason to assume that the internetwork was intrinsically different between the two dates in these large spatial averages. Thus, we may expect the solar behaviour to have been similar at the two dates (except for the C IV construct), especially in the internetwork. The fact that the mean phase difference and coherence spectra differ so much above  $f \approx 15$  mHz implies that measurement errors and measurement differences are important and upset our anticipation of diagnosing high-frequency oscillation properties exploiting the TRACE virtues of seeing-less and statistically-rich sampling. Various tests were therefore made to elucidate these errors. The principal question is to what frequency the phase-difference spectra are reliable.

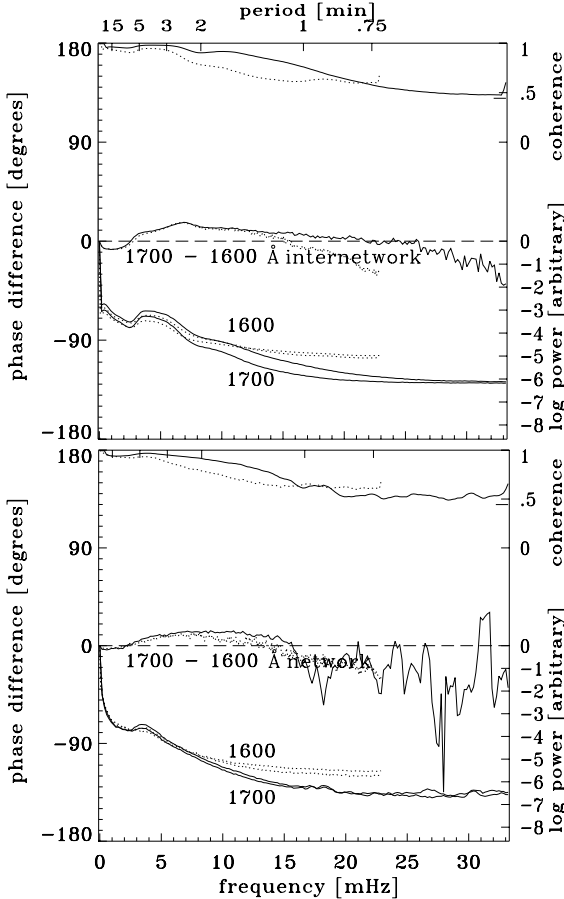


Figure 4.26: Comparison of the spatially averaged Fourier spectra from May 12 1998 and from October 14 1998. The solid curves are the same as in Fig. 4.18 except that the power spectra are normalised to the zero-frequency value (square of the mean intensity). The October 14 spectra are dashed and have a lower Nyquist frequency (23 mHz).

**Phase-difference closure.** A direct reliability test of the phase differences in Figs. 4.18–4.19 is available in the form of phase-difference closure. If each passband samples a well-defined oscillation phase per frequency, the  $\Delta\phi(1700-1550)$  differences should equal the summed  $\Delta\phi(1700-1600)$  and  $\Delta\phi(1600-1550)$  values. Figure 4.27 shows that the direct and summed evaluations depart between  $f = 10$  and  $f = 15$  mHz, and for the network at somewhat lower frequencies. This is the same frequency region in which the phase-difference spectra in Fig. 4.26 depart from each other, indicating that the averaged phase-difference spectra in Figs.

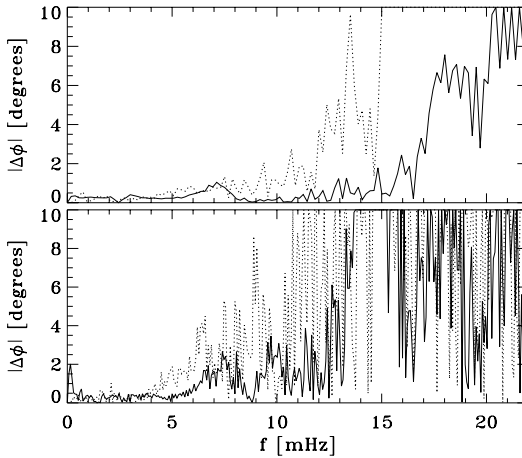


Figure 4.27: Phase-difference closure. The curves show  $|\Delta\phi(1700 - 1600) + \Delta\phi(1600 - 1550) - \Delta\phi(1700 - 1550)|$  where each  $\Delta\phi$  is the vector-averaged mean phase difference (solid curves in Figs. 4.18–4.19). Solid: internetwork. Dashed: network. Upper panel: May 12 data. Lower panel: October 14 data.

4.18–4.19 indeed become unreliable in this frequency band.

**Window taper.** In standard practice, the 10% start and end segments of the brightness sequence per pixel were multiplied by a 10% cosine bell taper to the mean value in order to suppress window edge effects. The original mean was restored as zero-frequency amplitude after the transform. Tests changing or even deleting the edge taper produced more high-frequency noise as expected from edge discontinuities (Brault & White 1971), but no significant change in phase-difference behaviour.

**Discrete sampling.** TRACE has no high-frequency filter to suppress noise above the Nyquist frequency. The power curves in Fig. 4.18 still decrease slightly close to the Nyquist frequency, so that some aliasing seems indeed to occur. However, the Nyquist frequency is quite high in the May 12 data. The power spectra are appreciably higher around  $f = 15$  mHz so that the phase-difference spectra should be dominated by non-aliased signal around this frequency. However, at higher frequencies the sampling itself becomes inadequate for phase measurements below the Nyquist frequency. These imply a three-parameter sinusoidal fit (amplitude, offset, and phase) to each signal per frequency and pixel, so that the uncertainties increase rapidly when the signal is sampled less than 3 times per period, i.e., above  $f \approx 17$  mHz for the May 12 data.

**Non-simultaneous sampling.** The worst phase-difference error source is the non-simultaneity of the imaging in the different passbands. In principle, the temporal offset between the

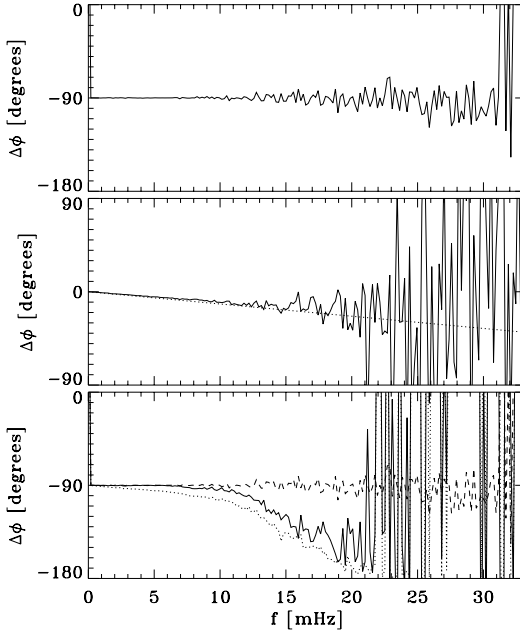


Figure 4.28: Phase-difference tests using 2500 pairs of artificial solar-like signals with random phase per frequency in the first signal. The top panel results when the second signal is identical to the first one apart from a phase delay of  $-90^\circ$  per frequency and both are sampled simultaneously with the actual TRACE 1600 Å timing sequence. The solid curve in the middle panel results when the two signals are identical (without phase delay) but are sampled TRACE-like with the 1600 and 1700 Å timing sequences, which have an average offset of 5 s. The dotted curve shows the phase difference for a constant offset of 5 s between signals. The dotted curve in the bottom panel shows the combination (two signals  $-90^\circ$  out of phase sampled TRACE-like). The solid curve includes correction for constant 5 s offset and emulates our phase difference evaluations from the actual data. The curve in the top panel is overlaid for comparison.

samples in two sequences introduces phase difference at each frequency that equals the offset divided by the period, a linear increase with frequency that was corrected using the equidistant time scale defined for each dataset. (The correction also makes  $\Delta\phi$  depart from  $0^\circ$  or  $\pm 180^\circ$  at the Nyquist frequency.) However, the actual timing irregularities and exposure durations cause uncertainties that also increase with frequency and become quite large at the high-frequency end – as demonstrated below.

**Sampling tests.** Figure 4.28 illustrates the effects of the major sampling errors on phase-difference measurements by using an artificially generated signal that possesses a solar-like power spectrum. Statistical variation was introduced by generating 2500 realizations in each of which the phase was chosen randomly at each frequency. The top panel illustrates errors due to discrete sampling and sampling irregularities alone. It uses the actual mid-exposure

timing sequence of the May 12 1600 Å data to measure phase differences between the 2500 artificial signals and 2500 copies that are phase-shifted over  $-90^\circ$  at each frequency. The curve shows the result from vector-averaged phase-difference determination as done above. The deviations from  $\Delta\phi = -90^\circ$  illustrate the errors caused by the non-equidistant exposure timing. They are reasonably small out to high frequencies.

The middle panel of Fig. 4.28 shows a similar test using 2500 pairs of identical (not phase-shifted) signals sampled with the actual 1600 and 1700 Å timing sequences. The noise increases considerably compared with the top panel.

The bottom panel results from a 2500-pair test combining the two error sources. It indicates that the irregular sampling of different signals at unequal times introduces large errors that cause appreciable  $\Delta\phi$  distortion for frequencies above  $f = 10$  mHz and large  $\Delta\phi$  scatter above  $f = 20$  mHz. The phase closure test in Fig. 4.27 indicates a somewhat larger extent of reliability, out to  $f = 15$  mHz for errors below  $10^\circ$ , in the internetwork which provided more samples than the 2500 used in these tests. The internetwork  $\Delta\phi$  curves in Fig. 4.26 also show equality up to  $f = 15$  mHz.

The conclusion is that, even though the TRACE data do not suffer from seeing, the sequential nature of TRACE's filter-wheel switching between passbands combined with the sampling irregularity is the major contributor of phase-difference noise and limits the reliability of the  $\Delta\phi$  spectra in Figs. 4.18–4.19 to frequencies below  $f \approx 15$  mHz.

## 4.6 Discussion

**Acoustic oscillations.** A major supplier of dynamics in the internetwork atmosphere at the heights sampled by TRACE's ultraviolet passbands is, obviously, the so-called chromospheric three-minute oscillation, i.e., the broad peak for 2–5 min periodicity in the spatially-averaged power spectra in Figs. 4.12–4.13 and 4.23. The fast-changing “sea of motion” sampled by the cutouts in Fig. 4.5, the dappled appearance of the internetwork parts of the timeslices in Fig. 4.7, the tight concentration of the three-minute  $\Delta\phi$  spread in Figs. 4.18–4.19, and the amount of three-minute power in Fig. 4.12 all attest to this ubiquitous oscillation gaining dynamical dominance already in the upper photosphere. There is not much else happening at these heights for frequencies around  $f = 5$  mHz or the coherences wouldn't be so high and the  $\Delta\phi$  spreads wouldn't be so small.

Our extensive comparisons with comparable displays from the Ca II H data of Lites et al. (1993) in Figs. 4.9–4.11 and Figs. 4.20–4.22 show that the ultraviolet continua sample the upper photosphere and low chromosphere rather like the inner wings of Ca II H, but without the higher-up Dopplershift effects of H<sub>3</sub> that produce the spectral asymmetry and intricate time-dependent spectral variations of the H & K emission reversals. Since the spectral Ca II H behaviour in these very data was convincingly reproduced by the simulations of CS1997, we deem it beyond doubt that the highly similar internetwork behaviour in the ultraviolet timeslices and Fourier spectra is set by acoustic waves that are steepening into weak shocks on their way up. As discussed in Sect. 4.4.3, we suspect that the mean  $\Delta\phi$  decline in Figs. 4.18–4.19 from  $f \approx 7$  mHz to  $f \approx 15$  mHz (where  $\Delta\phi$  becomes unreliable) results at least partially from wave steepening. We suspect also that similar phase-difference declines in older ground-based data were also partially due to wave steepening rather than atmospheric seeing.

Many of our results, in particular the phase differences in Figs. 4.18–4.19, are amenable to radiation-hydrodynamics simulations as those of Skartlien et al. (1994). Compared to their Ca II H modelling, the lower heights of formation of the ultraviolet continua (implying smaller sensitivity to canopy geometry) and the more straightforward computation (no sensitivity to unidentified microturbulence or to coherency in resonance and Raman scattering) warrant the expectation that such numerical modelling should reproduce our observations in considerable detail. The major obstacle might be the one-dimensionality of the Carlsson-Stein approach, but it should be noted that the spatial extent of the time-compressed internetwork features in the lower panel of Fig. 4.11 is appreciably larger than the pixel size; column shifts of 1–2 arcsec (700–1500 km) sample scene differences primarily in the form of phase shifts, whereas the radial stratification varies much more rapidly.

The ongoing debate on the presence or absence, both in the Carlsson-Stein Ca II H simulation and in the real Sun, of a sizable heating contribution by high-frequency waves (e.g., Kalkofen et al. 1999) is not decided by our data. Our initial expectations were that phase differences should provide the clearest signature of high-frequency oscillations in the presence of much larger power at lower frequencies, and that the ultraviolet continua, which are formed at heights where wave amplitudes grow and steepen but are not yet disturbed by magnetic canopies, should provide the best diagnostic. Our hope was that TRACE's seeing-free and large-sample data gathering would unequivocally settle this issue – but we did not anticipate that the sequentiality of TRACE's imaging in different passbands upsets phase difference measurements as far below the Nyquist frequency as shown in Sect. 4.5. Of course, the wide contribution functions of the ultraviolet continua (sampled by TRACE with very wide passbands), the reduced sensitivity to thermal modulation caused by resonance-like bound-free scattering in these continua, and slowness of the pertinent recombination rates may together cause low modulation sensitivity and so limit the detectability of high-frequency phases. Numerical simulations can assess which waves may leave what signature in TRACE-like data and indicate up to what frequency waves are at all observable with future (or ideal) instruments.

Excess sound emission from collapsing granules (Skartlien 1998; Rast 1999; Skartlien et al. 2000), in intergranular lanes within mesoscale convergence areas (Hoekzema & Brandt 2000) and in acoustic flux events (Goode et al. 1998) as well as wave refraction (Hoekzema et al. 1998b; Stix 2000) are likely to contribute some mapping of granular dynamics into the acoustic modulation pattern. For oscillations with long-duration persistence as the global  $p$ -modes, the signatures of local excitations are largely – if not fully – lost in the many-wave and multi-pass interference that produces the wavy-curtain five-minute timeslice patterns (e.g., Fig. 4.9), but above the cutoff frequency the pseudo-mode ridges are mostly due to single-bounce enhancement so that more of the excitation pattern may remain. However, the rapid apparent motions of the brightness modulation along the background-mesh strands and the timeslice patterns in Figs. 4.9–4.11 strongly suggest wave interference as the major acoustic patterning agent. The acoustic piston studies listed above indeed rely on extensive spatial averaging to identify collapsing granules and mesoscale convergence as sites of enhanced acoustic wave excitation. Apparently, direct one-to-one mapping of individual pistons to resulting wave trains is made impossible by the ubiquitous wave spreading and interference.

**Low-frequency modulation.** The three-minute acoustic oscillation appears as modulation of the background mesh pattern seen in the reversed-greyscale panels in Fig. 4.5 and as columnar structures in the compressed timeslices in Fig. 4.11. This background pattern corresponds to the pronounced low-frequency modulation peak in the spatially-averaged power spectra in Fig. 4.12 and Fig. 4.23. It is likely to be a complex mixture of granular overshoot dynamics, internal gravity waves, and the low-frequency tail of acoustic interference patterns as those evident in the photospheric five-minute Doppler timeslice in Fig. 4.10. However, on the basis of the well-defined negative-phase signatures in Figs. 4.18 and 4.24, we believe that internal gravity waves are the principal constituent and that the mesh pattern primarily portrays their spatio-temporal interference. Further analysis adding the October 14 white light sequence confirms this view and will be reported in a future paper.

**Internetwork grains.** The physics of spectral  $K_{2V}$  grain formation has been explained by CS1997 but the spatial patterns in which grains appear are not directly amenable to such one-dimensional simulation. The latter ascertained that acoustic three-minute waves are the principal grain-causing ingredient, but our results suggest that an important additional contribution comes from the slowly-varying background mesh which we attribute to internal gravity waves. The dominance of the two corresponding power peaks in Figs. 4.12–4.13, the well-defined phase relations in Fig. 4.18, and the consistent grain-to-mesh superposition observed in movies and shown by Fig. 4.11 suggest that these two constituents together dominate internetwork grain occurrence. Thus, we conclude once again that internetwork grain patterns are set primarily by wave interference with the brightest grains resulting from constructive additions (e.g., Rutten & Uitenbroek 1991; von Uexküll & Kneer 1995; Judge et al. 2001), but we now add the gravity-wave background as extra occurrence agent.

Neither the acoustic-wave nor the gravity-wave interference patterns should be regarded as pistons, but rather as modulations that combine to define grain appearance. The combining explains the grain-mesh correlation, the apparent travel along mesh strands seen in the TRACE movies, and the frequent appearance of grains in close pairs and clusters outlining the mesh pattern. Note that the combining is nonsinusoidal through the nonlinear temperature sensitivity of the Planck function in the ultraviolet and the onset of wave steepening at these heights.

The actual pistons are to be sought in collapsing, exploding, and/or overshooting granules, or other convective generators of acoustic events and gravity-wave emission. As noted above, such searches are effectively hampered by the ubiquitous interference of the resulting waves. Acoustic waves preferentially propagate straight up but gravity waves propagate downward and spread under large angles with the vertical (Mihalas & Toomre 1981, 1982).

As shown in Sect. 4.4.3, the internetwork grains also sense higher-up Dopplershifts when observed in optically thick lines such as H & K (Figs. 4.21–4.22). The ultraviolet continua provide a cleaner picture, but we should note that the time-dependent spectral asymmetry introduced by  $H_3$  Dopplershifts to  $H_{2V}$  grain evolution did provide a suitable yardstick to gauge CS1997 simulation success.

**Network waves.** The modulation spectra in Fig. 4.12 and the modulation maps in Fig. 4.14 once again confirm that network harbours low-frequency rather than high-frequency motions.

The lower panels of Figs. 4.18–4.19 show no distinctive network properties as those seen higher up (Fig. 4.21). Note that observed wave amplitudes may also be reduced by phase mixing between different fluxtubes within a cluster making up a network patch; Fourier studies of single-element flashers may provide a tactic to isolate fluxtube wave modes.

At low frequencies there is no sign of distinctive peaks in the network power spectra in Figs. 4.18–4.19 as the one at 2.5 mHz in the  $H_3$  Dopplershift spectrum in Fig. 6 of Paper I, which was taken as significant and attributed to kink-wave cutoff by Hasan & Kalkofen (1999). Such peaks are absent in the fourth panel of Fig. 4.21 which is produced from the same data with somewhat different averaging and smoothing choices. Our TRACE data provide far better statistics, so that we conclude that specific network modulation peaks that might suggest specific fluxtube wave modes have not really been detected so far.

On the other hand, the ubiquitous presence of internal gravity waves indicated by the low-frequency power and phase-difference behaviour in Figs. 4.18, 4.23–4.24 and the coupling to fluxtube modes suggested by the low-frequency peak equality in Fig. 4.21 may signify the importance of fluxtube interaction with internal gravity waves. The lack of coherence between  $H_3$  and  $Ca\ I\ 4226.7\ \text{\AA}$  Dopplershifts in network led to the conclusion in Paper I that the slow network modulation is not correlated with underlying photospheric disturbances. A similar lack of  $V-V$  coherence is seen in the fourth panel of Fig. 4.21. However, the  $I-I$  comparison in the second panel has low-frequency network peaks for both signals, with larger coherence between them. The absence of a comparable Dopplershift connection may be due to the smallness of gravity-wave velocity perturbations compared to brightness perturbations.

Alternative explanations of the large low-frequency modulation in network are (i) – slow footpoint motions as suggested by Kneer & von Uexküll (1985, 1986), and (ii) – that the canopies spreading out from fluxtubes funnel gravity waves down as suggested by Deubner & Fleck (1990), but their interpretation of phase differences between the  $Ca\ II$  infrared lines suffers from non-trivial response characteristics of these lines (Shine & Linsky 1974; Rutten & Uitenbroek 1991; Skartlien et al. 1994). As noted above, alternative explanations for the slow  $Ca\ II\ H_3$  Doppler modulation in network are also such slow footpoint motions, or mottle flow changes as observed in  $C\ IV$ . The latter ones would have to also affect deeper fluxtube parts to cause the low-frequency brightness modulation enhancements in Fig. 4.12.

**Intermediate zones.** Two unexpected findings are the wide zones of intermediate-brightness pixels between network and “true” internetwork in Fig. 4.4 and the appearance of mottle-like structures surrounding network in low-frequency  $C\ IV$  modulation maps (Fig. 4.14). In older  $Ca\ II\ K$  filtergram sequences we have also noted wide zones of somewhat enhanced emission around network, but at the time suspected atmospheric seeing and telescopic stray-light as main cause. The  $C\ IV$  modulation maps indicate that these zones are low-lying magnetic canopies rather like the fibrils that fan out from network on  $H\alpha$  movies, as discussed in Sect. 4.4.2. These zones may be brighter in ultraviolet continua due to smaller opacity. There may also be a time-averaged brightness enhancement from a larger density of single-fluxtube magnetic flashers, or there may be more wave dissipation in the network neighbourhood.

**Network modulation aureoles.** The same zones appear as enhanced three-minute modulation aureoles in the fourth column of Fig. 4.14. Hindman & Brown (1998) proposed that

the absence of brightness modulation aureoles in their photospheric MDI data implies incompressible waves, and that the Ca II K brightness on the image sequences of Braun et al. (1992) was contaminated by Dopplershifts. Such contamination is indeed illustrated by Figs. 4.21–4.22, but the aureoles in our TRACE continuum brightness data sample intrinsic brightness modulation resulting from temperature and/or opacity variations, not Dopplershifts. However, even the decidedly acoustic waves that make up Ca II K<sub>2V</sub> grains quickly lose their brightness signature with height, whereas their Doppler signature persists (e.g., Cram 1978b; Carlsson et al. 1997; Doyle et al. 1999). Intensity is formed with much more complexity than Dopplershift (in which the last particle-photon interaction does the coding) in any non-LTE situation; we note once more that the ultraviolet continua are affected by scattering similar to two-level-atom resonance scattering. Thus, non-existence of brightness aureoles would not prove wave incompressibility. The slight but definitely present brightness-modulation aureoles in (Figs. 4.14–4.16) point to some compressibility. We suspect that they are basically acoustic.

## 4.7 Conclusions

We have used ultraviolet image sequences from TRACE to provide a detailed view of quiet-Sun brightness oscillations in the upper photosphere and low chromosphere. The view is made comprehensive through combining space-time and Fourier representations of various sorts and through comparison with the well-modelled spectral behaviour of Ca II H. The view is also well-defined because the ultraviolet passbands yield a simpler picture than the Dopplershift-sensitive Ca II H core and are not too sensitive to magnetic canopy variations, and because TRACE’s image sequences co-align precisely, do not suffer from seeing, and provide excellent statistics by combining large field with long duration.

A major motivation for this study was to diagnose high-frequency waves (well above  $f = 10$  mHz) that might heat the internetwork and network chromospheres. We have not found those, but instead have detected:

- well-defined acoustic phase-difference properties between different passbands including signatures of wave steepening (Figs. 4.18–4.19);
- phase-difference contrast between the  $p$ -mode and pseudo-mode ridges and the interridges in two-dimensional  $(k_h, f)$  phase-difference spectra (Fig. 4.24);
- strong evidence for ubiquitous internal gravity waves (Figs. 4.18 and 4.24);
- a mesh background pattern to the three-minute oscillation, which we attribute primarily to gravity-wave interference (Figs. 4.5, 4.11). The spatio-temporal appearance of internetwork grains is dominated by constructive interference between the acoustic and gravity wave patterns (Fig. 4.11);
- three-minute brightness modulation aureoles around network (Figs. 4.14–4.16);
- narrower modulation shadows around network – but only when normalised by the mean brightness (Fig. 4.17);
- frequent presence of “persistent flashers”, network-like features “on the loose” that presumably have magnetic anchoring and seem to represent isolated fluxtubes (Fig. 4.9);

- wide zones of “intermediate” pixels between network and internetwork that have higher time-averaged brightness than the internetwork “cell” centers (Fig. 4.4). They contain more flashers and correspond closely to the mottle-like extensions seen in low-frequency C IV modulation which presumably delineate low-canopy topology (Fig. 4.14).

These findings define obvious desires for further study. Some issues, such as the properties and nature of power aureoles and the effects of canopy geometry, will gain from sampling more solar scenes in similar fashion but with variety in the degree of activity. The role of granular dynamics in setting the acoustic oscillation and the background mesh patterns may be studied through combination with photospheric imaging and Doppler mapping, by TRACE and MDI or with ground-based telescopes at higher angular resolution. The persistent flashers may be identified and studied using high-resolution magnetograms. The phase relationships portrayed here provide a valuable testbed for numerical simulation of the chromospheric three-minute oscillation. Internal gravity waves will be explored in a future paper using the October 14 white light data. Finally, simultaneous passband sampling as envisaged for the *Solar Diagnostics Observatory* may push the phase detectability limit to higher frequencies than reached here.

*Acknowledgements.* We are indebted to T.J. Bogdan, B. Fleck, P.G. Judge, O.V. Khomenko, R.I. Kostik and N.G. Shchukina for comments. J.M. Krijger’s research is funded by The Netherlands Organization for Scientific Research (NWO). The TRACE sequences were taken as part of SOHO Joint Observing Program JOP72 proposed and led by P.G. Judge. J.M. Krijger and R.J. Rutten thank the Leids Kerkhoven–Bosscha Fonds for travel support and the Lockheed-Martin Solar and Astrophysics Laboratory at Palo Alto, the High Altitude Observatory at Boulder, the Jurusan Astronomi and Bosscha Observatory of the Institute of Technology Bandung, and their colleagues at these institutions for hospitality. The Utrecht–Naples collaboration is part of the European Solar Magnetometry Network supported by the European Commission under contract ERBFMRXCT980190. B.W. Lites acknowledges partial support from NASA Grant W-19.328. Careful reading by referee Dr. W. Curdt improved the paper.

# Chapter 5

## Dynamics of the solar chromosphere IV. Evidence for atmospheric gravity waves from TRACE

**Abstract.** We analyze oscillations in the solar atmosphere using simultaneous ultraviolet and white-light image sequences from the *Transition Region and Coronal Explorer* (TRACE), concentrating on the slowly-varying brightness pattern that forms the internetwork background in ultraviolet images and groundbased Ca II H & K filtergrams. Time slices and spatial time-delay correlations show that it is not simply reversed granulation. Fourier analysis indicates that it consists of atmospheric gravity waves. The better-known chromospheric three-minute oscillation (acoustic waves turning into weak shocks at the heights sampled by ultraviolet continua) is superimposed on the gravity-wave interference pattern, which acts as internetwork grain co-localiser. We suggest that the gravity-wave background reaches maximum amplitude in areas with high magnetic canopies.

## 5.1 Introduction

This paper addresses oscillations of the quiet solar atmosphere using image sequences taken with the *Transition Region and Coronal Explorer* (TRACE). It is a sequel to the third paper in this series by Krijger et al. (2001, henceforth Paper III), which concentrated on three-minute and higher-frequency oscillations in the low chromosphere using ultraviolet image sequences taken with TRACE on May 12 and October 14 1998. In the present paper we combine the October 14 ultraviolet data with the simultaneous white-light sequence taken by TRACE to investigate relations between low-frequency modulations in the quiet photosphere and low chromosphere.

In particular, we try to establish whether or how the low-frequency modulations observed in the ultraviolet image sequences hang together with the photospheric granulation and with granular overshoot in the form of “reverse granulation”. Our conclusion is that the low-chromosphere low-frequency modulation consists primarily of interference patterns of internal gravity waves. At the suggestion of D. Banerjee we call these “atmospheric gravity waves” because we deem it unlikely that they represent the internally-excited global  $g$ -modes that constitute the elusive holy grail for various instruments on SOHO.

The general context of quiet-Sun oscillations was reviewed extensively in Paper III and is therefore not given here, but we briefly summarize the literature on atmospheric gravity waves. On the theoretical side, the early work of e.g., Whitaker (1963), Lighthill (1967), Stein (1967) and Schmieder (1977) culminated in the comprehensive analysis of Mihalas & Toomre (1981, 1982). The upshot is that gravity waves should be copiously excited by convective overshoot and should be abundantly present in the upper photosphere and low chromosphere up to their breaking height. However, their detection is not easy because they combine long periods with short wavelengths, comparable to and hard to disentangle from granulation. Also, since they propagate preferentially in near-horizontal directions, they produce only small radial Doppler-shifts and quickly move off a high-resolution pixel or a spectrometer slit.

Observationally, the clearest demonstration of gravity-wave presence in the middle photosphere has been given by Straus & Bonaccini (1997) using wavenumber- and frequency-resolved  $(k_h, f)$  phase-difference spectra and horizontal propagation diagrams. Before that, mid-photospheric gravity waves were similarly noted in  $(k_h, f)$  diagrams by Kneer & von Uexküll (1993) and have been suggested on the basis of various other, less direct, diagnostics by Frazier (1968), Schmieder (1976), Cram (1978a), Brown & Harrison (1980), Durrant & Nesis (1981), Staiger et al. (1984), Staiger (1987), Deubner & Fleck (1989), Bonet et al. (1991), and Komm et al. (1991).

In Paper III the ultraviolet “background mesh” pattern which covers internetwork areas was tentatively attributed to chromospheric gravity waves on the basis of downward propagation diagnosed in phase-difference  $(k_h, f)$  spectra similar to Figs. 5.8–5.9 below. Gravity wave signatures are particularly clear in the ultraviolet image sequences from TRACE because these sample intensity rather than velocity (gravity waves primarily affect temperature), sample them high up (the intensity modulation grows steeply with height), and permit two-wavelength phase-difference evaluation with small height of formation difference (about 50 km) and appropriate spatial resolution (1 arcsec). Thus, TRACE ultraviolet image sequences are “just right” to diagnose atmospheric gravity waves. The message of this paper is that they *dominate* the internetwork scene at the heights sampled by ultraviolet continua at

low temporal frequency.

We also demonstrate below that this gravity-wave background contributes constructively to the spatial occurrence pattern of higher-frequency (“three-minute”) internetwork grains. The latter have been identified as acoustic shock interference (Rutten & Uitenbroek 1991; Carlsson & Stein 1997), but their excitation remains controversial. Recent contributions debating whether internetwork magnetism controls their occurrence are given by Nindos & Zirin (1998), Lites et al. (1999), Worden et al. (1999) and Sivaraman et al. (2000), whereas acoustic flux events have been identified as source for some (but not many) of the brightest grains by Hoekzema et al. (2002). This grain pistoning issue is also reviewed in detail in Paper III, except for the last two papers.

Higher up in the solar atmosphere, in particular as sampled in ultraviolet lines with the SUMER spectrometer onboard SOHO (e.g., Wikstøl et al. 2000), the acoustic-wave penetration pattern is set by the presence or absence of low-lying magnetic canopies as evidenced by  $H\alpha$  fibrils (Rutten 2001; Judge et al. 2001; McIntosh et al. 2001; McIntosh & Judge 2001; Rosenthal et al. 2002). The last authors also find considerable reflection of acoustic waves at magnetic canopies and suggest that the resulting wave interference contributes intermittency to internetwork grain occurrence patterns.

The organization of this paper is as follows. The observations and reduction are summarized below. In Sect. 5.3 we employ different techniques to display atmospheric gravity wave behavior, namely space-time diagrams, scatter correlation diagrams, and Fourier spectra. In principle, they tell the same story; in practice, these different points of view are complementary. We discuss the results in Sect. 5.4.

## 5.2 Observations and reduction

The TRACE observations and their reduction were presented in detail in Paper III. In this paper we use only the October 14, 1998 sequences since on this date white-light image registration was added to the cyclic 1700 Å, 1600 Å and 1550 Å bandwidth selection. The field of view covered a very quiet area near disk center (Figs. 1 and 3 of Paper III). The four image sequences were carefully aligned and corrected for solar rotation, yielding four co-spatial and co-temporal “data cubes”, each consisting of a sequence of 611 images of  $512 \times 512$  px<sup>2</sup> at 0.5 arcsec/px spatial scale and covering a duration of 3.7 hours at 22 s cadence. Due to computer limitations the scatter diagrams in Figs. 5.5–5.7 are based on  $256 \times 256 \times 256$  sub-cubes of the white light and 1700 Å data.

The measured intensities were converted into brightness temperature for some displays below, on the premise that the observed intensity modulations are related to temperature fluctuations in some way or other. For  $H^-$  dominated white light the brightness temperature samples the actual temperature near the (very corrugated)  $\tau = 1$  surface. The ultraviolet continua are dominated by scattering with  $S_\nu \approx J_\nu > B_\nu$  in plane-parallel modeling (Fig. 36 of Vernazza et al. 1981), but for these the conversion corrects in first order for the non-linear response of the Planck function to temperature variations in the ultraviolet. The conversion of the uncalibrated TRACE intensity values was done by equating their mean per data cube to  $T_b = 5929$  K for the white light data and to  $T_b = 4453$  K for the 1700 Å data on the basis of the solar spectrum compilation in Vernazza et al. (1976). This conversion is not exact but

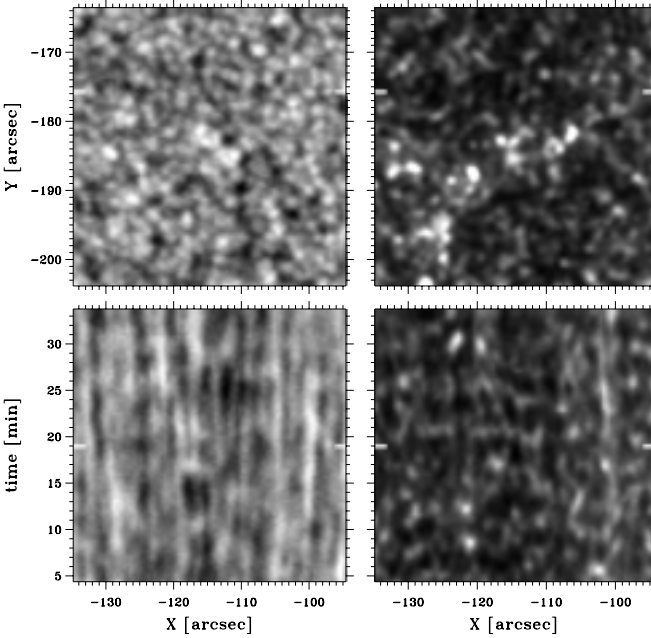


Figure 5.1: Image and time-slice samples. Left: white-light intensity. Right: co-temporal and co-spatial  $1700 \text{ \AA}$  intensity. The  $X$  and  $Y$  coordinates are angles from solar disk center on the sky, with  $Y$  directed toward the solar north pole. The images in the upper row are small cut-outs of the full  $256 \times 256 \text{ arcsec}^2$  field observed by TRACE. The time of observation is halfway the time slices in the lower row, as indicated by white markers. The slices show the temporal intensity evolution during 30 min of observation, for a horizontal cut through an internetwork area indicated by the white markers in the upper panels. It passes through weak network at the right. The greyscale is linear for all panels but has been clipped at half the actual maximum for the  $1700 \text{ \AA}$  image to suppress the brightest grains.

supplies useful modulation amplitude scales for the scatter diagrams in Figs. 5.5–5.7.

In various displays we also employ three-dimensional spatio-temporal “Fourier cone” filtering to remove all brightness modulation components with apparent horizontal speed in excess of  $6 \text{ km s}^{-1}$  (“low-pass filter”), or reversely below this value (“high-pass filter”). Such low-pass filtering selects features that are stable or move with subsonic horizontal velocities at the fastest. The high-pass filter selects modulatory phenomena above the Lamb line  $f = (1/2\pi) c_s k_h$  in the  $(k_h, f)$  diagram, i.e., the acoustic  $p$ -mode and three-minute oscillations of which the multi-wave interference patterns often show supersonic apparent motion. We first applied cosine edge tapers to avoid ringing, for the cone filter over  $v = 6 - 7 \text{ km s}^{-1}$  and for the cube edges over the first and last 12 spatial and temporal samples. The cube taper zones were removed in the subsequent analysis.

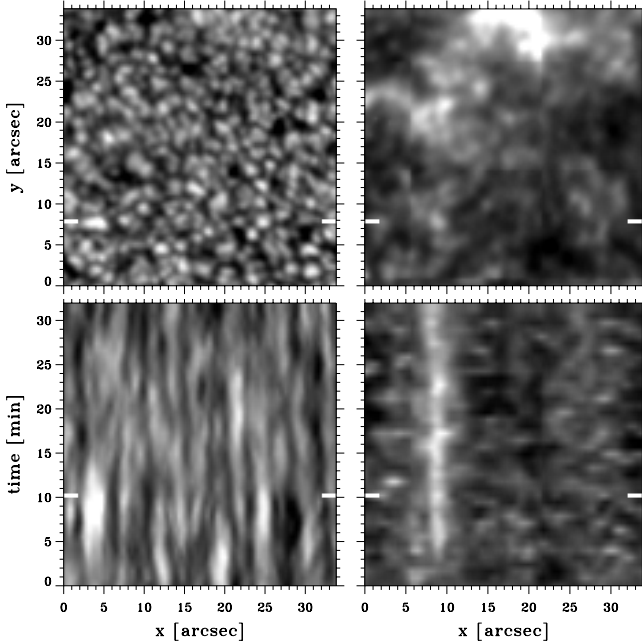


Figure 5.2: Simultaneous granulation and Ca II K imagery with the Dunn Solar Telescope from the data of Hoekzema et al. (2002), in the magnified cutout format of Fig. 5.1 and at comparable scales. Acoustic oscillations were removed from the lefthand panels through Fourier filtering. The righthand panels show intensity for 0.6 Å FWHM bandwidth centered on Ca II K<sub>2V</sub>, on a linear greyscale. The time-slice cut passes through a network grain at  $x = 9$  arcsec, with internetwork to its right.

## 5.3 Analysis and results

### 5.3.1 Space-time representations

Figure 5.1 introduces the topic of this paper. It compares the white-light scene and its evolution at left with the co-spatial and co-temporal 1700 Å scene and its evolution at right. The panels sample only very small parts of the full white-light and 1700 Å data cubes<sup>1</sup>. The image cutouts cover the lower-left corner of the full field of view shown in Fig. 3 of Paper III; the time slices cover the initial half hour of observation (skipping the tapered cube edges). The greyscale of the 1700 Å panels is logarithmic in order to bridge the large ultraviolet contrast between bright network grains and weaker internetwork grains. The  $y$ -axis cut location was selected to sample internetwork.

<sup>1</sup>These cutouts are small in order to obtain sufficient magnification. They represent a very limited rendering of the full data cubes. A better view of the dynamical ultraviolet scene is gained by inspecting the TRACE movies available at URL <http://www.astro.uu.nl/~rutten/trace1>.

The two images show grainy patterns with comparable grain sizes. The distinction between dark internetwork and bright network is obvious in the ultraviolet image at right even at 50% clipping, but the network presence produces no clear signature in the white-light granulation at left.

The white-light time slice displays granular evolution plus five-minute  $p$ -mode modulation. The ultraviolet time slice exhibits relative stability of the weak network grain near  $X = -100$  arcsec in the form of a bright streak and the dynamical nature of the internetwork in the form of three-minute internetwork grain sequences. There is no obvious correspondence between the photospheric patterns at left and the low-chromosphere patterns at right.

Ca II K<sub>2V</sub> grains are superimposed on a more extended and slower-evolving background pattern, as first pointed out by Cram & Dame (1983). In high-resolution Ca II K filtergram sequences, this background pattern appears as a spiderweb “mesh”, with the internetwork grains located on or moving along mesh strands (see the high-resolution examples in Lites et al. 1999). For reference, we add a Ca II K comparison in Fig. 5.2, using Ca II K<sub>2V</sub> filtergrams taken with the Dunn Solar Telescope by T.R. Rimmele. Comparison with Fig. 5.1 illustrates that TRACE, with 1 arcsec angular resolution, does not image solar granulation with the sharpness reached by groundbased telescopes during good seeing<sup>2</sup>, but does display larger granules reasonably well.

Comparison of the righthand columns in Figs. 5.1 and 5.2 shows that TRACE wins in sharpness from long-exposure (2 s) Ca II K filtergrams thanks to the absence of seeing in space, whereas seeing variations cause artificial sharpening of the temporal grain extents in the Ca II K time slice. The comparison shows nevertheless that the ultraviolet and Ca II K passbands portray similar solar scenes, as demonstrated by Rutten et al. (1999) from precise TRACE alignment with sharper Ca II K data. (Note that internetwork grains appear differently at different Ca II K passband widths due to sensitivity to Ca II K core Dopplershifts; see Paper III for detailed discussion of similarities and differences between these diagnostics).

In their spectral analyses of the Ca II H & K wings Evans & Catalano (1972) and Suemoto et al. (1987, 1990) have suggested that the Ca II K background pattern primarily reflects “reversed granulation”, the inverted pattern of bright lanes and dark granules that appears about 150 km above white-light continuum formation. However, spectrometry using weaker lines formed in the middle photosphere has generally led to the conclusion that the granulation pattern does survive fairly high in radial velocity, but is replaced in intensity by something else than just reversed granulation above  $h \approx 300$  km (e.g., Deubner 1988; Balthasar et al. 1990; Kucera et al. 1995; Espagnet et al. 1995; Hanslmeier et al. 2000). Our comparisons of TRACE white-light and ultraviolet images suggest a similar conclusion. All our displays below are designed to demonstrate that (i) – the internetwork ultraviolet brightness pattern is not directly or inversely coupled to granulation, and that (ii) – the low-frequency pattern properties are consistent with gravity wave behavior.

Figure 5.3 shows the same data as in Fig. 5.1 but after conversion into brightness temperature and Fourier filtering and with modified greyscaling. In the first column (white light) low-pass filtering as described in Sect. 5.2 has removed the photospheric five-minute oscillations.

<sup>2</sup>The exposure time was 200 ms, still appreciably longer than the seeing freezing time of about 10 ms. Much sharper granulation images result from 1 ms exposures with image restoration (granulation movies at URL <http://dot.astro.uu.nl>).

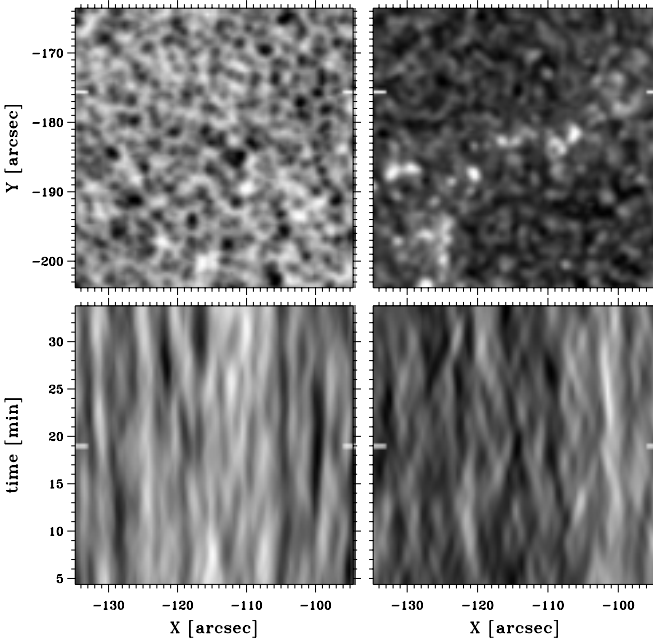


Figure 5.3: Image and time-slice samples as in Fig. 5.1 but low-pass filtered (signals with horizontal propagation below  $6 \text{ km s}^{-1}$  only) and plotting brightness temperature instead of intensity. Left: white-light brightness temperature on an inverted scale. Right: logarithm of the  $1700 \text{ \AA}$  brightness temperature.

tion and emphasizes granular evolution patterns. In addition, the greyscale is sign-reversed in order to show what reversed granulation should look like. The resulting mesh pattern in the reversed image illustrates topological difference between granules and intergranular lanes. The corresponding slice shows intergranular lanes as bright streaks with lifetimes up to 15 minutes.

In the second column ( $1700 \text{ \AA}$ ) the filtering has removed the chromospheric three-minute oscillation and emphasizes the slower background evolution next to the relatively stable network. The internetwork background streaks are shorter than the intergranular ones and show larger horizontal displacements (tilts). There is no obvious correspondence between reversed granulation at left and low-frequency internetwork modulation at right.

Figure 5.4 shows the same data once again in different manner. The lefthand white-light panels now display non-reversed brightness temperature. The righthand ultraviolet panels show the inverse of the  $1700 \text{ \AA}$  intensity. Such display reduces the visual impact of both the internetwork and the network grains (black) and emphasizes the amplitude extremes of the underlying background modulation with less contamination from other phenomena. There is again no obvious correspondence between left and right.

The conclusion from these space-time samples is that the internetwork ultraviolet scene

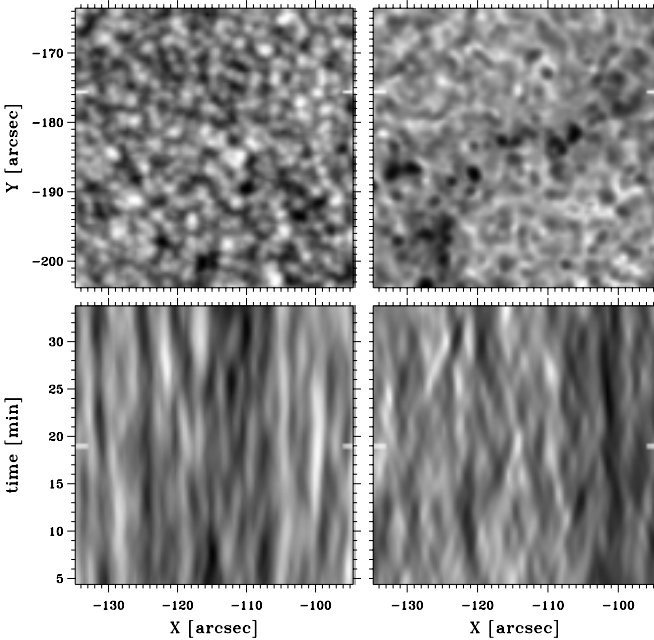


Figure 5.4: Fourier-filtered image and time-slice samples as in Fig. 5.3 but in reverse presentation. Left: white-light brightness temperature. Right: inverse of the 1700 Å intensity.

seems to have little relation to the white-light scene.

### 5.3.2 Time-delay scatter representations

Figures 5.5–5.7 compare white light (WL) and 1700 Å (UV) images in the form of pixel-by-pixel correlation plots in a format developed by Strous (1994). Each scatter diagram is measured from the lower-left  $256 \times 256$  px<sup>2</sup> TRACE subfield after removal of the 12-px edge taper zones, image conversion into brightness temperature, and  $3 \times 3$  px<sup>2</sup> ( $1.5 \times 1.5$  arcsec<sup>2</sup>) boxcar smoothing. The latter serves to suppress noise, cosmic ray hits, and pointing jitter. Similar plots without spatial smoothing show the same trends, but noisier.

For each pixel in the subfield, the brightness temperature at one moment in the one type of image (say WL) is taken as  $x$  quantity, its value at another (later) moment in the other type of image (say UV) as  $y$  quantity. Such pixel comparisons are made for 50 consecutive images of each type in order to obtain high statistics. All pairwise samples together define a scatter plot with 2.7 million comparisons. Plot saturation is avoided by plotting sample density contours instead of individual pixel-by-pixel samples.

The WL–WL comparison in the first column of Fig. 5.5 supplies a good start-off example to illustrate the format. Brightness distribution curves are added in the top panel. They are

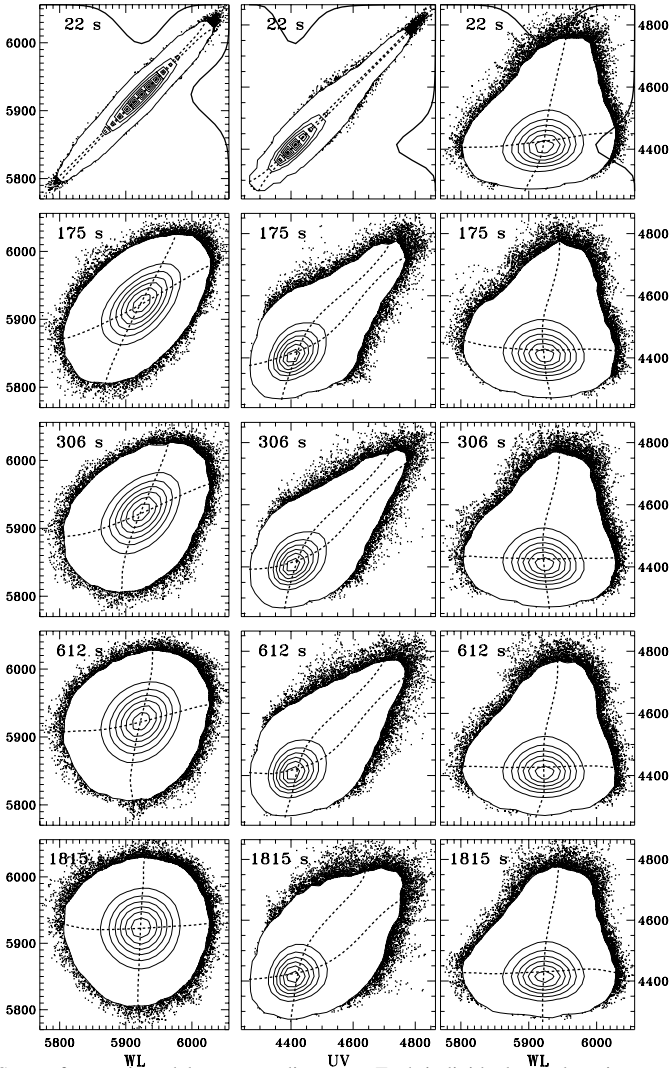


Figure 5.5: Strous-format time-delay scatter diagrams. Each individual sample point specifies  $(x, y, t)$  brightness temperature (horizontal) and time-delayed  $(x, y, t + \Delta t)$  brightness temperature (vertical) for one pixel  $(x, y)$ . The crowded central parts are plotted as sample density contours to avoid plot saturation (there are 2.7 million samples per plot). First column: time-delayed white-light brightness temperature  $WL(t + \Delta t)$  against  $WL(t)$ . Second column: time-delayed  $1700 \text{ \AA}$  brightness temperature  $UV(t + \Delta t)$  against  $WL(t)$ . Third column:  $UV(t + \Delta t)$  against  $WL(t)$ . The lefthand  $y$ -axis scale holds for the first column, the righthand one for the second and third columns. The time delays  $\Delta t$  are specified in each panel and increase from top to bottom. The solid curves in the top panels show the occurrence distributions of the quantities plotted along  $x$  and  $y$  on inverted normalized scales. The dashed curves show the first moments of the sample density distributions per  $x$  and  $y$  bin, i.e., the locations of the centers of gravity along  $x$  and  $y$  cuts through the contour “mountains”.

virtually the same for the other panels and also along  $x$  and  $y$  in this auto-correlation sequence. Their halfwidth is only about 100 K or a few percent of the intensity (the conversion is linear for white light), illustrating that TRACE does a poor job at resolving the full granulation contrast.

From the top down, the column panels are for increasing time delay between the two pixel samplings. The first panel shows very high pattern correlation; the final panel ( $\Delta t = 30$  min) shows absence of pattern correlation in the form of mutually perpendicular first-moment curves. They become diagonal for 100% correlation, anti-diagonal for 100% anticorrelation, and perpendicular in the absence of any correlation between the quantities plotted along  $x$  and  $y$ . Since the photospheric granulation has a nearly symmetrical  $T_b$  distribution, the sample contours form a nearly round bull's-eye pattern in the bottom panel. The sequence illustrates that granulation largely loses its pattern identity over ten minutes, completely in half an hour (the  $1/e$  autocorrelation time measured by Bahng & Schwarzschild 1961 from Stratoscope movies is 6.3 min; we find 4.7 min from our TRACE sequence).

The UV–UV autocorrelation sequence in the second column illustrates the two-component dichotomy between chromospheric network and internetwork. The bright distribution tail made up by network grains persists over long delays, whereas the darker internetwork (lower-left contour mountain) shows faster pattern change.

The UV–WL cross-correlation sequence in the third column shows some persistent bright-bright correlation due to network, slight anticorrelation for low WL at  $\Delta t = 3$  min, and subsequent lack of persistent correlation at low UV brightness.

The UV–WL cross-correlation is decomposed in constituents in Figure 5.6 by using selective data subsets. All three columns are limited to internetwork areas only, using a rather stringent mask derived and discussed in Paper III which labels only a third of the area as internetwork. The corresponding reduction in sampling statistics was offset by extending the pixel-by-pixel sampling to 120 consecutive image pairs per comparison. (In all scatter diagrams the outer contour lies at 100 samples per bin with 25 bins per axis. Note that the UV axis range differs between Fig. 5.5 and Figs. 5.6–5.7. We also remind the reader that the bound-free transitions which dominate in the formation of the UV radiation field suffer much resonance scattering, so that the observed brightness temperature modulation is likely to underestimate the actual temperature modulation even when the ionization equilibrium keeps up.)

The first column of Fig. 5.6 repeats the comparisons in the third column of Fig. 5.5 for internetwork only. The ultraviolet brightness temperature range diminishes correspondingly. The initial slight bright-bright correlation reverts soon into a slight but significant anticorrelation which persists during five to ten minutes.

The second and third column display the same internetwork data after  $6 \text{ km s}^{-1}$  Fourier cone filtering as described in Sect. 5.2. “Low pass” again implies removal of all acoustic oscillations; “high pass” removal of all slower components including the temporally averaged pattern. Low-pass WL filtering selects granulation. Low-pass UV filtering combined with mask selection of the inner internetwork area isolates the internetwork background pattern (cf. Figs. 5.3–5.4). High-pass UV filtering combined with the mask isolates the acoustic component of the brightness temperature variations.

The second column of Fig. 5.6 shows a delay sequence for low-pass UV against low-pass WL. The removal of the three-minute oscillation reduces the UV modulation amplitude, but

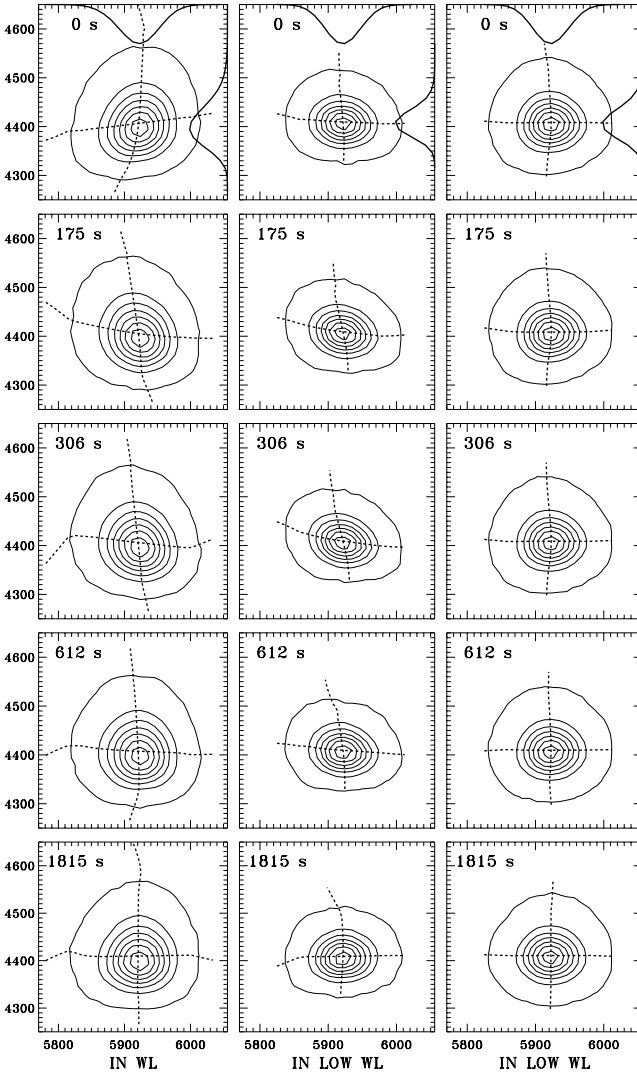


Figure 5.6: Time-delay scatter diagrams for internetwork (IN) areas only, in the format of Fig. 5.5 but dropping the outer sample clouds in order to limit plot file size. First column: unfiltered UV against unfiltered WL. Second column: low-pass UV against low-pass WL. Third column: high-pass UV against low-pass WL. The high-pass UV modulation ranges over  $[-170, +270$  K]; the mean UV internetwork value ( $T_b = 4418$  K) was added to shift the  $y$ -axis scale to the temperature scale of the other columns.

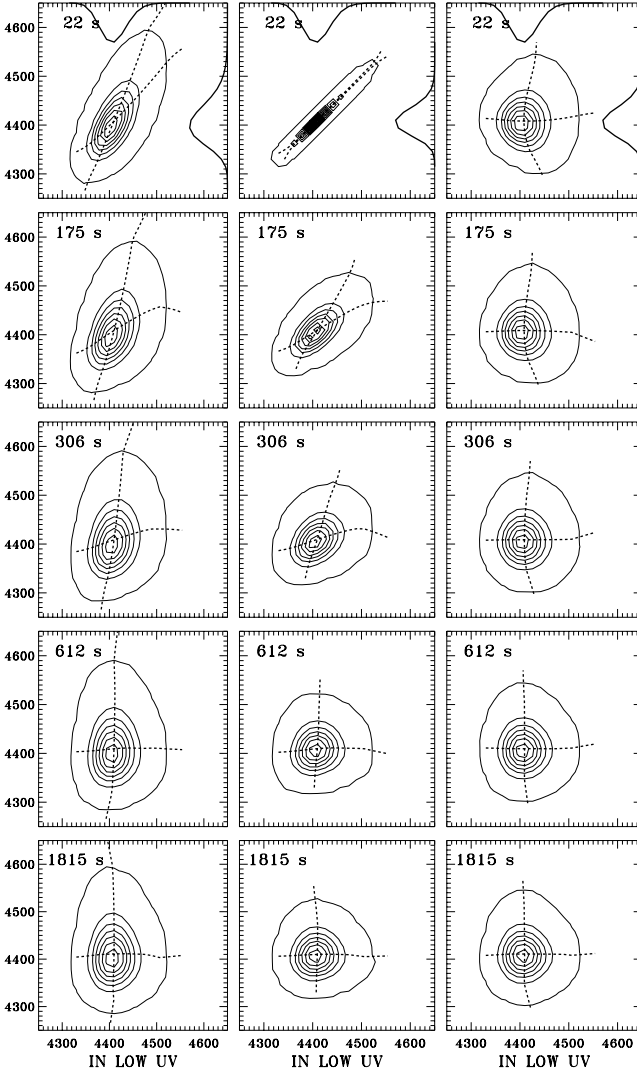


Figure 5.7: Time-delay scatter diagrams for internetwork (IN) areas only, in the format of Fig. 5.6. First column: unfiltered UV against low-pass UV. Second column: low-pass UV against low-pass UV. Third column: high-pass UV against low-pass UV, with the mean UV internetwork value added to the high-pass UV modulation for axis compatibility.

not by a large factor. The sequence shows that the slight anticorrelation in the first column is set by the slow components, namely a tendency for bright UV background to be located above intergranular lanes at delays up to 10 min. However, this anticorrelation is rather weak. Most of the UV background pattern is *not* “reversed granulation” because the anticorrelation should be much more pronounced if it were. Also, the observed anticorrelation increases initially with the sampling time delay. It reaches a maximum at  $\Delta t \approx 5$  min and survives even longer.

Note also that the top panel, at zero time delay, does not share in the slight bright-bright correlation seen in the top panel of the first column. The latter must be due to high-pass WL high-pass UV correlation from evanescent acoustic oscillations.

The third column of Fig. 5.6 shows a scatter diagram sequence for high-pass UV against low-pass WL, shifted over the mean UV internetwork brightness temperature for axis compatibility. Diagonal correlation would imply that internetwork grains favor bright granules underneath, anticorrelation that internetwork grains favor intergranular lanes underneath. The sequence shows a tiny, almost imperceptible, initial preference for the latter combination. A test comparison without spatial boxcar smoothing gave the same result, only noisier.

Thus, at the TRACE resolution there is no evidence for particular acoustic piston action by granules or lanes, in full agreement with the conclusion of Hoekzema et al. (2002) that there exists only a very slight (though highly significant) correlation between excessively bright internetwork grains and specific large-amplitude acoustic wave sources (“flux events”) in the underlying photosphere. However, much higher angular resolution than reached here may yield higher correlation with specific granular morphology such as the “collapsars” of Skartlien et al. (2000).

Both the slow modulation in the second column and the fast modulation in the third column have slightly asymmetric contours, indicating non-linearity in wave behavior. When plotted as intensity the scatter clouds stretch much further upwards due to the non-linear Planck function response in the ultraviolet; conversion to brightness temperature circularizes the contours considerably. The non-linear intensity response explains partially why internetwork grains appear as “superimposed” enhancements, see Foing & Bonnet (1984a) or Fig. 6 of Paper III. The remainder is likely to result from wave steepening.

Figure 5.7 completes the presentations in this section by adding time-delay scatter sequences for unfiltered UV, low-pass UV and high pass UV against low-pass UV, again only for internetwork pixels. The high initial correlation in the first column, with a roughly 2:1 slope, shows that peaks in internetwork UV brightness, i.e., internetwork grains, occur preferentially when also the slow-changing internetwork background is bright. The latter then contributes nearly half of the excess brightness temperature. This strong correlation confirms the finding of Cram & Dame (1983) that bright Ca II H<sub>2V</sub> grains are “invariably part” of a larger-scale modulation pattern. Thus, the slowly evolving background pattern and the three-minute oscillation combine constructively to produce bright internetwork grains. This summation survives over about five minutes, corresponding to the vertical streak lengths in the ultraviolet time slice in Fig. 5.3.

The second column of Fig. 5.7 shows a low-pass internetwork-only UV autocorrelation sequence and illustrates the five-minute lifetime of the low-frequency pattern at a given spatial position. (Horizontal propagation – producing tilts in the UV time slices in Figs. 5.3–5.4 when having an  $x$  component – causes loss of scatter correlation when the travel exceeds the 1.5 arcsec boxcar smoothing.)

The curved shape of the vertical moment curve in the upper panels of the third column in Fig. 5.7 shows that large three-minute excursions, both to high and to low UV brightness temperature with respect to the mean after removal of all slow variations, tend partially toward correlation with large UV background amplitude. This implies that the three-minute oscillation partially has modulatory character, gaining larger oscillation amplitude at larger background amplitude. The effect is not large.

The conclusions from this section are (i) – that the slowly-evolving internetwork UV background contributes appreciable intensity to internetwork grains arising from acoustic modulation and so acts as co-localizer in grain occurrence, and (ii) – that the background itself is not reversed granulation, having too weak an anticorrelation with the granulation brightness (and that over too large and too persistent time delay). It must indeed be something else.

### 5.3.3 Fourier representations

Figures 5.8–5.9 furnish Fourier presentations of our data in formats similar to various figures in Paper III. They serve to quantify phase relationships that contribute to the time-delay correlations in Figs. 5.5–5.7.

The  $(k_h, f)$  diagrams in Fig. 5.8 are directly comparable to Figs. 23 and 24 of Paper III but are derived from the October 14 rather than the May 12, 1998 TRACE data. The two-dimensional power and phase difference spectra resolve the ultraviolet intensity oscillations in both temporal frequency  $f$  (vertical) and spatial wavenumber  $k_h$  (horizontal) using annular averaging over the  $(k_x, k_y)$  spatial transform domain. The October 14 data contain almost no network, so that these Fourier plots are dominated by internetwork behavior. The acoustic oscillations (ridges and pseudo-ridges) were discussed at length in Sect. 4.4 of Paper III.

The emphasis here lies on the low-frequency domain. The mean temporal 1700 Å power spectrum (curve along the righthand side in the upper panel of Fig. 5.8) has a high low-frequency peak due to network and a wide tail toward higher frequency which represents the internetwork background until the acoustic power peak sets in. Spatially, the power increases toward longer wavelengths (mean power spectrum along the top). The lower panel of Fig. 5.8 shows a prominent wedge-shaped signature of negative phase propagation over a large  $k_h$  range in  $\Delta\phi(1700 - 1600)$  phase difference. It has high coherence between the 1700 and 1600 Å modulation. The wedge location, its Lamb-line delimitation, and its negative values all suggest atmospheric gravity waves as cause. The large power and coherence imply that these waves dominate the low-frequency internetwork background in the ultraviolet.

Figure 5.9 is a Fourier representation of the scatter comparisons in Figs. 5.5–5.6. The format was developed by B.W. Lites and combines spatially averaged power, coherence and phase difference spectra for two signals, with the spatial averaging split between internetwork and network pixels (upper and lower panel, respectively). Figures 18-22 of Paper III show similar diagrams derived from the May 12, 1998 ultraviolet TRACE data and for the older Ca II H spectrometry of Lites et al. (1993) which was successfully simulated by Carlsson & Stein (1997). We use the same compact display format here to Fourier-analyze modulation relations between our TRACE white light and ultraviolet data sequences. The upper panel in Fig. 5.9 does so for the internetwork pixels. The main conclusion is that the two image sequences are virtually independent in temporal Fourier properties. The coherence (top curve) is nowhere significantly above the random noise value ( $c = 0.45$ , indicated with a dash at

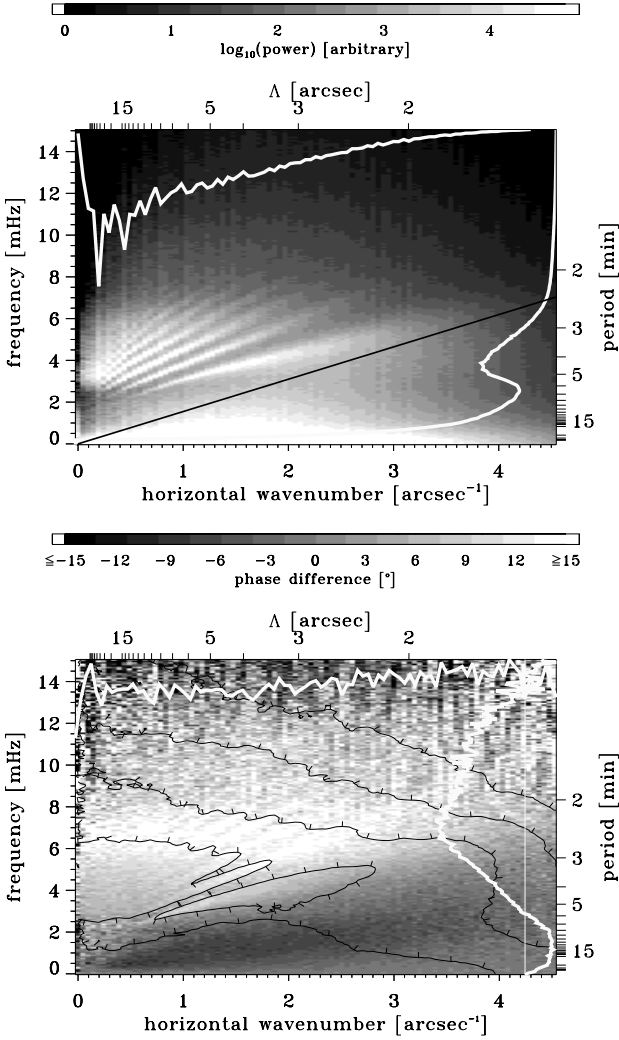


Figure 5.8: Two-dimensional Fourier spectra determined from the TRACE October 14, 1998 ultraviolet image sequences. Upper panel: 1700 Å intensity power. Lower panel:  $\Delta\phi(1700 - 1600)$  intensity phase difference. Axes: horizontal wavenumber  $k_h$  and temporal frequency  $f$ . The corresponding wavelengths and periodicities are specified along the top and the righthand sides of each panel. Greyscale: power and phase difference coding specified in the bars above the panels. The white curves along the sides are the temporal and spatial means, on linear scales in arbitrary units (with zero phase difference indicated by a thinner line at right in the lower panel). The slanted black line in the upper panel is the Lamb line  $f = (1/2\pi)c_s k_h$  for  $c_s = 7.2 \text{ km s}^{-1}$ . The contours in the lower panel specify 1700–1600 Å coherence at values  $C = 0.4, 0.6, 0.8$  and  $0.95$  with the ticks directed to lower values. The column structure in the top panel is an artefact from TRACE data compression.

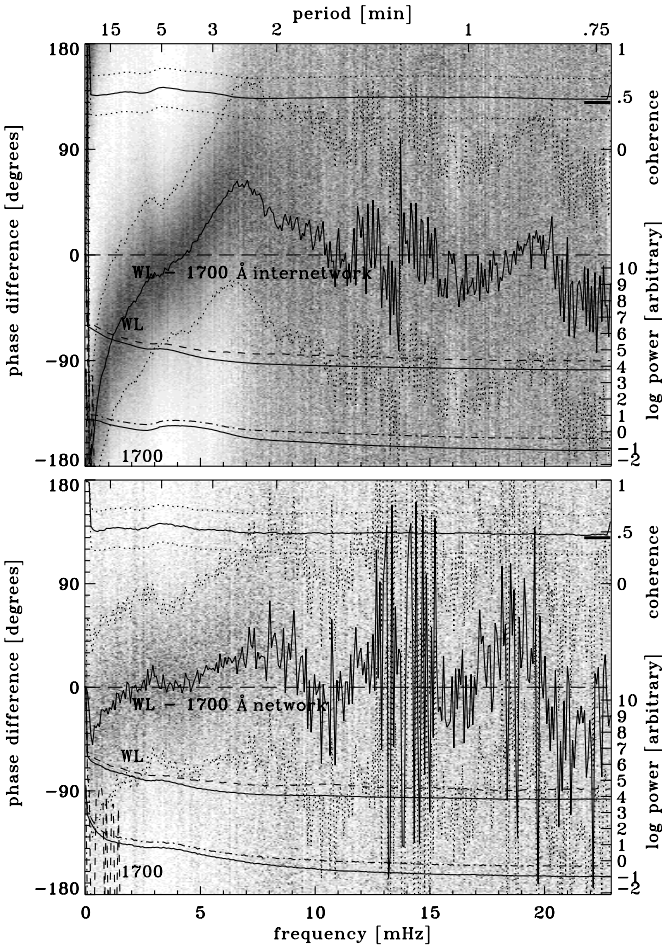


Figure 5.9: Lites-format temporal Fourier spectra for white light and 1700 Å intensity, spatially averaged over internetwork (upper panel, 39432 px) and network (lower panel, 2485 px). Abscissae: temporal frequency, corresponding periodicity specified along the top. Solid curves in the lower half of each panel: logarithmic power spectra (scale at right) with  $1\sigma$  estimates (dash-dotted and dashed curves, the lower ones drop below the panel). Solid curve near the top of each panel: coherence  $C$  between white light and 1700 Å, with  $1\sigma$  estimates (dotted; scale at right; the extra dash indicates the  $C = 0.45$  random noise value). Scatter diagram in the middle of each panel: phase differences  $\Delta\phi(\text{WL} - 1700)$ , scale at left, positive values corresponding to white light intensity leading 1700 Å intensity. Each spatial sample per frequency was weighted by the corresponding cross-power amplitude  $\sqrt{P_1 P_2}$  and then binned into a greyscale plot normalized to the same maximum darkness per frequency bin. The solid curve is the spatial vector average; the dotted  $1\sigma$  curves are determined from the weighted phase differences. Pure noise produces  $\Delta\phi$  scatter over all angles, jagged behavior of the mean  $\Delta\phi$  curve, and  $1\sigma$  spread covering  $2/3$  of the figure height.

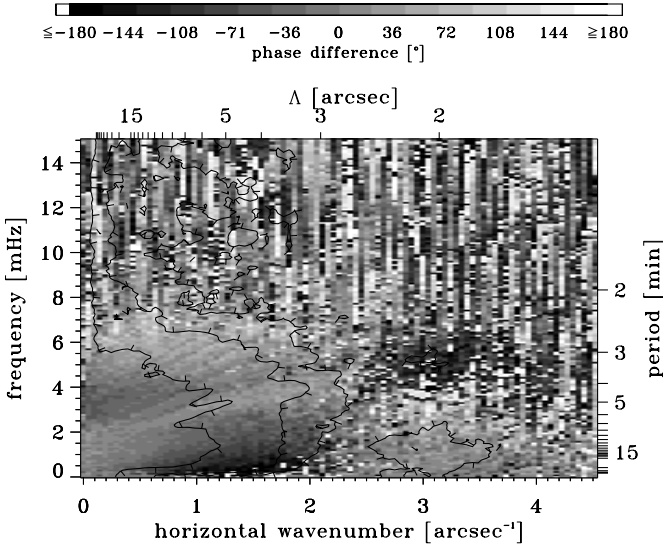


Figure 5.10: Two-dimensional  $\Delta\phi(\text{WL}-1700)$  phase difference spectrum between white light intensity and  $1700\text{ \AA}$  intensity. Format as in Fig. 5.8. The contours specify coherence levels  $C = 0.1, 0.2$  and  $0.5$ , with the ticks directed to lower values.

right). It is slightly higher in the five-minute band but very close to random in the low-frequency regime discussed here. The phase difference spread is large everywhere and reaches the random noise value already below  $f = 10$  mHz. Nevertheless, the phase difference mean shows systematic (non-jagged) behavior at low frequencies. The large negative phase difference at the start represents the Fourier counterpart of the anti-correlation in the middle column of Fig. 5.6, and pertains similarly to a minor part of the data. It has  $\Delta\phi(\text{WL}-1700) \approx -180$  deg at long periods, corresponding to long delays in Fig. 5.6.

The lower panel of Fig. 5.9 shows, though very noisily, that the network shares at most only partially in the phase difference behavior seen in the upper panel. The lack of coupling between photospheric and chromospheric network oscillations (e.g., Lites et al. 1993) is once again evident (as low low-frequency coherence).

Finally, Fig. 5.10 completes our WL-UV comparisons by showing  $\Delta\phi(\text{WL}-1700)$  phase differences in the two-dimensional  $(k_h, f)$  format of Fig. 5.8. The result is very noisy but again shows a low- $f$  low- $k$  wedge of negative phase for  $k_h < 2$  arcsec<sup>-1</sup>. It reaches much larger  $\Delta\phi$  values due to the much larger span in formation height and it has much smaller coherence, but it is qualitatively similar.

At larger  $k_h$  the low- $f$  phase differences flips from large negative to large positive values at about  $k_h = 2.5$  arcsec<sup>-1</sup>, which we attribute to wraparound in our  $\Delta\phi = [-180, +180]$  deg evaluation. This makes the positive blob around  $k_h = 3$  arcsec<sup>-1</sup> (outlined by a  $C = 0.1$  coherence contour) a continuation of the negative dark wedge and identifies the initial phase difference dip in Fig. 5.9 as due to granules. The slight signatures of reverse granulation in

Figs. 5.6 and 5.9 are therefore indeed caused at granular scales. The high- $k$  contribution is likely to become better defined in data with higher angular resolution than the 1 arcsec resolving power of TRACE.

The conclusion from this section is that Fourier analysis confirms the lack of correlation between the internetwork UV background and underlying granulation diagnosed in Sects. 5.3.1–5.3.2 through spatiotemporal analysis, and identifies the low-frequency UV variation as primarily due to atmospheric gravity waves.

## 5.4 Discussion

### 5.4.1 Terminology

Our use of the term “atmospheric gravity waves” and taking “atmosphere” to mean “low chromosphere” require comment.

First, gravity waves and convective overshoot are phenomena so closely linked that one might consider them the same. For example, realistic numerical simulations of the solar granulation such as those of Stein & Nordlund (1998) are bound to harbor both when equipped with sufficient atmosphere as in Skartlien et al. (2000). However, the two phenomena are not identical since overshoot is local whereas waves spread out. We ascribe the low-frequency internetwork mesh pattern to gravity-wave interference fed from many sources. The latter may mostly be nearby, but the non-local wave spreading is essential in producing interference.

Second, within the context of one-dimensional standard modeling as by Fontenla et al. (1993) the term “chromosphere” denotes the layers between the temperature minimum and the onset of the coronal temperature rise. Within this definition the 1700 Å continuum comes from the upper photosphere, the 1600 Å continuum from the temperature minimum, and the 1550 Å continuum from the low chromosphere (Fig. 36 in Vernazza et al. 1981). However, in all three continua the solar scene appears closely similar to what is observed in Ca II K filtergrams (Rutten et al. 1999), commonly denoted chromospheric<sup>3</sup>. In the present paper, our term “low chromosphere” simply denotes the layers sampled by ultraviolet continua<sup>4</sup>.

---

<sup>3</sup>One might argue that even wide-band Ca II K filtergrams sample the upper photosphere since the intensity-encoding thermal creation (rather than the velocity-encoding last scattering) of most of the observed photons takes place well below the standard temperature minimum. For example, the Na I D lines are not chromospheric in intensity response, i.e., not mapping a standard chromospheric temperature rise in their emergent profiles (Bruls et al. 1992). However, in the case of Ca II K the inner-wing intensity behavior is strongly influenced by chromospheric Dopplershifts (Paper III).

<sup>4</sup>Actually, we would prefer to define “chromosphere” – harking back to its color-coded eclipse origin – as the solar regime sampled by H $\alpha$ . Taking the complex mass of fibrils observed in H $\alpha$  as constituting actual “magnetic canopies”, this definition makes the chromosphere start at canopy height (which may vary widely between supergranulation cells, corresponding to H $\alpha$  difference between short local and long distant fibril connections). In this view, the present paper discusses upper-photospheric or “clapotispheric” (Rutten 1994) under-the-canopy behavior only

### 5.4.2 Gravity wave excitation

The large wedge of negative phase difference in the lower panel of Fig. 5.8 extends over  $k_h = 0.5 - 3.5 \text{ arcsec}^{-1}$ , or  $\Lambda = 2 - 10 \text{ arcsec}$  in wavelength. An initial estimate by Th. Straus (OAC, Naples) to be reported elsewhere suggests that the upper border of the wedge corresponds to the gravity-wave propagation limit set by radiative relaxation. The wedge ( $k_h, f$ ) location (larger than granules, smaller than network, below the acoustic regime), shape (delimited by the Lamb line or propagation cutoff), and its negative phase differences strongly suggest atmospheric gravity waves as cause.

We therefore interpret the internetwork background in our ultraviolet image sequence, and also the similar mesh pattern in Ca II K filtergram sequences, as dominated by atmospheric gravity waves. We so confirm the many earlier indications for gravity waves lower down in the photosphere that are listed in Sect. 5.1. Reversed granulation makes only a minor contribution, if at all, and only at granular scales as one might expect (Fig. 5.10). The slight reverse correlation at rather long time delay seen in the middle column of Fig. 5.6 may also signify enhanced gravity wave presence above intergranular lanes rather than non-wave granulation pattern reversal.

One would expect that granular upwellings hitting the overlaying radiative-equilibrium regime are a major contributor of photospheric gravity-wave emission. However, since the gravity-wave power increases somewhat with wavelength beyond granular scales, it may be that the slightly larger upwellings in the so-called meso-scale convection regime are somewhat more efficient gravity-wave emitters by being slower and less susceptible to radiative pattern smoothing. Also, since the waves spread in slanted directions from their sources and brighten steeply with height, wave interference is likely to occur and to cause low-chromosphere modulation peaks at source separation scales. Finally, bound-free scattering in the UV continua may wash out the smaller scales. Only numerical simulation can address these scale issues.

More in general it is obvious that numerical simulation of the granulation including an extended atmosphere and employing diagnostics as ours is an appropriate and promising method to shed light on atmospheric gravity-wave excitation and properties.

Although we deem it unlikely, we cannot exclude a contribution from internal global  $g$ -modes to the gravity wave signal detected here. Just as for locally excited atmospheric gravity waves, TRACE's ultraviolet brightness sampling of layers well above the granulation provides in principle a better diagnostic than visible-light brightness or Dopplershift from the granule-dominated low photosphere.

### 5.4.3 Inverse canopy mapping

Figure 5.11 extends the inverse display used in the righthand panels of Fig. 5.4 to TRACE's full field of view in these observations and to one-hour time averaging, and adds a similar Ca II  $K_{2V}$  display from the data of Hoekzema et al. (2002). As noted above, such reversed display emphasizes the deepest minima of the background modulation and de-emphasizes superimposed three-minute oscillation spikes and yet brighter network grains. The brightest reverse-display features mark locations where the uncontaminated low-frequency background modulation reaches its largest amplitude.

Each panel in Fig. 5.11 is an average of time-sequence image brightness over one hour

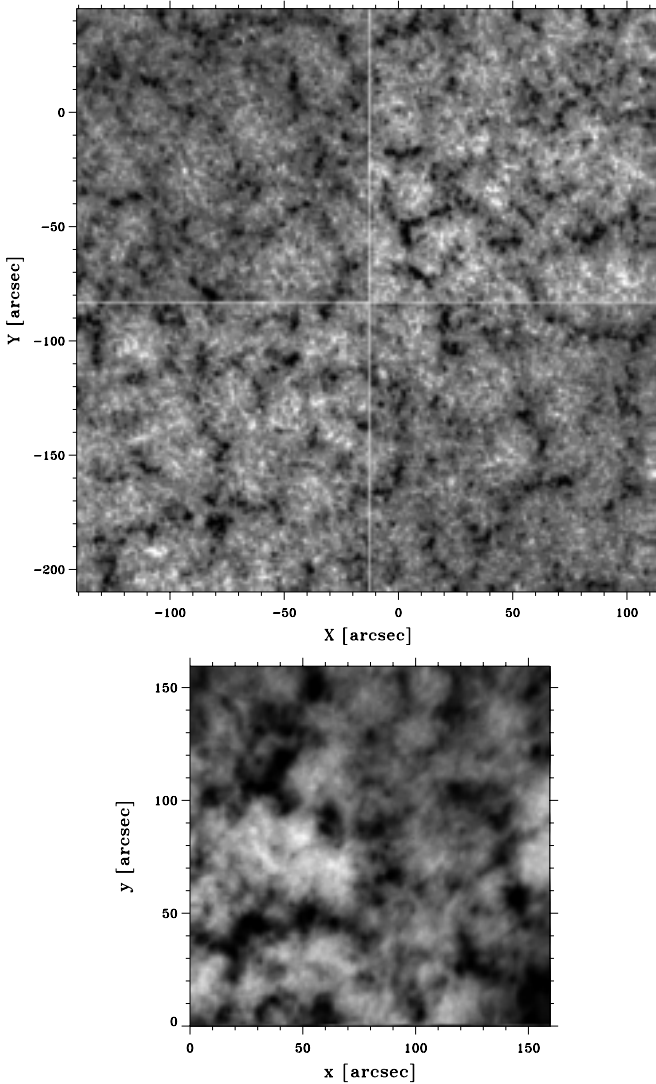


Figure 5.11: Wide-field  $1700\text{ \AA}$  and  $\text{Ca II K}_{2V}$  imaging on similar spatial scales. The data are from October 14 and September 27, 1998, respectively, and are only qualitatively comparable. Each image is a one-hour temporal brightness average displayed with reversed greyscale (inverse for  $1700\text{ \AA}$ , sign-reversed and cubed for  $\text{Ca II K}_{2V}$ ). The white lines in the upper panel mark the division of the TRACE data into four subfields. The horizontal striping near the right edge results from solar rotation correction. The relative unsharpness of the  $\text{Ca II K}_{2V}$  average results primarily from atmospheric seeing.

duration. The reversed-display patterns indicate that gravity-wave extrema tend to occur preferentially at some distance from the nearest network and that they may differ systematically between different internetwork regions. An explanation which we consider likely is that the occurrence of large extrema marks locations where the magnetic canopy<sup>5</sup> reaches larger height than elsewhere, on the assumption that gravity waves vanish where the field becomes strong enough to convert them akin to the magnetic suppression or reflection of acoustic waves at canopies reported by McIntosh et al. (2001) and Rosenthal et al. (2002).

An alternative and reversed speculation (suggested by R. Erdelyi, cf. Cadez et al. 1997; Pintér et al. 2001) is that magnetic resonant absorption enhances specific wave modes at the canopy height and that large apparent amplitude marks such resonance.

#### 5.4.4 Magnetic alternative

We interpret the ultraviolet internetwork background as a gravity-wave interference pattern, but we cannot exclude from these data that internetwork fields play a role. As noted in the introduction, the debate on the role of internetwork fields in causing and localizing internetwork grains still continues (e.g., Lites et al. 1999; Sivaraman et al. 2000). The lefthand column of Fig. 5.7 demonstrates that the low-frequency internetwork modulation is an important grain co-localizer. Advocates of magnetic grain formation may argue that this slowly varying emission pattern originates from weak fields that are swept into and collected in intergranular lanes without reaching the kilogauss field strengths of network elements, as suggested observationally by Lin & Rimmele (1999) and theoretically by the magnetoconvection simulations of Emonet & Cattaneo (2001). A further conjecture might then be that these weak-field concentrations share the strong-field network propensity to display low-frequency variations in the low chromosphere, and so make up the low-frequency intensity background in ultraviolet and Ca II K filtergrams.

We regard the absence of considerable anticorrelation between low-frequency ultraviolet brightness and intergranular lanes in Fig. 5.6 a strong argument against such a speculation. Even if the internetwork fields concentrate with meso-scale location selectivity, as they do in the simulations of Cattaneo et al. (2001) and in yet unpublished non-Boussinesq simulations by Stein and Nordlund, they still reside nearly exclusively in intergranular lanes and lane junctions, and should therefore display strong anticorrelation.

The inverse amplitude mapping in Fig. 5.11 suggests to us rather the reverse, namely that larger low-frequency UV modulation amplitude implies weaker magnetism (i.e., larger canopy height). Nevertheless, we cannot reject internetwork magnetism as an important internetwork brightness agent without measuring it.

A first test would be to correlate the weak-field background in sufficiently sensitive and reliable magnetograms with the ultraviolet or Ca II K intensity background. Preferably this should be done using quantification techniques as ours above, instead of only showing selective “example” displays. The ultimate test is to reproduce our observed power and phase

---

<sup>5</sup>The internetwork canopy may be defined as the surface where the ratio of gas pressure to magnetic pressure (plasma beta) drops through unity. In schematic fluxtube models the canopy hovers dome-like over internetwork “cell interiors”. In reality, canopies are likely to be highly warped surfaces, strongly offset by dynamical flows and with large topological variations between different internetwork areas depending on small-scale and large-scale field connectivity.

difference spectra from realistic simulations. We predict that this can be achieved through 3D simulation of granular convection, atmospheric gravity-wave propagation and ultraviolet radiation scattering without involving magnetism.

*Acknowledgements.* We are indebted to T.D. Tarbell for programming and scheduling TRACE for these observations and to T.J. Bogdan, B. Fleck, S.S. Hasan, O.V. Khomenko, R.I. Kostik, N.G. Shchukina, G. Severino, R.F. Stein and Th. Straus for inspiring discussions, some within the framework of NATO grant PST.CLG.97501, INTAS grant 00-00084 and the EC-TMR European Solar Magnetometry Network. J.M. Krijger's research was funded by The Netherlands Organization for Scientific Research (NWO). Both authors thank the Leids Kerkhoven-Bosscha Fonds for frequent travel support.

---

# Chapter 6

## Dynamic behaviour of the upper solar atmosphere:

### II. SUMER/SOHO, TRACE and VTT observations

**Abstract.** We analyze oscillations in the solar atmosphere using simultaneous observations from the SUMER spectrometer onboard SOHO, the TRACE satellite, and the groundbased VTT in different Lyman lines, UV continua and Ca II K. We compare the oscillatory patterns detected with these different diagnostics and conclude that, although the whole atmosphere exhibits oscillatory behaviour with periods between 2-8 min (longer ones being also present), there are no obvious similarities between oscillations of the lower chromosphere and lower transition region. We confirm that TRACE 1600 Å can be used as a good substitute for groundbased Ca II K. We also show that the Ly $\alpha$  construct derived from the TRACE 1216 Å passband following the method of Handy et al. (1999b) originates in the wing of Ly $\alpha$  and shows a similar morphology as the Ly $\alpha$  wing emission observed by SUMER.

## 6.1 Introduction

The dynamic structure of the solar chromosphere and its consequences on the modelling of the upper solar atmosphere are the subject of a rather controversial debate. In the interiors of the quiet sun supergranular cells (internetwork, as distinct from the network or cell boundaries) one can detect chromospheric oscillations, first seen as CaII  $K_{2v}$  grains (for a review see Rutten & Uitenbroek 1991; Krijger et al. 2001a). These grains result from dissipation of vertically-propagating acoustic weak shocks (Carlsson & Stein 1997). Chromospheric oscillations were observed from space with the HRST by Cook et al. (1996), Hoekzema et al. (1997) and more recent with the SUMER (Wilhelm et al. 1995) and CDS (Harrison et al. 1995) instruments on board the *Solar and Heliospheric Observatory* (SOHO) (Domingo et al. 1995). Results based on SUMER observations of various UV lines are summarized in Carlsson (1999) while a study of oscillations in hydrogen Lyman lines and continuum was described by Curdt & Heinzel (1998) and Heinzel & Curdt (1999). Recently, also time series of UV images from the *Transition Region and Coronal Explorer* (TRACE) (Handy et al. 1999a) were used to analyse the chromospheric oscillations and transition-region (TR) oscillations (e.g., Judge et al. 2001; Krijger et al. 2001a).

When comparing all these observations, an obvious question arises to which extent all the oscillations in different lines and continua, found in the above mentioned papers, correlate in space and time. The degree of such correlations constrains the models of propagation and dissipation of waves in the chromosphere and the transition region. For example, if acoustic shocks inside the internetwork fully dissipate to form waves visible as chromospheric grains, one should not observe any oscillations in higher atmospheric levels seen by the Lyman transitions or in other lines formed at bottom of the transition region, which is not the case. On the other hand the work of Rosenthal et al. (2002) shows that one can expect a large variety of oscillations below, inside and above the magnetic canopies and these will probably show little correlation with each other, if any.

In an initial explorative study, Curdt & Heinzel (1998) found the clear signature of oscillations in Lyman lines and continuum which motivated them to propose a joint SOHO-TRACE-GBO campaign (Joint Observing Programme JOP95) to study chromospheric and transition region oscillations in a more comprehensive way. Within JOP95, in which SUMER observed the whole Lyman series, the Lyman continuum, and inevitably some other UV lines with a 29 s cadence. TRACE was used simultaneously to obtain images in 1700 Å, 1600 Å, 1550 Å and 1216 Å channels. Ground-based observatories (GBO) on Tenerife joined the campaign, the Vacuum Tower Telescope (VTT) obtained CaII  $K_{2v}$  and H $\alpha$  narrow-band filtergrams while the Gregory Coudé Telescope (GCT) performed Stokes polarimetry of the observed quiet-Sun region (not used in this study). The SUMER part of JOP95 was successfully tested in spring 1999. The coordinated SOHO-TRACE-GBO campaign was performed during May 4–8, 1999. A schematic time table of the observations is shown in Fig. 6.1. Preliminary results were reported by Curdt et al. (1999).

Part of this work contains comparison between CaII  $K_{2v}$  grains and grains seen in TRACE UV continua (see also Rutten et al. 1999) and direct comparison between SUMER and TRACE Ly $\alpha$ . Some of the data were processed using the comprehensive Fourier diagnostics described in Krijger et al. (2001a). We also show results of wavelet analysis of selected co-temporal data sets.

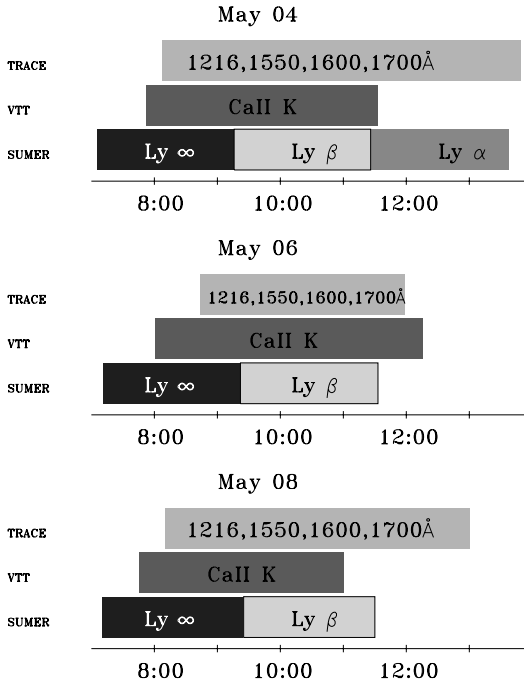


Figure 6.1: Overview of the coordinated observations taken during May 4-8, 1999 campaign. TRACE observed in the passbands centred on 1216, 1600, 1700 Å, the VTT observed Ca II K. The SUMER instrument aboard SOHO observed the higher Lyman lines and continuum, Ly $\beta$  and Ly $\alpha$ , respectively.

The paper is organized as follows. The observations and reductions are presented in the next section. In Sect. 6.3 we discuss the possibility of using the TRACE 1600 Å passband as a substitute for Ca II K. In Sect. 6.4 we compare SUMER Ly $\alpha$  and the TRACE Ly $\alpha$  construct. In Sect. 6.5 we analyse oscillations in higher Lyman lines and in the Lyman continuum. The discussion and conclusions follow in Sect. 6.6.

## 6.2 Observations and reduction

### 6.2.1 SUMER/SOHO observations

The daily observations during JOP95 of the SUMER spectrograph fell into two blocks consisting of time series in higher Lyman lines and Ly $\beta$ , respectively. We selected 2.2 Å broad spectral windows at 907 Å ( $L_{\text{cont}}$ ), 913 Å ( $L_{\infty}$ ), 915.329 Å ( $L_{15}$ ), 918.129 Å ( $L_{11}$ ), 920.963 Å ( $L_9$ ), 926.226 Å ( $L_7$ ), 930.20 Å ( $L_6$ ) for the first time series and adjacent windows at 1023.8 Å, 1026.0 Å, 1028.2 Å (covering Ly $\beta$  and the nearby O I lines) for the second time series. On

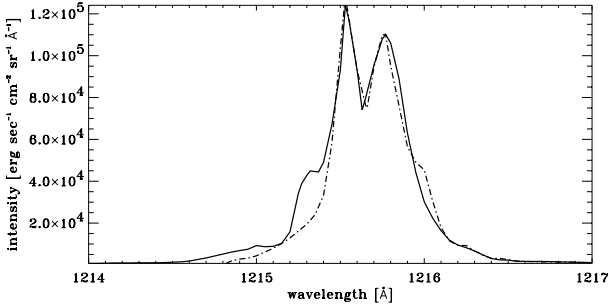


Figure 6.2: Average Ly $\alpha$  profile after correction for attenuator (full line) and SUMER Atlas profile (dashed line).

May 4 this was followed by a third time series during which Ly $\alpha$  (1210.66 Å– 1216.66 Å) was observed. The data were recorded using detector ‘B’. At the beginning of each daily observation a context map of  $80 \times 300$  arcsec was obtained in the He I 584.34 Å line and the C I continuum around 1168 Å.

The SUMER instrument was pointed near disk centre and tracked this position on the solar surface using a special, so-called half-step solar rotation compensation scheme, where steps of 0.375 arcsec were performed every 145.7 s. This tracking mode circumvents the standard SUMER compensation mode using compensation with 0.75 arcsec increments, which introduces a parasitic power peak near solar oscillation frequencies (Rybák et al. 1999; Heinzel & Curdt 1999). The cadence of 29.06 s was dictated by both the dedicated solar-rotation tracking and telemetry constraints: a multiple of the exposure time had to match the 145.7 s interval of the solar rotation compensation.

Standard procedures were employed for decompression, flat-field correction, and geometrical distortion correction of the data as furnished at URL <http://www.linmpi.mpg.de/english/projekte/sumer/text/cookbook.html>. The photon load of the detector was below the critical values above which dead-time and local gain depression errors occur.

For the Ly $\alpha$  line, we have used three spectral windows, each about 2 Å wide (50 pixels) between 1210.66 Å and 1216.66 Å. The first two cover the blue wing on the bare part of the detector, while the third one contains the central part of the line. Due to its large brightness on the disk, this part was placed on the attenuator. The attenuator edge cuts the blue part of the line core and had to be calibrated. We have determined the average and fitted it to the quiet-Sun line profile from SUMER spectral atlas (Curdt et al. 2001). Figure 6.2 shows the result. Note that both the mean Ly $\alpha$  profile from our observations and the reference profile exhibit a blue asymmetry (blue peak higher) as does the reference atlas profile. This fit delivers the attenuation coefficients for the edge pixels of the attenuator which were subsequently used to reduce the whole set of time-dependent per spatial position profiles along the SUMER slit. We have assumed that pixel 22 is already fully on the attenuator (attenuation factor 10) and that the red peak at this pixel has the intensity of the reference profile. There are two small uncertainties in the resulting profile. First, the blue asymmetry is probably not physically realistic since all higher Lyman lines exhibit the red asymmetry in their mean quiet-

Sun profiles – see the SUMER atlas or preferably the Lyman-line profiles in Warren et al. (1998). We ascribe the blue asymmetry to the attenuator modulation for which the atlas profile is not corrected. Second, small humps appear in the wings which we also attribute to attenuator modulation. These effects do not affect significantly the integrated line intensity, which is the quantity used below in our comparison with Ly  $\alpha$  imaging from TRACE.

### 6.2.2 TRACE observations

We use two different TRACE image sequences. The first sequence was taken on May 4, 1999 between 8:08–13:48 UT, the second on May 8, 1999 between 8:10–12:58 UT. Details are given in Table 6.1. Both sequences had 40 s cadence and sequentially sampled the 1700 Å, 1600 Å, 1550 Å and 1216 Å passbands. Figure 6.3 shows the pointing. Irregular jumps in pointing and the lack of temporal overlap with the VTT Ca II K and SUMER Lyman lines observing reduced the pertinent duration of the TRACE sequence of May 8 to 8:10–8:58 UT.

Both sequences were treated similarly in their reduction. Following the TRACE Analysis Guide<sup>1</sup> we subtracted the readout pedestal, but did not apply flat-field corrections or bad-pixel eliminations since none are specified for these dates. Faulty images were replaced by the averages of the preceding and subsequent images.

The sequences were aligned in a overlapping stepping scheme with cross-correlation, resulting in alignments generally accurate to a few tenths of a pixel. Sample images of the different TRACE passbands are shown in Fig. 6.4. The network appears as bright patches, corresponding to the magnetic network in the underlying photosphere (e.g., Krijger et al. 2002). Individual bright grains are visible in the internetwork. In the 1550 Å the network becomes larger and more diffuse then in the 1600 Å or 1700 Å passbands and even more so in the 1216 Å passband.

Table 6.1: TRACE observations used in this paper

date	May 04, 1999	May 08, 1999
image size [px]	256 × 640	512 × 640
$X_{\text{cen}}, Y_{\text{cen}}$ [arcsec]	99, 79	67, 21
time [UT]	08:08–13:48	08:10–08:58
cadence [s]	40.108	40.043
exposure 1700 Å [s]	2.0479	2.0479
exposure 1600 Å [s]	1.0239	1.0239
exposure 1550 Å [s]	5.7919	5.7919
exposure 1216 Å [s]	2.1538	2.1538

### 6.2.3 VTT observation

The ground-based observations used in this paper were carried out at the Vacuum Tower Telescope of the Kiepenheuer-Institut für Sonnenphysik at the Observatorio del Teide on Tenerife,

<sup>1</sup><http://www.lmsal.com/solarsoft/>

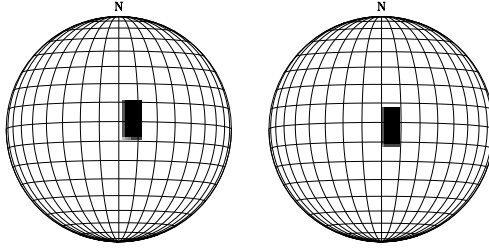


Figure 6.3: Solar location of the fields observed with TRACE on May 4, 1999 (left) and May 8, 1999 (right). The grid shows heliocentric longitude and latitude.

between May 4 and May 8, 1999. A Halle Lyot filter was used to obtain narrow-band filtergrams in the Ca K line ( $3933 \text{ \AA}$ ). The width of the filter was set to  $60 \text{ pm}$  with the bandpass centered on the Ca  $K_{2v}$  emission peak. Time sequences with a cadence of  $6.04 \text{ s}$  and duration between two and five hours were recorded on a blue-sensitive  $1024 \times 1024 \text{ pixel}^2$  CCD camera. The CCD was operated in a  $512 \times 512$  summing mode, resulting in an effective pixel size of  $38 \text{ }\mu\text{m}$ . The plate scale was determined from a calibration grid target placed in the prime focus of the telescope. The image scale of the telescope at the prime focus was measured to be  $4.55 \text{ arcsec/mm}$ , giving a filtergram pixel size of  $0.356 \times 0.356 \text{ arcsec}^2$ . The integration time was  $0.25 \text{ s}$ . A correlation tracker was used for image stabilization. The only sequence with good seeing was obtained on May 8, 1999 between 7:45–11:00 UT.

All data were corrected for dark current and offset and for intensity inhomogeneities caused by the CCD or other optics. The guiding was not perfect throughout the whole sequence; occasionally, the correlation tracker, locked on normal granulation, lost its tracking position due to moments of bad seeing. Therefore the images were aligned again. Every 100th image of a sequence was selected as a reference image, and these images were aligned first. The full sequence was then aligned with respect to the nearest reference image. This procedure produced a good alignment of the sequence, without any systematic image drift and co-registration precision of about  $0.2 \text{ pixel}$ . This post-facto alignment procedure reduced the field of view to about  $150 \times 150 \text{ arcsec}^2$  (see Fig. 6.4).

## 6.2.4 Coalignment

The SUMER spectrometry data were aligned to the TRACE images in two steps. As a first iteration for each day an average TRACE  $1600 \text{ \AA}$  image was coaligned to a SUMER context map of the C I continuum using cross-correlation. Regrettably the context map on May 4 was taken a full hour before the start of the TRACE sequences. The solar feature pattern had evolved in the meantime, but still a good alignment was possible. As a second step, the TRACE  $1600 \text{ \AA}$   $y-t$  slices taken around the assumed position of the SUMER slit inside the C I context map were correlated with the SUMER sequences in all Lyman lines, determining the best slice. Using these two steps the coalignment between TRACE and SUMER is estimated to be accurate within  $1 \text{ arcsec}$ .

On May 8 we obtained 47 min of simultaneous VTT Ca II K and TRACE observations.

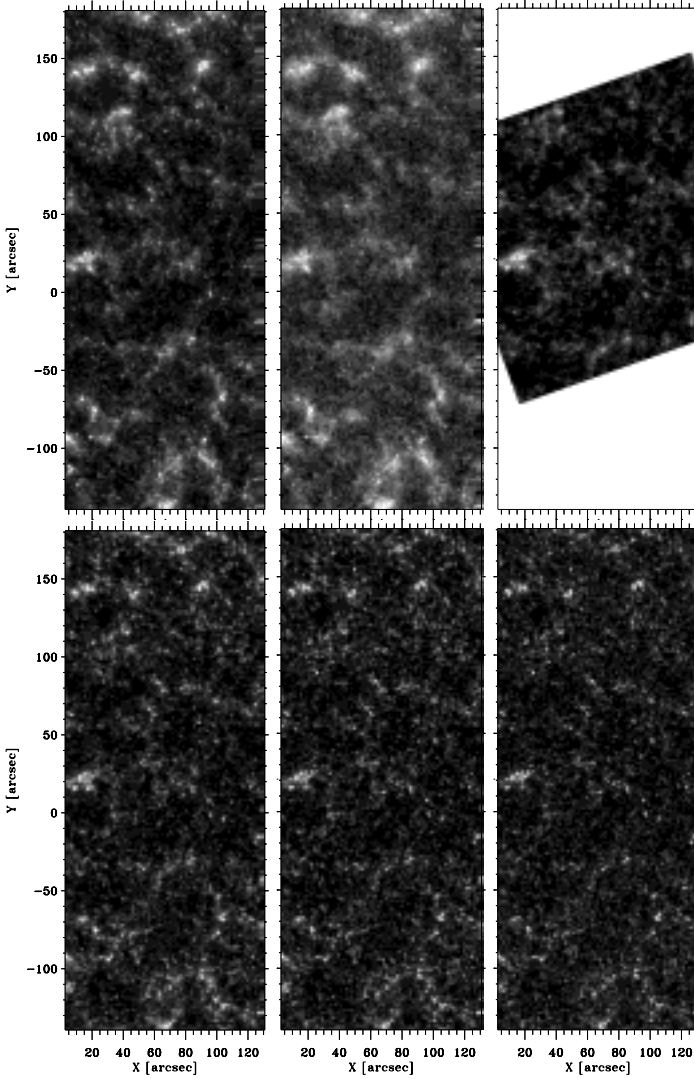


Figure 6.4: Sample images showing the same subfield taken around 08:31 UT, May 8 1999. Top row from left to right: TRACE 1216 Å, Ly $\alpha$  construct (see Sect. 6.4) and aligned VTT Ca II K. Bottom row from left to right: 1550 Å, 1600 Å, and 1700 Å. The rightside horizontal striping is due to solar rotation correction. Axes:  $X$  and  $Y$  in arcsec from disk centre.

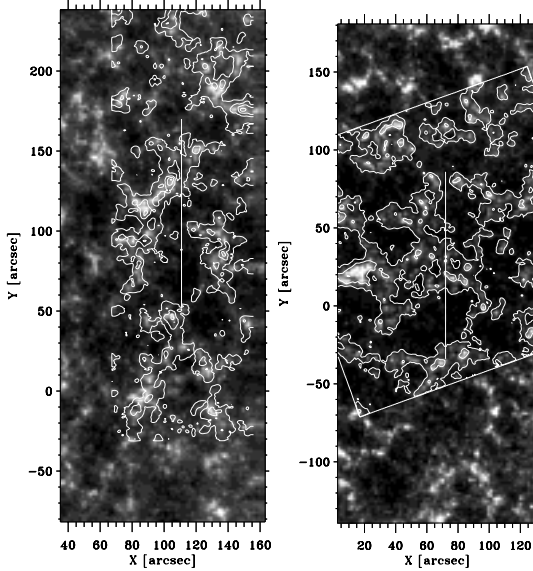


Figure 6.5: Temporal averages over one hour duration TRACE 1600 Å images with contours added respectively of C I continuum taken by SUMER for May 4, 1999 (left) and average Ca II K taken by VTT for May 8, 1999 (right). The solid vertical line indicates the SUMER slit position. Axes:  $X$  and  $Y$  in arcsec from disk centre.

After rotating and rescaling the Ca II K sequence we coaligned the different sequences by cross-correlation. The resulting alignment is accurate to within a few tenths of a pixel. The lefthand panel in Fig. 6.5 shows a temporal average over one hour duration TRACE 1600 Å image for May 4, 1999 with the contour of the SUMER C I continuum context map. The SUMER slit is shown as a solid vertical line. In the righthand panel of Fig. 6.5 the SUMER slit and the average 1600 Å image for May 8, 1999 are shown, but the contours are of the average Ca II K VTT sequence.

### 6.3 TRACE 1600 Å versus Ca II K

Multi-telescope observing campaigns involving groundbased telescopes (GBO's) are often troubled by the variations in seeing quality and the limitation to sequence durations of a few hours at best. These problems are avoided by using space telescopes, though the current solar space telescopes do not yet reach the resolution possible by GBO's. Our campaign was no exception: during three days of our observing campaign there was only one morning with reasonably good seeing for the groundbased Ca II K observations and at that moment no SUMER Ly  $\alpha$  was available (see Fig. 6.1). In order to better study the relation between Ly  $\alpha$  and Ca II K an alternative for groundbased observation was needed, however no space telescopes observe Ca II K. The overlap in TRACE and VTT observing enables us to demonstrate the close cor-

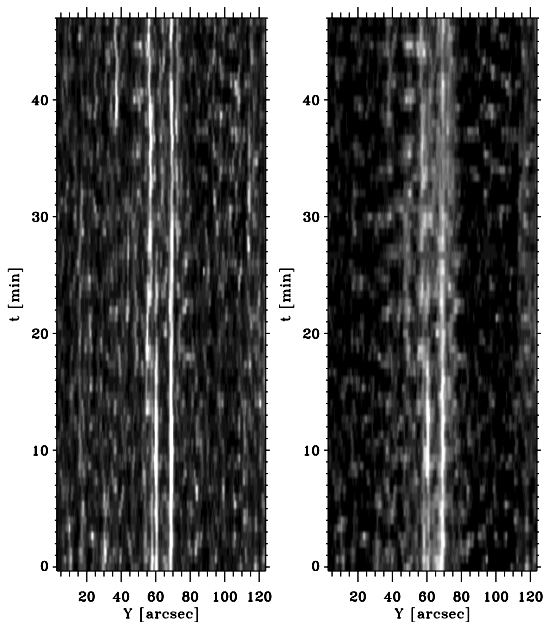


Figure 6.6: Linear intensity variation along the SUMER slit for TRACE 1600 Å (left) and VTT Ca II K (right) taken on May 8, 1999. The Ca II K is rescaled to the same TRACE cadence of 40 s. Axes:  $Y$  in arcsec from disk centre, elapsed time in minutes covering the whole duration of simultaneous observation.

response of the solar scene imaged in the UV (TRACE) and in Ca II K filtergrams, as suggested by the single-image comparison of Rutten et al. (1999). Krijger et al. (2001a) already describe the intrinsic differences and similarities between Ca II K and the TRACE UV diagnostics.

Inspection of Fig. 6.6 shows a very similar morphology in both space and time between the TRACE 1600 Å passband and Ca II K. When studying not only morphology but also Fourier information, results confirm that the TRACE 1600 Å passband has almost identical power and phase as the Ca II K. This is shown in Fig. 6.7 using the format described in Krijger et al. (2001a). The deviations from 0 degrees phase difference are well within the  $1\sigma$  estimates and likely due to the low cadence (40 s) of the TRACE observations.

Figures 6.6 and 6.7 indicate that TRACE 1600 Å passband observations can be used as a substitute for Ca II K in the absence of simultaneous groundbased Ca II K observations.

## 6.4 TRACE Ly $\alpha$ versus SUMER Ly $\alpha$

Handy et al. (1999b) used the Very Advanced Ultraviolet Telescope sounding rocket data to develop a method to construct Ly $\alpha$  images from TRACE images which are uncontaminated by UV continuum at longer wavelengths, by linearly combining TRACE 1216 Å and 1600 Å

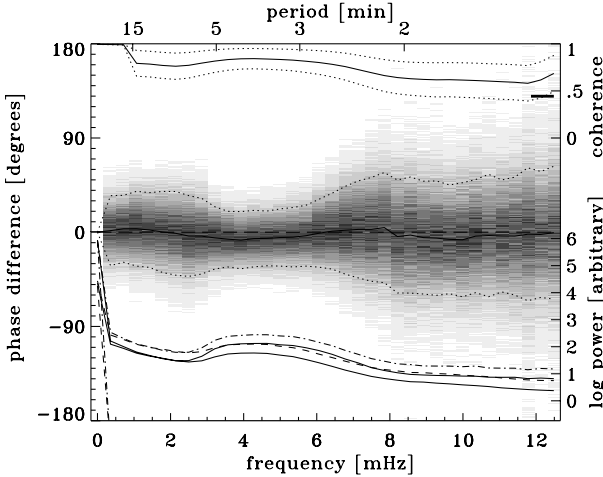


Figure 6.7: Various Fourier spectra of the May 8, 1999 brightness data for TRACE 1600 Å and VTT Ca II K, spatially averaged over the internetwork as a function of frequency (abscissa), corresponding periodicity specified along the top. The average power spectra are shown as solid curves in the lower half part show of the panel on a logarithmic scale (at right), with  $1\sigma$  estimates (dash-dotted and dashed curves, the lower ones drop below the panel due to the logarithmic scaling). The coherence  $C$  between the two signals is the solid curve in the upper half, with  $1\sigma$  estimates (dotted); scale is at the right, the extra tick at  $C = 0.45$  indicates the random noise value. The scatter diagram shows the phase differences, greyscale weighted by cross-power amplitude, between the two signals, scale at left, positive values corresponding to Ca II K brightness leading 1600 Å brightness. The solid curve is the spatial vector average phase difference with the  $1\sigma$  curves (dotted) determined from the weighted (by cross-power amplitude) phase differences. Coherence is high for all frequencies and phase difference is zero within the  $1\sigma$  estimates.

passbands. Our joint Ly $\alpha$  observations allow us to check this method. Figure 6.8 shows co-spatial and co-temporal timeslices, selecting different parts of the SUMER Ly $\alpha$  line and various TRACE passbands. During this observation the 1216 Å image quality suffered from heavy cosmic ray storms, resulting in a low quality construct. Despite this low quality the similarity between SUMER Ly $\alpha$  and TRACE Ly $\alpha$  construct is convincing.

Since the so-called 1216 Å passband actually transmits both Ly $\alpha$  photons and the 1600 Å continuum emission (the response function is double-peaked), one has to subtract the latter in order to get the Ly $\alpha$  signal only. This is done in the procedure of Handy et al. (1999a) which converts the original 1216 Å passband signal to the so-called Ly $\alpha$  construct. This construct corresponds to spectral intensity integrated over about 80 Å around Ly $\alpha$ , including its very extended wings.

Careful co-alignment enables us to compare  $y-t$  time slices of the SUMER Ly $\alpha$  sequence with those extracted for the SUMER slit position from the TRACE construct. Figure 6.8 displays  $y-t$  plots for the Ly $\alpha$  line core (1215.66 Å  $\pm$  1 Å), line wing (1210.66 Å to 1214.66 Å), the TRACE construct and TRACE 1600 Å.

The TRACE Ly $\alpha$  construct (bottom central panel of Fig. 6.8) is very different from the

SUMER whole Ly $\alpha$  line (top central panel of Fig. 6.8), but shows similar behaviour as the SUMER Ly $\alpha$  wing only. However, our TRACE Ly $\alpha$  construct suffers from heavy cosmic ray hits preventing a detailed comparison. Large scale features, such as indicated by the SUMER Ly $\alpha$  wing contours in the leftmost bottom panel of Fig. 6.8, correspond between the two different sequences.

It is surprising that while the Ly $\alpha$  line wing appears similar to the TRACE Ly $\alpha$  construct, the Ly $\alpha$  line core shows quite different behaviour from the Ly $\alpha$  wing. The line wing and TRACE construct exhibit oscillatory patterns almost everywhere and this is similar to patterns seen in the TRACE 1600 Å continuum which, as we have shown above, can be considered as a substitute to Ca II K. A high degree of similarity between the Ly $\alpha$  wing pattern observed by SUMER and optical Ca II K pattern was also reported by Betta et al. (1998). This agrees to the 700–1200 km formation heights indicated in Fig. 1 of Vernazza et al. (1981). On the other hand, the Ly $\alpha$  line-core  $y - t$  plot shows rather fuzzy structures with oscillatory behaviour that is rather different. This may reflect the fact that the line-core radiation comes from higher layers which differ, at least in this case, in oscillatory behaviour and could be already a part of the predicted canopies.

From the morphological characteristics in Fig. 6.8 we conclude that the TRACE Ly $\alpha$  construct shows oscillations in deeper chromospheric layers and is not dominated by the bright line-core emission as one would expect.

Note that if we integrate over all SUMER Ly $\alpha$  channels as shown in the top leftmost panel of Fig 6.8, the  $y - t$  plot is still dominated by the emission of the line core, i.e. appears like the Ly $\alpha$  line core scene rather than being similar to the line wing scene.

In order to investigate this striking core-wing difference, we have weighted the spectral radiance (intensity) of the average quiet Sun as given in the SUMER spectral atlas (Curdt et al. 2001) with the response function of the TRACE 1216 Å passband, taking only the wavelength range from 1200 Å to 1445 Å assuming that only this portion contributes to the TRACE Ly $\alpha$  construct. After normalization of the curve in Fig. 6.2 to 100% we find the following percentages of the radiance for the indicated wavelength ranges:

1215.66 Å ± 0.2 Å	53.5%
1215.66 Å ± 15 Å outside core	38.2%
red of 1231 Å	8.3%

This demonstrates that a significant part of the signal in the Ly $\alpha$  construct originates in the wings of Ly $\alpha$  and explains why the  $y - t$  plot of the TRACE Ly $\alpha$  construct shows similarities with SUMER  $y - t$  plots taken 1 Å to 5 Å away from the core, but no similarity with SUMER  $y - t$  plots taken in the core of Ly $\alpha$ .

## 6.5 Oscillations in higher Lyman lines and in the Lyman continuum

In Fig. 6.8 we show the dynamical behaviour of the Ly $\alpha$  line. As was already demonstrated in previous studies, higher Lyman lines clearly show oscillatory behaviour (Curdt & Heinzel 1998). Using the same data as used here, Curdt et al. (1999) studied oscillations in Ly $\beta$ , higher Lyman lines and the Lyman continuum and compared them to Ca II K. The Ly $\beta$  line

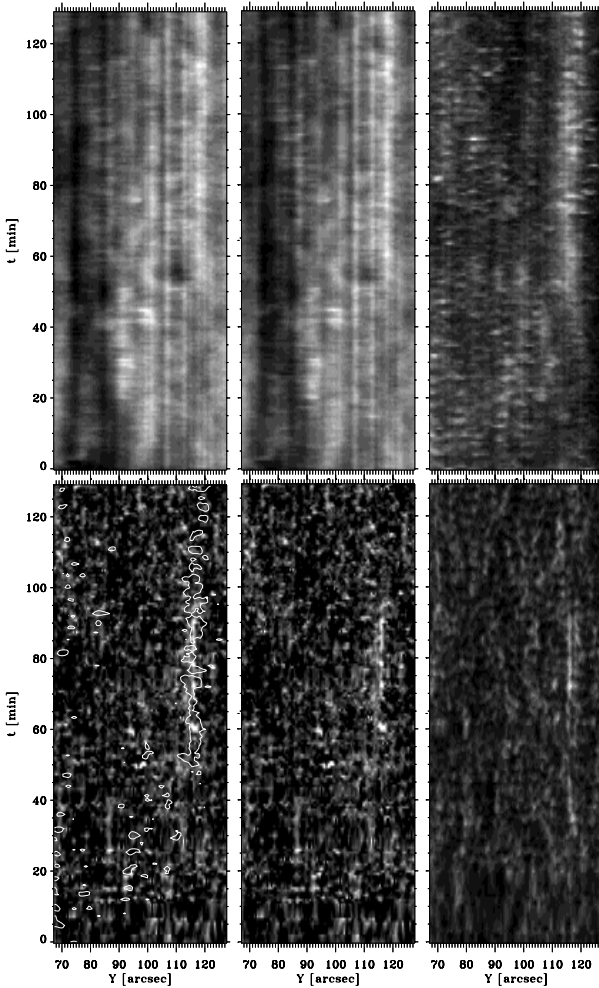


Figure 6.8: Linear intensity variation along the SUMER slit on May 4, 1999. Top row from left to right: SUMER Ly $\alpha$  core only, whole Ly $\alpha$  and Ly $\alpha$  wing. Bottom row from left to right: TRACE Ly $\alpha$  construct with contours of SUMER Ly $\alpha$  wing added, TRACE Ly $\alpha$  construct only and TRACE 1600 Å. Axes: Y in arcsec from disk centre, elapsed time in minutes covering the whole SUMER-TRACE overlap duration.

exhibits oscillations in the line-core intensity as well as the blue/red wing ratio (asymmetry) and the power peak around 5 mHz correlates well with the power peak for CaII K observed by the VTT (see Fig. 2 in Curdt et al. (1999)). However, an attempt to find phase correlations between CaII and Lyman lines higher than Ly $\alpha$  led to positive, but still conflicting results (Curdt et al. 1999). In this context we address the same data here again but using wavelet

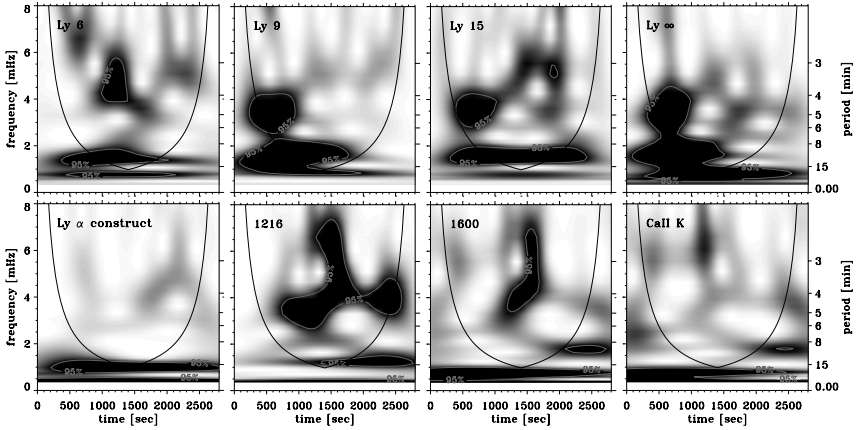


Figure 6.9: Panels for different passbands indicated in the upperright corner of each panel for an internetwork location covered by the SUMER slit (at  $Y=130.9$  arcsec (N)) for May 8 showing Fourier power as a function of time versus frequency. Domains with larger waveletpower appear darker. The power is clipped above 95% confidence levels which are indicated by the contours. The TRACE or SUMER passband are indicated in the top left of each waveletogram.

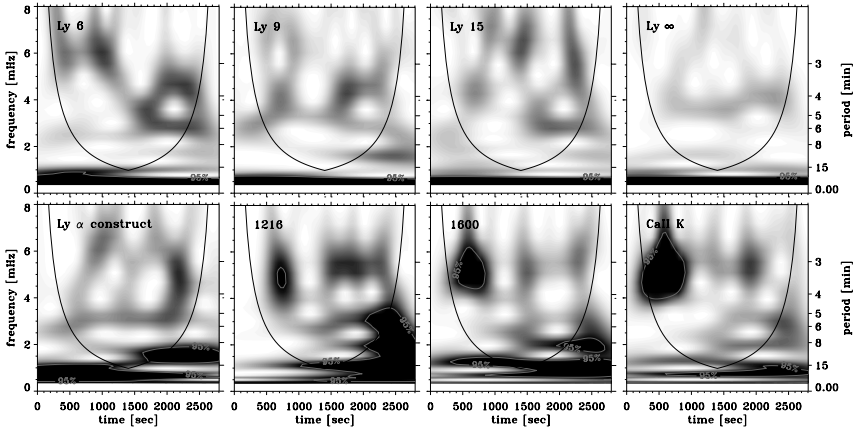


Figure 6.10: Same as in Fig. 6.9 but now for  $Y = 172.4$  arcsec (N).

analysis and adding data from TRACE. We investigated a large sample of wavetrains (signals) originating in different places within the internetwork and the network (along the SUMER slit) for the May 8 data. Since the behaviour of  $Ly\beta$  was already discussed by Curdt et al. (1999), we concentrate here on the behaviour of higher lines and continuum (note that since SUMER cannot observe all Lyman lines simultaneously, their variations must be studied separately for

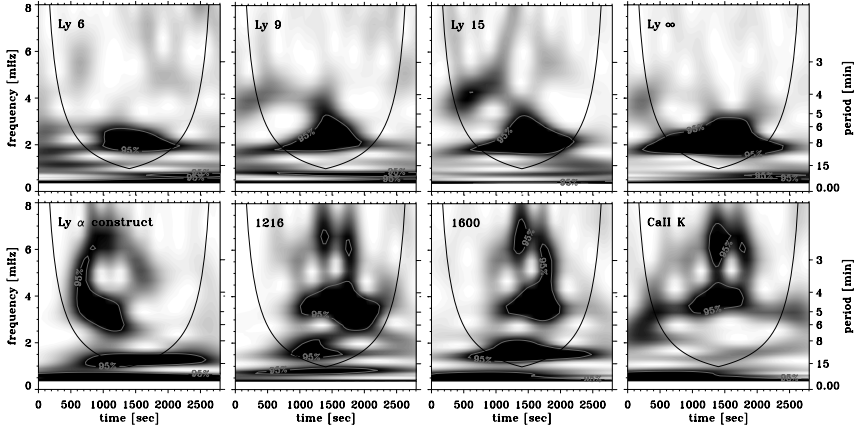


Figure 6.11: Same as in Fig. 6.9 but now for  $Y = 138.4$  arcsec (N), which is located in the network.

Ly $\alpha$ , Ly $\beta$  and higher lines plus continuum).

Figures 6.9 and 6.10 show examples of simultaneous internetwork observations, with SUMER in the Lyman lines Ly 6, Ly 9, Ly 15 and the Lyman continuum (denoted by Ly  $\infty$ ), with TRACE in the Ly $\alpha$  construct, 1216 Å and 1600 Å passbands and with the VTT in Ca II K. In the panels the 95% confidence levels are indicated with contours. The vertical tails visible at higher frequency are aliasing effects and not significant. The solid concave curve in each panel is the “cone of influence”; everything outside these cones should be distrusted due to inability of wavelets to sample beyond the finite duration of the observations. As expected, the frequency- and time-resolved power patterns displayed in these waveletograms differ for solar locations, but careful examination of our large sample of waveletograms shows both systematic similarities and systematic differences between these different spectral diagnostics for a given solar location.

Starting with the higher Lyman lines, we usually see a good correlation between Ly 9 and Ly 15 with strong power between in 3–5 min band. Similar periodicities were obtained by Curdt & Heinzel (1998), using another SUMER dataset. The Ly 6 line is sometimes different due to blending by the chromospheric O I line.

All TRACE passbands in Fig. 6.9 and 6.10 show similar behaviour, but they significantly differ from the higher Lyman lines and continuum which we can understand as the observed TRACE continua are formed in the lower chromosphere. Also the TRACE 1216 Å passband shows a similar character as the 1600 Å continuum and this again demonstrates that this channel is strongly contaminated by oscillations in the lower chromosphere and not by oscillations pertinent to Ly $\alpha$  itself. This is also clear from the TRACE Ly $\alpha$  construct pattern which is different.

Finally, the Ca II K waveletograms are closely similar to those for TRACE 1600 Å passband, confirming the results in Figs. 6.6 and 6.7. We observe time-varying oscillations (wavelets) with periods between 2 and 8 minutes, but that there is little or no correlation between

the lower and higher chromospheric layers. Similar results are also obtained from the network (Fig. 6.11), although the periods seem to be longer (see also Jensen & Orrall 1963; Lites et al. 1993; Heinzel & Curdt 1999).

## 6.6 Discussion and Conclusions

We have presented a comprehensive analysis of multiwavelength observations of quiet-Sun chromospheric oscillations. The principal objective of this study was to see whether there exists any clear correlation between oscillations in the lower chromosphere (VTT, TRACE continua) and the upper chromosphere and lower transition region. After examination of a large sample of waveletograms we came to a conclusion that although the whole atmosphere exhibits oscillatory behaviour with periods between 2-8 min (longer ones being also present), there are no obvious similarities between wavelet patterns corresponding to these two atmospheric regions. This is consistent with conclusions of Steffens et al. (1997) who compared Ca II K with selected transition-region lines observed by SUMER.

Figure 6.8 demonstrates that oscillations in the Ly $\alpha$  line show quite different behaviour in the line core and in the wings. The dynamical models of Carlsson & Stein (see, e.g., Carlsson & Stein 1999) are not aimed at reproducing emission lines formed higher-up in the chromosphere so that the only current knowledge about the formation of Ly $\alpha$  comes from static FAL models (Fontenla et al. 1993). The structure of the FAL-C model (see Avrett 1998) indicates that the Ly $\alpha$  core is formed at temperatures between  $10^4$  and  $4 \times 10^4$  K. The height is larger than 2000 km and we can only speculate whether this is above the magnetic canopy (Kopp & Kuperus 1968; Gabriel 1976; Schrijver & Zwaan 2000) or not (FAL models are just 1D models without any magnetic structure). The rather diffuse character of Fig. 6.8 for the line core can be interpreted in two ways. If the line core is formed already above the canopy, we will see the dynamical behaviour of various fluxtubes which are spatially much more extended than the compact grains. Another explanation is that the line core is formed below a high-lying canopy which is located relatively high and that the diffuse pattern is due to a 3D propagation of acoustic waves which expand as they propagate higher-up and are reflected from the overlying canopy (Rosenthal et al. 2002). This would be consistent with the fact that Ly $\alpha$  wings show similar pattern as TRACE 1600 Å continuum which, as we show in Sect. 6.3, can be regarded as a substitute of Ca II K. Counter argument to this scenario is our finding of the rather different dynamics of the Ly $\alpha$  core compared to its wings and from Ca II K. So either 3D propagation of waves changes substantially their dynamics (wavelet character) or the Ly $\alpha$  core is indeed formed above the canopy where the dynamics is quite different due to presence of magnetic fields.

We confirmed that TRACE 1600 Å imaging is closely similar to Ca II K filtergram imaging in exhibiting the dynamical patterns in the low chromosphere.

Handy et al. (1999b) suggested that the TRACE Ly $\alpha$  construct shows the whole line, yet we showed that the TRACE Ly $\alpha$  construct is dominated by the wings of Ly $\alpha$  and shows a similar morphology as the Ly $\alpha$  wing as observed by SUMER. Oscillations are present in both datasets, while some differences appear at smaller scales. However, our TRACE Ly $\alpha$  construct suffers from heavy cosmic ray hits. Also the observations were done at different cadence, which might cause short-term variations to differ. Calculations using the SUMER solar

spectrum show that the TRACE Ly $\alpha$  construct indeed is dominated by Ly $\alpha$  wing emission.

*Acknowledgements.* The SUMER project is supported by DLR, CNES, NASA and ESA PRODEX. SUMER is part of SOHO, the Solar and Heliospheric Observatory, of ESA and NASA. We would like to thank T. Tarbell for TRACE operation. J.M. Krijger's research is funded by The Netherlands Organization for Scientific Research (NWO). J.M. Krijger thanks the Leids Kerkhoven–Bosscha Fonds for travel support. P. Heinzel and J.M. Krijger are indebted to the Max-Planck Institut für Aeronomie in Katlenburg-Lindau for support and hospitality. P. Heinzel was also supported by grant A3003203 of the Academy of Sciences of the Czech Republic. Wavelet software was provided by C. Torrence and G. Compo, and is available at URL: <http://paos.colorado.edu/research/wavelets>. We are indebted to R.J.Rutten for many improvements to the manuscript.

---

# Hoofdstuk 7

## Structuur en dynamica van de zonnechromosfeer

een Nederlandse samenvatting

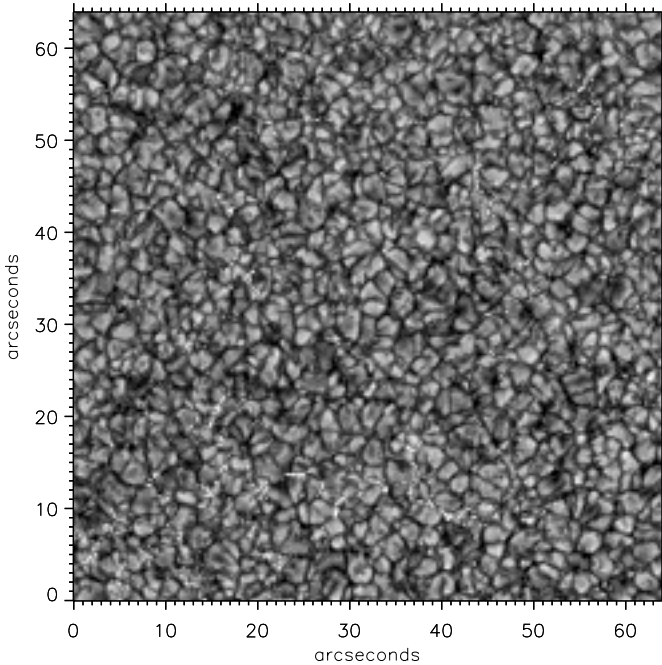


Figure 7.1: Een voorbeeld van granulatie, waargenomen door de Dutch Open Telescope op La Palma. Magnetische buizen zijn zichtbaar als kleine witte puntjes. Dit voorbeeld toont slechts één drieduizendste van het totale zonneoppervlak (1 boogseconde (“*arcsecond*”) aan de hemel is gelijk aan ongeveer 730 km op de zon).

**Granulatie** Energie wordt opgewekt in het centrum van de zon door middel van kernfusie. Deze energie wordt in het centrum van de zon naar buiten toe getransporteerd door middel van straling en in de buitenste lagen door middel van omhoog bewegende hete gasbellen net zoals in kokend water. Dit wordt *convectie* genoemd. Als deze gasbellen het oppervlak van de zon bereiken wordt de energie weer uitgestraald als het licht (grieks: photos) dat wij van de zon hier op aarde zien. Daarom wordt deze laag de *fotosfeer* genoemd. Deze oppervlaktelaag heeft een temperatuur rond de 4500 graden. Het steeds veranderend patroon van de gasbellen, noemen we *granulatie*. Een enkele granulatiebel of cel leeft ongeveer 10 minuten en is typisch 1000 km groot. De horizontale beweging van elke granulatiecel is een onderdeel van een veel grootschaliger patroon: de *supergranulatie* met cellen groter dan 15.000 km en een typische levensduur van een dag.

**Magnetisme** De zon zit vol met grote en kleine magnetische buizen, *flux buizen* (“flux tubes”), die soms dwars door de fotosfeer heenprikken in groepen. Deze buizen zijn lichter dan de omgeving en bezitten een opwaartse kracht. Ze worden door de horizontale beweging van het aanwezige gas meegeslept. Wanneer een magneetbuis onder invloed van de

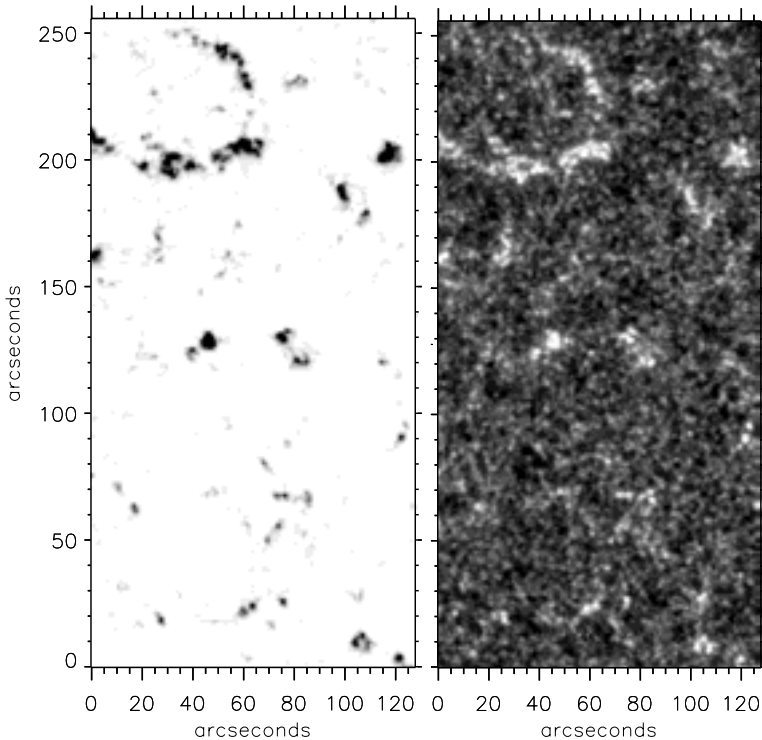


Figure 7.2: Links: Een voorbeeld van de verdeling van het magnetisch veld (zwart) in de fotosfeer. Rechts: Het heldere netwerk in de chromosfeer als gevolg van deze magneetvelden.

stromingen en opwaartse kracht voldoende dik is geworden is zij zichtbaar in de fotosfeer als een *zonnevlek*. Boven de fotosfeer strekken de meeste magnetische buizen zich uit tot ver in de ruimte en sluiten bij elkaar aan in de hogere lagen van de zonneatmosfeer: het overgangsgedebied (“*transition region*”) en de *corona*. Deze lagen zijn zeer ijl en geheel gedomineerd door deze magnetische velden. Het bijzondere aan de corona is dat deze een temperatuur heeft van twee miljoen graden, veel heter dan de fotosfeer van 4500 graden.

**Chromosfeer** Tussen de “koele” fotosfeer en de hete corona bevindt zich de *chromosfeer*. Zij vormt de laag waar de wisselwerking plaatsvindt tussen de zeer hete corona die gedomineerd wordt door magneetveld en de fotosfeer waarin het gas het magneetveld meesleept. De chromosfeer is zichtbaar in purperrood licht tijdens een volledige zonsverduistering. In dit overgangsgedebied waaiert het magneetveld dat in de fotosfeer nog opgesloten zit in aparte buizen uit tot een baldakijn (“*canopy*”) waarboven het magneetveld de hele ruimte vult. Het magneetveld wordt bijeengeveegd aan de randen van supergranulen en vormt een *netwerk* zichtbaar als heldere punten in de chromosfeer.

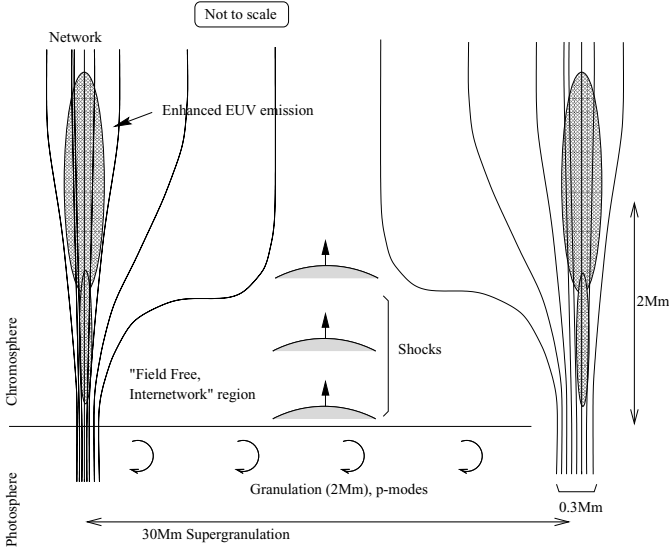


Figure 7.3: Schematische verticale plak van de lage zonneatmosfeer. Een enkele supergranule met magnetische buizen aan zijn randen wordt getoond met de chromosfeer erboven.

**Dit proefschrift** In het eerste hoofdstuk van dit proefschrift worden de verschillende eigenschappen van de zonneatmosfeer beschreven met het focus op de nog onopgeloste problemen, zoals de verhitting van de corona en chromosfeer en de bestudering van supergranulen.

In het tweede hoofdstuk is een techniek beschreven en getest waarmee, door de verschuiving te bepalen van een klein stukje zonsoppervlak tussen twee na elkaar genomen observaties, de beweging van granulen gevolgd kan worden.

In het derde hoofdstuk wordt deze techniek toegepast op een week lange waarneming met de ruimtesatelliet *TRACE* (Transition Region and Coronal Explorer). In het zo bepaalde bewegingspatroon worden magnetische buizen losgelaten en hun verschillende eigenschappen bestudeerd. Na vergelijking van de resultaten met de huidige modellen en ideeën over granulatie wordt aangetoond dat nieuw omhoog komende magnetische buizen (fluxtubes) snel ( $\sim 100$  m/sec) naar de randen van de supergranulen bewegen en daar het chromosferisch netwerk in stand houden. Ook wordt in dit hoofdstuk het recente resultaat bevestigd dat supergranulatiecellen kleiner zijn dan voorheen aangenomen ( $\sim 18000$  km).

In het vierde hoofdstuk worden trillingen en golven in de chromosfeer bestudeerd. Er wordt aangetoond dat de chromosfeer beheerst wordt door omhoog lopende geluidsgolven. Ook wordt er een sterke aanwijzing voor een ander bepaald soort golven gevonden, *interne gravitatie golven*, waar in het vijfde hoofdstuk beter naar wordt gekeken.

In het zesde hoofdstuk worden de trillingen en golven het overgangsgebied in gevolgd. Met simultane observaties van meerdere telescopen wordt aangetoond dat trillingen in dichtbij elkaar gelegen lagen in de zonneatmosfeer veel gelijkenis vertonen, maar tussen de lagere

chromosfeer en het hogere overgangsgebied is weinig correlatie. Dit kan worden uitgelegd met een magnetisch baldakijn tussen deze twee lagen in, waar de eigenschappen van de trillingen en golven veranderen.

---



# **Bibliography**

- Appourchaux, T., Fröhlich, C., Andersen, B., et al. 2000, *ApJ*, 538, 401
- Athay, R. G. 1970, *Sol. Phys.*, 11, 347
- Athay, R. G. & Lites, B. W. 1972, *ApJ*, 176, 809
- Avrett, E. H. 1998, in *Solar Electromagnetic Radiation Study for Solar Cycle 22*, 449
- Bahng, J. & Schwarzschild, M. 1961, *ApJ*, 134, 312
- Balthasar, H., Grosser, H., Schröter, C., & Wiehr, E. 1990, *A&A*, 235, 437
- Beck, J. G. & Duvall, T. L. 2001, in *Helio- and asteroseismology at the dawn of the millennium*, ed. A. Wilson, *Procs. of the SOHO 10/GONG 2000 Workshop (ESA SP-464)*, 577
- Beckers, J. M. 1968, *Sol. Phys.*, 3, 367
- Beckers, J. M. & Artzner, G. 1974, *Sol. Phys.*, 37, 309
- Berger, T. E., Löfdahl, M. G., Shine, R. S., & Title, A. M. 1998, *ApJ*, 495, 973
- Bessey, R. J. & Kuperus, M. 1970, *Sol. Phys.*, 12, 216
- Betta, R., Hansteen, V., Carlsson, M., & Wilhelm, K. 1998, *Memorie della Societa Astronomica Italiana*, 69, 699
- Biermann, L. 1946, *Naturwiss.*, 33, 118
- Biermann, L. 1948, *Zeitschrift Astrophysics*, 25, 161
- Bonet, J. A., Marquez, I., Vázquez, M., & Wöhl, H. 1991, *A&A*, 244, 492
- Bonnet, R. M., Decaudin, M., Foing, B., et al. 1982, *A&A*, 111, 125
- Brandt, P. N., Rutten, R. J., Shine, R. A., & Trujillo Bueno, J. 1992, in *Cool Stars, Stellar Systems, and the Sun*, ed. M. S. Giampapa & J. A. Bookbinder, *Proc. Seventh Cambridge Workshop (Vol. 26: Astron. Soc. Pacific Conf. Series)*, 161
- . 1994, in *Solar Surface Magnetism*, ed. R. J. Rutten & C. J. Schrijver, *NATO ASI Series C 433 (Dordrecht: Kluwer)*, 251
- Brault, J. W. & White, O. R. 1971, *A&A*, 13, 169
- Braun, D. C. & Lindsey, C. 1999, *ApJ*, 513, L79
- Braun, D. C., Lindsey, C., Fan, Y., & Jefferies, S. M. 1992, *ApJ*, 392, 739
- Bray, R. J., Loughhead, R. E., & Durrant, C. J. 1984, *The solar granulation (2nd edition)* (Cambridge University Press), 270
-

- Brown, T. M., Bogdan, T. J., Lites, B. W., & Thomas, J. H. 1992, *ApJ*, 394, L65
- Brown, T. M. & Harrison, R. L. 1980, *ApJ*, 236, L169
- Brueckner, G. E. 1980, *Highlights of Astronomy (IAU)*, 5, 557
- Bruls, J. H. M. J., Rutten, R. J., & Shchukina, N. G. 1992, *A&A*, 265, 237
- Cadez, V. M., Csik, A., Erdelyi, R., & Goossens, M. 1997, *A&A*, 326, 1241
- Carlsson, M. 1999, in *Magnetic Fields and Solar Processes*, ed. A. Wilson, Proc. 9th European Meeting on Solar Physics, ESA SP-448 (ESTEC, Noordwijk: ESA Publ. Div.), 183
- Carlsson, M., Judge, P. G., & Wilhelm, K. 1997, *ApJ*, 486, L63
- Carlsson, M. & Stein, R. F. 1992, *ApJ*, 397, L59
- . 1994, in *Chromospheric Dynamics*, ed. M. Carlsson, Proc. Miniworkshop (Oslo: Inst. Theor. Astrophys.), 47
- . 1995, *ApJ*, 440, L29
- . 1997, *ApJ*, 481, 500
- Carlsson, M. & Stein, R. F. 1998, in *New Eyes to See Inside the Sun and Stars*, ed. F.-L. Deubner, J. Christensen-Dalsgaard, & D. Kurtz, Procs. IAU Symp. 185 (Kyoto) (Dordrecht: Kluwer), 435
- Carlsson, M. & Stein, R. F. 1999, in *Magnetic Fields and Oscillations*, ed. B. Schmieder, A. Hofmann, & J. Staude, Procs. Third Adv. Solar Physics Euroconf. (Astron. Soc. Pacific Conf. Series 184), 206
- Carrington, R. C. 1859, *MNRAS*, 20, 13
- Cattaneo, F., Lenz, D., & Weiss, N. 2001, *ApJ*, 563, L91
- Christensen-Dalsgaard, J. 1988, *IAU Symposia*, 123, 3
- Cook, J. W., Brückner, G. E., & Bartoe, J. D. F. 1983, *ApJ*, 270, L89
- Cook, J. W., Rutten, R. J., & Hoekzema, N. M. 1996, *ApJ*, 470, 647
- Cram, L. E. 1972, *Sol. Phys.*, 22, 375
- . 1978a, *A&A*, 67, 301
- . 1978b, *A&A*, 70, 345
- Cram, L. E. & Dame, L. 1983, *ApJ*, 272, 355
- Cuntz, M., Rammacher, W., Ulmschneider, P., Musielak, Z. E., & Saar, S. H. 1999, *ApJ*, 522, 1053
-

- Curdt, W., Brekke, P., Feldman, U., et al. 2001, *A&A*, 375, 591
- Curdt, W. & Heinzel, P. 1998, *ApJ*, 503, L95
- Curdt, W., Heinzel, P., Schmidt, W., et al. 1999, in *Magnetic Fields and Solar Processes*, ed. A. Wilson, Proc. 9th European Meeting on Solar Physics, ESA SP-448 (ESTEC, Noordwijk: ESA Publ. Div.), 177
- Curdt, W., Heinzel, P., von Uexküll, M., et al. 1999, in *Magnetic Fields and Solar Processes*, ed. A. Wilson, Proc. 9th European Meeting on Solar Physics, ESA SP-448 (ESTEC, Noordwijk: ESA Publ. Div.), 33
- Daglis, I. A., ed. 2001, *Space Storms and Space Weather Hazards*
- Damé, L., Foing, B., Martić, M., et al. 1986, *Adv. Spac. Res.*, 6, 273
- De Pontieu, B., Martens, P. C. H., & Hudson, H. S. 2001, *ApJ*, 558, 859
- De Rosa, M., Duvall, T. L., & Toomre, J. 2000, *Sol. Phys.*, 192, 351
- Dere, K. P. & Cook, J. W. 1983, *A&A*, 124, 181
- Deubner, F. L. 1988, *A&A*, 204, 301
- Deubner, F.-L. 1990, in *The Solar Photosphere: Structure, Convection and Magnetic Fields*, ed. J.-O. Stenflo, Proceedings IAU Symposium 138 (Kiev) (Dordrecht: Kluwer), 217
- Deubner, F.-L. 1998, in *New Eyes to See Inside the Sun and Stars*, ed. F.-L. Deubner, J. Christensen-Dalsgaard, & D. Kurtz, Procs. IAU Symp. 185 (Kyoto) (Dordrecht: Kluwer), 427
- Deubner, F.-L., Endler, F., & Staiger, J. 1984, *Mem. Soc. Astron. Italia*, 55<sup>o</sup>, 135
- Deubner, F. L. & Fleck, B. 1989, *A&A*, 213, 423
- . 1990, *A&A*, 228, 506
- Deubner, F. L., Fleck, B., Schmitz, F., & Straus, T. 1992, *A&A*, 266, 560
- Deubner, F. L. & Gough, D. 1984, *ARA&A*, 22, 593
- Deubner, F.-L. & Steffens, S. 1999, in *Magnetic Fields and Solar Processes*, ed. A. Wilson, Proc. 9th European Meeting on Solar Physics, ESA SP-448 (ESTEC, Noordwijk: ESA Publ. Div.), 149
- Deubner, F. L., Waldschik, T., & Steffens, S. 1996, *A&A*, 307, 936
- Domingo, V., Fleck, B., & Poland, A. I. 1995, *Sol. Phys.*, 162, 1
- Doyle, J. G., van den Oord, G. H. J., O'Shea, E., & Banerjee, D. 1999, *A&A*, 347, 335
-

- Durrant, C. J. & Nesis, A. 1981, *A&A*, 95, 221
- Duvall, T. L. 1982, *Nature*, 300, 242
- Duvall, T. L., Jefferies, S. M., Harvey, J. W., & Pomerantz, M. A. 1993, *Nature*, 362, 430
- Edmonds, F. N. & Webb, C. J. 1972, *Sol. Phys.*, 22, 276
- Emonet, T. & Cattaneo, F. 2001, *ApJ*, 560, L197
- Endler, F. & Deubner, F. L. 1983, *A&A*, 121, 291
- Espagnet, O., Muller, R., Roudier, T., Mein, N., & Mein, P. 1995, *A&AS*, 109, 79
- Evans, J. W. & Catalano, C. P. 1972, *Sol. Phys.*, 27, 299
- Foing, B. & Bonnet, R. M. 1984a, *A&A*, 136, 133
- . 1984b, *ApJ*, 279, 848
- Foing, B., Bonnet, R.-M., & Bruner, M. 1986, *A&A*, 162, 292
- Fontenla, J. M., Avrett, E. H., & Loeser, R. 1993, *ApJ*, 406, 319
- Forbes, T. G. 2000, *J. Geophys. Res.*, 105, 23153
- Frazier, E. N. 1968, *ApJ*, 152, 557
- Gabriel, A. H. 1976, *Royal Society of London Philosophical Transactions Series*, 281, 339
- Georgobiani, D., Kosovichev, A. G., Nigam, R., Nordlund, Å., & Stein, R. F. 2000, *ApJ*, 530, L139
- Giovanelli, R. G. 1980, *Sol. Phys.*, 68, 49
- Giovanelli, R. G. & Jones, H. P. 1982, *Sol. Phys.*, 79, 267
- Goode, P. R., Strous, L. H., Rimmele, T. R., & Stebbins, R. T. 1998, *ApJ*, 495, L27
- Goodman, M. L. 1996, *ApJ*, 463, 784
- . 2000, *ApJ*, 533, 501
- Gouttebroze, P., Vial, J. C., Bocchialini, K., Lemaire, P., & Leibacher, J. W. 1999, *Sol. Phys.*, 184, 253
- Hagenaar, H. J. 2001, *ApJ*, 555, 448
- Hagenaar, H. J., Schrijver, C. J., & Title, A. M. 1997, *ApJ*, 481, 988
- Hagenaar, H. J., Schrijver, C. J., Title, A. M., & Shine, R. A. 1999, *ApJ*, 511, 932
-

- Handy, B. N., Acton, L. W., Kankelborg, C. C., et al. 1999a, *Sol. Phys.*, 187, 229
- Handy, B. N., Bruner, M. E., Tarbell, T. D., et al. 1998, *Sol. Phys.*, 183, 29
- Handy, B. N., Tarbell, T. D., Wolfson, C. J., Korendyke, C. M., & Vourlidas, A. 1999b, *Sol. Phys.*, 190, 351
- Hanslmeier, A., Kučera, A., Rybák, J., Neunteufel, B., & Wöhl, H. 2000, *A&A*, 356, 308
- Harrison, R. A., Sawyer, E. C., Carter, M. K., et al. 1995, *Sol. Phys.*, 162, 233
- Harvey, K. & Harvey, J. 1995, Air Force Rep. AFGL-TR-76-0225
- Harvey-Angle, K. L. 1993, *Magnetic Bipoles on the Sun* (Utrecht University: PhD Thesis)
- Hasan, S. S. & Kalkofen, W. 1999, *ApJ*, 519, 899
- Hathaway, D. H., Beck, J. G., Han, S., & Raymond, J. 2002, *Sol. Phys.*, 205, 25
- Heinzel, P. & Curdt, W. 1999, in *ASP Conf. Ser. 184: Third Advances in Solar Physics Euro-conference: Magnetic Fields and Oscillations*, 201
- Hildner, E., Gosling, J. T., Hansen, R. T., & Bohlin, J. D. 1975, *Sol. Phys.*, 45, 363
- Hindman, B. W. & Brown, T. M. 1998, *ApJ*, 504, 1029
- Hoekzema, N. M. & Brandt, P. N. 2000, *A&A*, 353, 389
- Hoekzema, N. M., Brandt, P. N., & Rutten, R. J. 1998, *A&A*, 333, 322
- Hoekzema, N. M., Rimmele, T. R., & Rutten, R. J. 2002, *A&A*, 390, 681
- Hoekzema, N. M. & Rutten, R. J. 1998, *A&A*, 329, 725
- Hoekzema, N. M., Rutten, R. J., Brandt, P. N., & Shine, R. A. 1998b, *A&A*, 329, 276
- Hoekzema, N. M., Rutten, R. J., & Cook, J. W. 1997, *ApJ*, 474, 518
- Hollweg, J. V. 1982, *ApJ*, 257, 345
- Jefferies, S. M. 1998, in *New Eyes to See Inside the Sun and Stars*, ed. F.-L. Deubner, J. Christensen-Dalsgaard, & D. Kurtz, *Procs. IAU Symp. 185 (Kyoto)* (Dordrecht: Kluwer), 415
- Jefferies, S. M., Osaki, Y., Shibahashi, H., et al. 1997, *ApJ*, 485, L49
- Jensen, E. & Orrall, F. Q. 1963, *PASP*, 75, 162
- Jones, H. P. & Giovanelli, R. G. 1982, *Sol. Phys.*, 79, 247
- . 1983, *Sol. Phys.*, 87, 37
-

- Judge, P. G. & Peter, H. 1998, in *Solar Composition and its Evolution from Core to Corona*, ed. C. Fröhlich, M. C. E. Huber, S. Solanki, & R. von Steiger, *Procs. ISSI Workshop (85: Space Sci. Rev.)*, 187
- Judge, P. G. & Peter, H. 1998, in *Solar Composition and Its Evolution From Core to Corona*, 187
- Judge, P. G., Tarbell, T. D., & Wilhelm, K. 2001, *ApJ*, 554, 424
- Kalkofen, W. 1991, *The heating of the solar chromosphere (Solar interior and atmosphere (A92-36201 14-92)*. Tucson, AZ, University of Arizona Press, 1991, p. 911-932.), 911
- . 1997, *ApJ*, 486, L145
- . 1999, in *Magnetic Fields and Oscillations*, ed. B. Schmieder, A. Hofmann, & J. Staude, *Procs. Third Adv. Solar Physics Euroconf. (Astron. Soc. Pacific Conf. Series 184)*, 227
- Kalkofen, W., Ulmschneider, P., & Avrett, E. H. 1999, *ApJ*, 521, L141
- Keller, C. U., Deubner, F. L., Egger, U., Fleck, B., & Povel, H. P. 1994, *A&A*, 286, 626
- Keppens, R. & Goedbloed, J. P. 2000, *ApJ*, 530, 1036
- Kiefer, M. & Balthasar, H. 1998, *A&A*, 335, L73
- Kneer, F. & von Uexküll, M. 1983, *A&A*, 119, 124
- . 1985, *A&A*, 144, 443
- . 1986, *A&A*, 155, 178
- . 1993, *A&A*, 274, 584
- Komm, R., Mattig, W., & Nesis, A. 1991, *A&A*, 252, 827
- Kopp, G., Lindsey, C., Roellig, T. L., et al. 1992, *ApJ*, 388, 203
- Kopp, R. A. & Kuperus, M. 1968, *Sol. Phys.*, 4, 212
- Krijger, J. M., Roudier, T., & Rieutord, M. 2002, *A&A*, 387, 672
- Krijger, J. M., Rutten, R. J., Lites, B. W., et al. 2001, *A&A*, 379, 1052
- Kucera, A., Rybak, J., & Wöhl, H. 1995, *A&A*, 298, 917
- Kumar, P. 1994, *ApJ*, 428, 827
- Kumar, P., Fardal, M. A., Jefferies, S. M., et al. 1994, *ApJ*, 422, L29
- Kuperus, M. & Athay, R. G. 1967, *Sol. Phys.*, 1, 361
- Leahy, D. A., Darbro, W., Elsner, R. F., et al. 1983, *ApJ*, 266, 160
-

- Leibacher, J. W., Noyes, R. W., Toomre, J., & Ulrich, R. K. 1985, *Scientific American*, 253, 48
- Leibacher, J. W. & Stein, R. F. 1971, *Astrophys. Lett.*, 7, 191
- Leighton, R. B., Noyes, R. W., & Simon, G. W. 1962, *ApJ*, 135, 474
- Lighthill, M. F. 1967, in *IAU Symp. 28: Aerodynamic Phenomena in Stellar Atmospheres*, Vol. 28, 429
- Lin, H. 1995, *ApJ*, 446, 421
- Lin, H. & Rimmele, T. 1999, *ApJ*, 514, 448
- Lisle, J., De Rosa, M., & Toomre, J. 2000, *Sol. Phys.*, 197, 21
- Lites, B. W. & Chipman, E. G. 1979, *ApJ*, 231, 570
- Lites, B. W., Chipman, E. G., & White, O. R. 1982, *ApJ*, 253, 367
- Lites, B. W., Leka, K. D., Skumanich, A., Martínez Pillet, V., & Shimizu, T. 1996, *ApJ*, 460, 1019
- Lites, B. W., Rutten, R. J., & Berger, T. E. 1999, *ApJ*, 517, 1013
- Lites, B. W., Rutten, R. J., & Kalkofen, W. 1993, *ApJ*, 414, 345
- Lites, B. W., Rutten, R. J., & Thomas, J. H. 1994, in *Solar Surface Magnetism*, ed. R. J. Rutten & C. J. Schrijver, NATO ASI Series C 433 (Dordrecht: Kluwer), 159
- Lites, B. W., Thomas, J. H., Bogdan, T. J., & Cally, P. S. 1998, *ApJ*, 497, 464
- Liu, S. Y. & Sheeley, N. R. 1971, *Sol. Phys.*, 20, 282
- Liu, S.-Y. & Skumanich, A. 1974, *Sol. Phys.*, 38, 109
- Livingston, W. & Harvey, J. 1971, in *IAU Symp. 43: Solar Magnetic Fields*, Vol. 43, 51
- Lockwood, M. 2002, *A&A*, 382, 678
- Löfdahl, M. G., Berger, T. E., Shine, R. S., & Title, A. M. 1998, *ApJ*, 495, 965
- Marsh, N. & Svensmark, H. 2000, *Space Science Reviews*, 94, 215
- Martić, M. & Damé, L. 1989, in *Solar and Stellar Granulation*, ed. R. J. Rutten & G. Severino, NATO ASI Series C 263 (Dordrecht: Kluwer), 207
- Martin, S. F. 1990, in *IAU Symposium*, Vol. 138, 129
- McIntosh, S. W., Bogdan, T. J., Cally, P. S., et al. 2001, *ApJ*, 548, L237
- McIntosh, S. W. & Judge, P. G. 2001, *ApJ*, 561, 420
-

- Mihalas, B. W. & Toomre, J. 1981, *ApJ*, 249, 349
- . 1982, *ApJ*, 263, 386
- Moore, R. L., Falconer, D. A., Porter, J. G., & Suess, S. T. 1999, *ApJ*, 526, 505
- Muller, R., Hulot, J. C., & Roudier, T. 1989, *Sol. Phys.*, 119, 229
- Musielak, Z. E., Rosner, R., Stein, R. F., & Ulmschneider, P. 1994, *ApJ*, 423, 474
- Narain, U. & Ulmschneider, P. 1996, *Space Science Reviews*, 75, 453
- Neckel, H. 1999, *Sol. Phys.*, 184, 421
- Nigam, R. & Kosovichev, A. G. 1999a, *ApJ*, 510, L149
- . 1999b, *ApJ*, 514, L53
- Nindos, A. & Zirin, H. 1998, *Sol. Phys.*, 179, 253
- November, L. J. & Simon, G. W. 1988, *ApJ*, 333, 427
- November, L. J., Toomre, J., Gebbie, K. B., & Simon, G. W. 1981, *ApJ*, 245, L123
- Oliviero, M., Severino, G., Straus, T., Jefferies, S. M., & Appourchaux, T. 1999, *ApJ*, 516, L45
- Pintér, B., Erdélyi, R., & New, R. 2001, *A&A*, 372, L17
- Ploner, S. R. O., Solanki, S. K., & Gadun, A. S. 2000, *A&A*, 356, 1050
- Poedts, S. 2001, in *SOLSPA 2001 Euroconference: Solar Cycle and Space Weather*
- Porter, J. G., Moore, R. L., Reichmann, E. J., Engvold, O., & Harvey, K. L. 1987, *ApJ*, 323, 380
- Rast, M. P. 1995, *ApJ*, 443, 863
- . 1999, *ApJ*, 524, 462
- Rhodes, E. J., Reiter, J., Kosovichev, A. G., Schou, J., & Scherrer, P. H. 1998, *American Astronomical Society Meeting*, 30, 845
- Rieutord, M., Roudier, T., Ludwig, H.-G., Nordlund, Å., & Stein, R. 2001, *A&A*, 377, L14
- Rieutord, M., Roudier, T., Malherbe, J. M., & Rincon, F. 2000, *A&A*, 357, 1063
- Rosenthal, C. S., Bogdan, T. J., Carlsson, M., et al. 2002, *ApJ*, 564, 508
- Roudier, T., Rieutord, M., Malherbe, J. M., & Vigneanu, J. 1999, *A&A*, 349, 301
-

- Rutten, R. J. 1988, in *Physics of Formation of FeII Lines Outside LTE*, ed. R. Viotti, A. Vittono, & M. Friedjung, IAU Coll94 (Dordrecht: Reidel), 185
- . 1994, in *Chromospheric Dynamics*, ed. M. Carlsson, Proc. Miniworkshop (Oslo: Inst. Theor. Astrophys.), 25
- . 1995, in *Helioseismology*, ed. J. T. Hoeksema, V. Domingo, B. Fleck, & B. Battrick, Proc. Fourth SOHO Workshop (ESA Publ. Div., ESTEC, Noordwijk: ESA SP Vol. 1), 151
- . 1997, in *Advances in the Physics of Sunspots*, ed. B. Schmieder, J. C. del Toro Iniesta, & M. Vázquez, Procs. First Adv. in Solar Physics Euroconf. (Vol. 118: Astron. Soc. Pacific Conf. Series), 298
- . 1998, in *Solar Composition and Its Evolution From Core to Corona*, 269
- . 1999, in *Magnetic Fields and Oscillations*, ed. B. Schmieder, A. Hofmann, & J. Staude, Procs. Third Adv. in Solar Physics Euroconf. (Vol. 184: Astron. Soc. Pacific Conf. Series), 181
- . 2000, *Radiative Transfer in Stellar Atmospheres (7th WWW Edition, <http://www.astro.uu.nl/~rutten>: Lecture Notes Utrecht University)*
- . 2001, in *Cool Stars, Stellar Systems and the Sun*, ed. R. J. García López, R. Rebolo, & M. R. Zapatero Osorio, Procs. 11th Cambridge Workshop (Vol. 223: Astron. Soc. Pacific Conf. Series), 117
- Rutten, R. J., de Pontieu, B., & Lites, B. 1999a, in ASP Conf. Ser. 183: *High Resolution Solar Physics: Theory, Observations, and Techniques*, 383
- Rutten, R. J., Lites, B. W., Berger, T. E., & Shine, R. A. 1999b, in *Solar and Stellar Activity: Similarities and Differences*, ed. C. J. Butler & J. G. Doyle, Procs. Armagh Workshop (Vol. 158: Astron. Soc. Pacific Conf. Series), 249
- Rutten, R. J. & Uitenbroek, H. 1991a, *Sol. Phys.*, 134, 15
- . 1991b, in *Mechanisms of Chromospheric and Coronal Heating*, ed. P. Ulmschneider, E. R. Priest, & R. Rosner, Proc. Heidelberg Conf. (Berlin: Springer Verlag), 48
- Rybák, J., Curdt, W., Kučera, A., Schühle, U., & Wöhl, H. 1999, in *Magnetic Fields and Solar Processes*, ed. A. Wilson, Procs. 9th European Meeting on Solar Physics, ESA SP-448 (ESTEC, Noordwijk: ESA Publ. Div.), 72
- Scherrer, P. H., Bogart, R. S., Bush, R. I., et al. 1995, *Sol. Phys.*, 162, 129
- Schmieder, B. 1976, *Sol. Phys.*, 47, 435
- . 1977, *Sol. Phys.*, 54, 269
- . 1978, *Sol. Phys.*, 57, 245
-

- Schmitz, F. & Steffens, S. 1999, *A&A*, 344, 973
- Schrijver, C. J., Title, A. M., Berger, T. E., et al. 1999, *Sol. Phys.*, 187, 261
- Schrijver, C. J., Title, A. M., van Ballegooijen, A. A., Hagenaar, H. J., & Shine, R. A. 1997, *ApJ*, 487, 424
- Schrijver, C. J. & Zwaan, C. 2000, *Solar and stellar magnetic activity (Solar and stellar magnetic activity / Carolus J. Schrijver, Cornelius Zwaan. New York : Cambridge University Press, 2000. (Cambridge astrophysics series ; 34))*
- Schwarzschild, M. 1948, *ApJ*, 107, 1
- Shine, R. A., Frank, Z. A., Tarbell, T. D., & Simon, G. W. 2001, in *American Geophysical Union, Fall Meeting 2001*, abstract#SH11A-0702, A702
- Shine, R. A. & Linsky, J. L. 1974, *Sol. Phys.*, 39, 49
- Shine, R. A., Simon, G. W., & Hurlburt, N. E. 2000, *Sol. Phys.*, 193, 313
- Simon, G. W., Title, A. M., Topka, K. P., et al. 1988, *ApJ*, 327, 964
- Simon, G. W., Title, A. M., & Weiss, N. O. 1995, *ApJ*, 442, 886
- . 2001, *ApJ*, 561, 427
- Sivaraman, K. R., Gupta, S. S., Livingston, W. C., et al. 2000, *A&A*, 363, 279
- Skartlien, R. 1998, *Three-Dimensional Modeling of Solar Convection and Atmosphere Dynamics (Oslo University: PhD thesis)*
- Skartlien, R., Carlsson, M., & Stein, R. F. 1994, in *Chromospheric Dynamics*, ed. M. Carlsson, *Proc. Miniworkshop (Oslo: Inst. Theor. Astrophys.)*, 79
- Skartlien, R. & Rast, M. P. 2000, *ApJ*, 535, 464
- Skartlien, R., Stein, R. F., & Nordlund, Å. 2000, *ApJ*, 541, 468
- Solanki, S. K. & Brigljevic, V. 1992, *A&A*, 262, L29
- Solanki, S. K. & Fligge, M. 2000, *Space Science Reviews*, 94, 127
- Solanki, S. K. & Steiner, O. 1990, *A&A*, 234, 519
- Somov, B. V. 1992, *Physical processes in solar flares (Physical processes in solar flares Kluwer Academic Publishers (Astrophysics and Space Science Library. Vol. 172), 257 p.)*, 65
- Soon, W. H., Posmentier, E. S., & Baliunas, S. L. 1996, *ApJ*, 472, 891
- Spruit, H. C. 1976, *Sol. Phys.*, 50, 269
-

- Staiger, J. 1987, *A&A*, 175, 263
- Staiger, J., Mattig, W., Schmieder, B., & Deubner, F. L. 1984, *Memorie della Societa Astronomica Italiana*, 55, 147
- Steffens, S., Deubner, F.-L., Fleck, B., et al. 1997, in *Advances in the physics of sunspots*, ed. B. Schmieder, J. C. del Toro Iniesta, & M. Vázquez, *Procs. First Adv. in Solar Physics Euroconf. (Vol. 118: Astron. Soc. Pacific Conf. Series)*, 284
- Steffens et al., S. 1997, in *Fifth SOHO Workshop: The Corona and Solar Wind Near Minimum Activity*, 685
- Stein, R. F. 1967, *Sol. Phys.*, 2, 385
- Stein, R. F. & Carlsson, M. 1997, in *ASSL Vol. 225: SCORE'96 : Solar Convection and Oscillations and their Relationship*, 261
- Stein, R. F. & Nordlund, A. 1998, *ApJ*, 499, 914
- Steiner, O., Pneuman, G. W., & Stenflo, J. O. 1986, *A&A*, 170, 126
- Stix, M. 2000, *Sol. Phys.*, 196, 19
- Straus, T. & Bonaccini, D. 1997, *A&A*, 324, 704
- Straus, T., Severino, G., Deubner, F. L., et al. 1999, *ApJ*, 516, 939
- Strous, L. H. 1994, *Dynamics in Solar Active Regions: Patterns in Magnetic-Flux Emergence (Utrecht University: PhD thesis)*
- . 1995, in *Helioseismology*, ed. J. Hoeksema, V. Domingo, B. Fleck, & B. Battrick, *Proc. of 4th Soho Workshop (ESA SP-376)*, 213P
- Suemoto, Z., Hiei, E., & Nakagomi, Y. 1987, *Sol. Phys.*, 112, 59
- . 1990, *Sol. Phys.*, 127, 11
- Theurer, J., Ulmschneider, P., & Cuntz, M. 1997a, *A&A*, 324, 587
- Theurer, J., Ulmschneider, P., & Kalkofen, W. 1997b, *A&A*, 324, 717
- Thomas, J. H. & Stanchfield, D. C. H. 2000, *ApJ*, 537, 1086
- Title, A. M. & Berger, T. E. 1996, *ApJ*, 463, 797
- Title, A. M., Tarbell, T. D., Topka, K. P., et al. 1989, *ApJ*, 336, 475
- Toner, C. G. & Labonte, B. J. 1993, *ApJ*, 415, 847
- Uitenbroek, H. 1989, *A&A*, 213, 360
-

- Ulmschneider, P. 1970, *A&A*, 4, 144
- . 1974, *Sol. Phys.*, 39, 327
- . 1999, in *Solar and Stellar Activity: Similarities and Differences*, ed. C. Butler & J. Doyle, *Procs. Armagh Workshop (ASP Conf. Series 158)*, 260
- Ulrich, R. K. 1970, *ApJ*, 162, 993
- van Ballegooijen, A. A., Nisenson, P., Noyes, R. W., et al. 1998, *ApJ*, 509, 435
- van der Klis, M. 1989, in *Timing Neutron Stars*, ed. H. Ögelman & E. P. J. van den Heuvel, *NATO ASI C262 (Dordrecht: Kluwer)*, 27
- Vernazza, J. E., Avrett, E. H., & Loeser, R. 1973, *ApJ*, 184, 605
- . 1976, *ApJS*, 30, 1
- . 1981, *ApJS*, 45, 635
- von Uexküll, M. & Kneer, F. 1995, *A&A*, 294, 252
- von Uexküll, M., Kneer, F., Malherbe, J. M., & Mein, P. 1989, *A&A*, 208, 290
- Vorontsov, S. V., Jefferies, S. M., Duval, T. L., J., & Harvey, J. W. 1998, *MNRAS*, 298, 464
- Wang, H., Tang, F., Zirin, H., & Wang, J. 1996, *Sol. Phys.*, 165, 223
- Wang, H. & Zirin, H. 1989, *Sol. Phys.*, 120, 1
- Wang, J., Wang, J., Tang, F., Lee, J. W., & Zirin, H. 1995, *Sol. Phys.*, 160, 277
- Warren, H. P., Mariska, J. T., & Wilhelm, K. 1998, *ApJS*, 119, 105
- Whitaker, W. A. 1963, *ApJ*, 137, 914
- Wikstøl, Ø., Hansteen, V. H., Carlsson, M., & Judge, P. G. 2000, *ApJ*, 531, 1150
- Wilhelm, K., Curdt, W., Marsch, E., et al. 1995, *Sol. Phys.*, 162, 189
- Worden, J., Harvey, J., & Shine, R. 1999, *ApJ*, 523, 450
- Zhang, J., Lin, G., Wang, J., Wang, H., & Zirin, H. 1998, *A&A*, 338, 322
- Zhao, J., Kosovichev, A. G., & Duvall, T. L. 2001, *ApJ*, 557, 384
-



## Dankwoord

Allereerst wil ik de lezer bedanken voor de moeite die hij heeft genomen om toch minstens het dankwoord in mijn proefschrift te lezen. Vervolgens verontschuldigd ik mij onmiddellijk aan iedereen die ik vergeten ben in dit dankwoord op te nemen, want meer mensen dan ik kan herinneren hebben mij bijgestaan bij het maken van dit proefschrift. Ik wil dan ook al mijn familie, vrienden en collega's bedanken voor hun steun.

Enkele personen wil ik toch persoonlijk bedanken. Joke van Dijk, wijlen Aert Schadee voor hun wijsheid en advies. Mandy en Pit voor het met mij uithouden op een kamer en het toch nog gezellig weten te maken. Ed en Sake voor het oplossen van mijn computer problemen. Gé en Marion voor het regelen van al die kleine dingen. And of course much thanks to my co-authors for the fruitful cooperation.

Natuurlijk wil ik Rob Rutten niet uit mijn dankwoord weglaten. Voor het zetten van mijn neus in de goede richting en voor de bereidheid een flinke hoeveelheid "hoe heet het?" gerechtvaardigd commentaar op mijn werk te leveren. Ook Jan Kuijpers wil ik bedanken voor het zijn van mijn promotor en zijn advies in moeilijke tijden.

Voor alle gezelligheid wil ik bedanken: De DOT-spelletjesgroep, de trouwe bezoekers van de A.B.Cie<sup>1</sup> borrels en spelletjesavonden, de B.B.Cie<sup>2</sup>, mijn schermvereniging S.V. Pallós en natuurlijk al mijn vrienden en kennissen met in het bijzonder 'De jongens'.

Mijn ouders wil ik bedanken voor al hun steun en begrip over de jaren. Tevens dank aan mijn twee paranimfen: mijn zus Elize en Jeroen Warnaar.

En natuurlijk wil ik de persoon bedanken die mij heeft bewezen dat dromen toch uitkomen: Jelena. Volim te, bre!

---

<sup>1</sup>Astro Bar Commissie

<sup>2</sup>Bi-wekelijkse Borrel Commissie

---



## Levensloop

Op 29 april 1976 te Dordrecht werd ik geboren. In 1980 verhuisden we naar Numansdorp in de buurt van Rotterdam, alwaar ik naar de basisschool ging tot we aan het eind van het een-na-laatste schooljaar, op 27 mei 1987, verhuisden naar Houten in de buurt van Utrecht. Het laatste jaar van de basisschool heb ik daar afgerond. Vervolgens ben ik in 1988 voor zes jaar naar het Christelijk Gymnasium te Utrecht gegaan tot mijn diploma uitreiking op 17 juni 1994.

Het enige dat voor mij veranderde toen ik Sterrenkunde aan de Universiteit Utrecht ging studeren was eigenlijk mijn fietsroute. Pas later besepte ik de verandering die het studentleven met zich meebracht. In augustus 1995 behaalde ik mijn propaedeuse Natuur- & Sterrenkunde. In 1997 besloot ik dat theoretische sterrenkunde en ik niet bij elkaar pasten en begon ik een observationeel afstudeerproject bij Stichting Ruimte Onderzoek Nederland (SRON). In samenwerking met L. Kuijpers en W. Hermsen schreef ik een scriptie genaamd "COMPTEL detection of pulsed -ray emission from PSR B1509-58 up to at least 10 MeV" waarmee ik op 25 juni 1998 mijn doctoraal sterrenkunde met genoegen behaalde.

Echter zes weken voor mijn afstuderen, met een halfgeschreven scriptie en nog een tentamen te gaan, vroeg Rob Rutten mij of ik zin had mee te gaan naar La Palma om waar te nemen op de Zweedse Zonnetelecoop. Na initieel geprobeerd te hebben iemand anders deze kans te laten "waarnemen", besloot ik zelf te gaan. Hier werd mijn liefde geboren voor observationele zonnephysica en toen Rob mij na een lange wandeling vroeg zijn promovendus aan de Universiteit Utrecht te worden heb ik toegestemd.

Voordat ik besepte dat mijn student-bestaan alweer voorbij was zette Rob mij op het vliegtuig naar San Fransisco om daar het vak en de net gelanceerde Transition Region And Coronal Explorer (TRACE) satelliet te leren van de mensen van Lockheed-Martin die hem bedienen. Het idee was om als de Dutch Open Telescope klaar was deze tegelijk te laten waarnemen met TRACE en aldus de observaties te combineren. Daarom is mijn proefschrift dus voornamelijk gebaseerd op waarnemingen met TRACE. Tijdens mijn promotie ben ik in de Verenigde Staten, Tenerife, Frankrijk, Duitsland, Engeland en Tsjechie soms meerdere keren geweest en heb daar met verschillende mensen samen gewerkt.

Nu zullen we zien wat de toekomst brengt.